THÈSE

présentée pour obtenir le grade de

Docteur en Sciences

Spécialité Physique Théorique

Melting, Surface Relaxation and Thermal Stability of Crystalline Solids

par
Virgile BOCCHETTI

Soutenue le 16 décembre 2013 devant le jury composé de

Prof. BOUKHEDDADEN Kamel	Université Versailles - St Quentin	Examinateur
Prof. DIEP Hung The	Université de Cergy-Pontoise	Directeur
Prof. KAUFMAN Miron	Cleveland State University	Rapporteur
Prof. LEVY Jean-Claude	Université Paris 7 Denis Diderot	Rapporteur
Prof. OUGHADDOU Hamid	Université de Cergy-Pontoise	Examinateur
Prof. PLUMER Martin	Memorial University of Newfoundland	Examinateur

Abstract

In this thesis we study thermal properties and melting behavior of crystals using Monte Carlo simulations. The Monte Carlo method is very difficult to implement for melting investigation, unlike for problems where particles (such as spins) are localized on lattice sites. However, once it is well formulated, it is among the most efficient numerical techniques, to be able to study melting.

We have created a high-performance algorithm shown in chapter 1, based on an optimized Verlet procedure, which allowed us to investigate, with efficiency, thermal properties up to the melting. This optimization was necessary for treating an large number of atoms in very long runs to have good statistics, without prohibitive CPU time. We applied our algorithm to rare-gas crystals using the Lennard-Jones potential with parameters given by Bernardes which are widely used in the literature since 1958. Our results, thanks to their precision, show that we should modify these parameters in order to have a good agreement with experimental data.

In chapter 2, we studied melting of bulk semiconductors and metals by considering the case of Si and Ag. These materials have been chosen for our project in the following chapters as will be seen below. Silicon has a diamond structure, and silver has the FCC lattice structure, both of them have been well experimentally studied with well-known experimental melting temperatures. In spite of this, no good simulations have been done. For Si, one of the major problems is the choice of a potential which stabilizes the diamond structure at finite temperatures. We need a multi-body potential specific for each lattice structure. We have applied our algorithm to these materials using the multi-body Stillinger-Weber and Tersoff potentials for Si and the Gupta and EAM (embedded atom method) potentials for Ag. We obtained results much more precise than in early simulations and in good agreement with experiments.

In chapter 3, we studied the Ag(111) surface trying to elucidate the long-standing controversy whether or not there is the "anomalous" thermal expansion which happens, for certain metals, when the inter-layer distances between the topmost atomic planes changes from a contracted situation to an expansion with respect to the bulk distance. We showed that, depending on the potential, the anomalous crossover exists and the surface melting can occur at a temperature very far below that of the bulk melting. This is the case of EAM potential, but not the Gupta potential where surface melting occurs just below bulk the melting.

In chapter 4, we studied the thermal stability of a stand-alone silicene sheet. Silicene is the Si counterpart of 2D carbon sheet called "graphene". Silicene attracts the attention of many researchers because of its electronic and thermal properties which seem to be comparable to those of graphene,

which is actually one of the most studied materials, due to its unusual properties susceptible for revolutionary device applications. Furthermore, because it is a Si-based material, the compatibility, with the actual Si-based electronic industry, is expected to be better than for graphene. We show that, using the Tersoff potential with two sets of parameters (the original and the modified ones), the silicene 2D honeycomb structure is stable up to high temperatures without buckling. We have tested the Stillinger-Weber potential: it yields a buckled honeycomb sheet at low temperatures but the 2D structure is destroyed in favor of a tri-dimensional structure at the melting. Discussion of this point is given.

A general conclusion with some open perspectives is given at the end.

Résumé

Dans cette thèse nous étudions le comportement thermique de matériaux cristallins, par le biais de la simulation Monte Carlo. Cette technique est très difficile à implémenter pour l'étude de la fusion à cause de la variation du volume du système et des déplacements des atomes hors des noeuds du réseau cristallin. Mais une fois bien mise au point, elle est l'une des plus efficaces pour traiter ce genre de problématique.

Dans le premier chapitre nous présentons notre algorithme conçu en optimisant la procédure de Verlet. Cette optimisation a permis d'étudier le comportement thermique d'un cristal jusqu'à la fusion, avec des simulations très longues pour de meilleures statistiques sans avoir des temps CPU prohibitifs. Nous avons appliqué cet algorithme aux cristaux de gaz rares en utilisant le potentiel de Lennard-Jones (LJ) avec les paramètres calculés par Bernardes en 1958. Ces paramètres ont été largement utilisés dans la littérature depuis. Or nos résultats, grâce à la précision de l'algorithme, montrent que ces paramètres conduisent à une surestimation des températures de fusion de ces cristaux par rapport aux températures de fusion expérimentalement mesurées. Nous avons donc proposé une modification des paramètres qui permet un meilleur accord avec l'expérience.

Dans le chapitre 2, nous avons étudié la fusion des semiconducteurs et des métaux en prenant le cas du silicium de structure diamant et le cas de l'argent de structure cubique à faces centrées. L'objectif de ce chapitre est de comprendre le comportement thermique et la fusion de ces matériaux tridimensionnels avant d'examiner les cas des cristaux bi-dimentionnel et semi-infini dans les chapitres suivants. Ces matériaux dans l'état massif ont été expérimentalement bien étudiés. Malgré ceci, il n'y a pas de résultats théoriques et de simulations avec précision sur le comportement de fusion. L'un des problèmes majeurs dans l'étude de fusion est le choix d'un potentiel qui est capable de reproduire, à basses températures, des structures de réseau autres que le réseau FCC qui est la structure obtenue avec un potentiel isotropique à deux corps tel que le potentiel LJ. Nous avons choisi les potentiels de Stillinger-Weber et de Tersoff pour Si, et les potentiels de Gupta et EAM pour Ag. Les résultats obtenus pour les deux potentiels sont similaires et meilleurs que les résultats publiés dans la littérature. Ils sont en accord avec l'expérience.

Dans le chapitre 3, nous avons traité le cas d'un problème très étudié mais restant controversé: le comportement de la surface (111) d'un cristal d'argent. Expérimentalement, certaines études ont montré que la distance entre la surface et la deuxième couche atomique subit une contraction à basses températu- res. Au fur et à mesure que la temperature augmente, cette distance rattrape celle entre deux couches intérieures et puis la dépasse: ce

résultat est connu sous le nom d'anomalie de dilatation thermique. Nous avons étudié ce problème en prenant deux potentiels multi-corps EAM (embedded atom method) et de Gupta. Les résultats montrent que le potential EAM décrit mieux cette anomalie qui a lieu après la fusion de la surface alors que le potentiel de Gupta ne donne pas la fusion de surface. Par conséquent, l'anomalie de dilatation évoquée n'a pas lieu avec le potentiel de Gupta.

Finalement, dans le chapitre 4 nous avons étudié la stabilité thermique d'une feuille de silicène libre, c'est-à-dire non supportée par un substrat. Ce matériau attire l'attention de nombreux chercheurs du fait de ses propriétés électroniques et thermiques qui semblent comparables à celles du graphène, de même structure en nid d'abeille mais avec des atomes de carbone. C'est l'un des matériaux les plus étudiés actuellement en raison des propriétés remarquables pour des applications. En utilisant le potentiel de Tersoff avec deux jeux de paramètres, nous avons montré que la structure 2D du silicène est stable jusqu'à la fusion qui a lieu à une température élevée, malgré la basse dimension du matériau. Il est à noter que le matériau n'a pas le même comportement selon le jeu de paramètres utilisé. En outre, nous n'avons pas observé le "buckling" avec le potentiel de Tersoff. Le potentiel de Stillinger-Weber donne, en revanche, un buckling mais la structure se déforme vers une structure tri-dimensionnelle à la fusion. Une discussion sur ce point est donnée à la fin du chapitre.

La conclusion générale et les perspectives sont présentées à la fin de ce mémoire.

Acknowledgments

The time of acknowledgments comes and my first ones are destined to my advisor Hung The Diep. Professionally, it was a real pleasure for me to collaborate with him. He knew how to guide my research thanks to his high vision in both scientific and general cultures. Humanly, I could not dream of anyone better to accompany me in this human adventure. I am indebted to him indefinitely.

I thank Professors Miron Kaufman and Jean-Claude Levy who have kindly accepted the hard task to be referees of my thesis. I would also like to thank Professors Kamel Boukheddaden, Hamid Oughaddou and Martin Plumer who have accepted to be members of the jury. It is a honor for me to defend my thesis in front of such a prestigious jury.

I would like to thank the members of the Laboratoire de Physique Théorique et Modélisation for their friendship and for providing me the best conditions to carry out my research. I especially want to thank Sylvie for her kindness and professionalism that has allowed me to concentrate my effort only on scientific matters. I am grateful to my fellow Ph D. students Héloise and Tai for their friendship. I express a special thank to Tai with who I spent the main part of these three years and with who I shared a lot of great moments. I also thank my new colleagues Valentin and Aurélien who have encouraged me during this difficult time of the manuscript preparation.

I also thank Jean-Louis, Philippe and Romane of the university library. Their professionalism and kindness have allowed me to be more efficient in my work.

I finish my non-exhaustive list of thanks by Mr Gennevieve, my physics teacher in high school, who could be the first if I had chosen the chronological order to make this list. I owe a lot to him. He knew how to convey me his passion for physics and more generally for sciences. I also thank my two favorite mathematics teachers Mr Benzekri (high school) and Mr Druet (university). If I am there, it is also thanks to them, their passion and their professionalism.

Remerciements

Je remercie ma femme Mireille pour m'avoir supporté durant ma thèse et pour avoir su me réconforter avec tant de douceur et de gentillesse dans les moments les plus difficiles, et surtout pour ses talents aux fourneaux. C'est dans ses petits plats que j'ai pu trouver l'inspiration. J'éspère qu'elle me supportera encore longtemps. Je remercie mes deux enfants Anton et Terrennce "les chefs" qui me donnent tant de joie et de fierté chaque fois que je rentre à la maison. Ils sont tout pour moi. Je remercie mes parents qui sont à la base de tout pour moi. Ils ont toujours cru en moi et m'ont toujours soutenu dans mes entreprises. Je leur serai éternellement reconnaissant. Avec mon grand père, qui n'est malheureusment plus là mais qui reste toujours dans un coin de ma tête, mes parents m'ont donné le goût de l'effort et du travail bien fait. Je tiens plus particulièrement à remercier mon père qui m'a initié à la physique et aux mathématiques dès mon plus jeune âge sans jamais m'imposer quoi que ce soit. J'éspère que je saurai avoir autant de tact avec mes petits gars. Je n'oublie pas "Læt" et "Gap", ma soeur et mon frère, qui m'ont aidé à me construire sur d'autres aspects que celui de la physique.

Je sais que ma famille est la condition *sine qua non* de ma réussite dans ce travail. Elle m'a donné l'équilibre et la force nécessaires pour pouvoir me dépasser et travailler au rythme de la thèse de doctorat.

Contents

Introduction

Our study is placed in the general framework of condensed matter physics and more precisely in the field of phase transitions.

The thermal behavior of materials is of great importance for several reasons. One of them concerns the functioning of electronic devices. As we know, when the temperature increases, even a simplest device such as a resistance, has a different behavior at high and low temperatures because the electronic transport is modified by the temperature. It is the same for all electrical components such as diodes, self, transistors, etc. Furthermore, with the nanoscale of new 2D materials in the electronic industry, the material is more sensitive to temperature than 3D ones. The change of properties of materials with temperature is also of crucial importance in other domains such as in the nuclear industry.

We focus in this thesis on the melting phenomenon. The understanding of the melting transition is not an easy task and actually we do not have a complete understanding of the phenomenon because melting depends on different mechanisms according to the nature of the interaction between atoms. We have decided to tackle this problem by studying a number of cases using the Monte Carlo technique. This technique is based on statistical physics at equilibrium. Statistical physics is a powerful methodology which allows scientists to study systems containing a large number of particles.

When we deal with a system composed of a tremendous number of particles such as atoms in a crystal (we recall that in 1 cm^3 of a solid crystal there are about 6.02×10^{23} atoms), solving the Schrödinger equation of all interacting particles is simply impossible.

In a system at a fixed temperature (canonical ensemble), the partition function allows us to study almost all physical quantities. This partition function can be obtained by summation over all the microscopic states. In statistical physics, an important idea is the ergodicity principle which is based on the fact that if we average a physical quantity over all the microscopic states at a given time, we will find the same value obtained by an average over all the microscopic configurations that the system takes during a very long

(theoretically infinite) time. This principle allows us to write the average of a quantity X as follows:

$$\langle X \rangle = \sum_{\sigma} X_{\sigma} P_{\sigma} \tag{1}$$

where P_σ is the probability of the microscopic state σ and X_σ the value of X in the microscopic state σ. The probability P_σ is given by :

$$P_{\sigma} = \frac{1}{Z} e^{-\frac{E_{\sigma}}{k_B T}} \tag{2}$$

Z being the partition function which is defined by :

$$Z = \sum_{\sigma} e^{-\frac{E_{\sigma}}{k_B T}} \tag{3}$$

As we said above, the partition function allows us to describe physical properties of the system. For example, the average the energy of the system is given by :

$$\langle E \rangle = -\frac{\partial ln(Z)}{\partial \beta} \tag{4}$$

where $\beta = \frac{1}{k_B T}$.

In simulations, microscopic states are created with some rules during the simulation time as seen below. The Monte Carlo technique is based on the following considerations :

i) The simple sampling method which consist in the generation of several microscopic states in a random manner. Each new microscopic state is chosen independently of the previous one. The average of the observable X being taken over these microscopic states. For a system where N is large, one can understand that all the microscopic states cannot be created. For example a system of N Ising spins has 2^N states, this number is huge even if we take $N = 1000$ very far from real systems. So, even if we were able to find all these microscopic states, it is impossible to make numerically such a huge sum. Hence, some theoretical considerations are needed in order to retain only the most important states without changing physical properties of the system. This is what provided by statistical mechanics in the following importance sampling.

ii) The importance sampling method which is more elaborate than the first one. This sampling uses the generation of most probable states for a given set of parameters such as temperature, volume, number of

particles. These states follow the Boltzmann probability distribution. In this case, each new microscopic state is chosen from the previous one following a Markov chain with a transition probability between these states which respects the equilibrium condition as seen below.

In this thesis we have always used the importance sampling. This procedure, widely used in the field of Monte Carlo simulations, has been proposed by Metropolis et al. in 1953 [1]. The algorithm uses Markov chains as follows.

In a Markov chain, each new state is generated from an existing one with a transition probability $\omega(\sigma \to \sigma^*)$, where σ and σ^* are respectively the actual and new microscopic states. In order to be a Markov chain the following condition has to be verified :

$$\sum_{\sigma^*} \omega(\sigma \to \sigma^*) = 1 \tag{5}$$

We want to generate a Markov chain (i.e. a succession of microscopic states) where each state σ is weighted by the frequency of occurrence of such equivalent states.

At the beginning, we start with a configuration which is generally not at equilibrium. The probability of such state is given by $P_\sigma(t_0)$, where t_0 is the initial time. Thereafter, $P_\sigma(t)$ evolves with time following the evolution equation given by :

$$P_\sigma(t+dt) = P_\sigma(t) + \sum_{\sigma^*} \left[\omega(\sigma^* \to \sigma) P_{\sigma^*}(t) - \omega(\sigma \to \sigma^*) P_\sigma(t)\right] \tag{6}$$

As we can understand, this evolution depends on the number of configurations σ^* which lead to σ, weighted by the transition probability $\omega(\sigma^* \to \sigma)$ and depends also of the number of microscopic states which leave σ, weighted by $\omega(\sigma \to \sigma^*)$.

The needed thermalization time will be achieved when the convergence of the distribution of probabilities P_σ will be done.

When the thermalization is done, the detailed balance is given by :

$$\forall(\sigma, \sigma^*), \quad P_\sigma \omega(\sigma \to \sigma^*) = P_{\sigma^*} \omega(\sigma^* \to \sigma) \tag{7}$$

$$\iff e^{\frac{E_\sigma}{k_B T}} \omega(\sigma \to \sigma^*) = e^{\frac{E_{\sigma^*}}{k_B T}} \omega(\sigma^* \to \sigma) \tag{8}$$

This equation guaranties the system is in equilibrium. Hence we do not have to know the partition function of the system Z, for the choice of the transition probabilities $\omega(\sigma \to \sigma^*)$.

The choice proposed by Metropolis is :

$$\omega\left(\sigma \rightarrow \sigma^{*}\right)=\begin{cases} e^{-\beta\left(E_{\sigma^{*}}-E_{\sigma}\right)} & if \quad E_{\sigma^{*}}>E_{\sigma}, \\ 1 & if \quad E_{\sigma^{*}} \leq E_{\sigma} \end{cases} \tag{9}$$

The Metropolis criterion is then :

- $E_{\sigma^{*}}<E_{\sigma}$, the transition is accepted
- $E_{\sigma^{*}} \geq E_{\sigma}$, the transition is accepted with a probability $\omega_{\sigma \rightarrow \sigma^{*}}$. If not, the system returns to its previous configuration.

In this thesis we have used the NPT set of quantities (N is the number of partivles, P is the pression, T is the temperature) because of the variation of volume with temperature. In this case, the quantity involved in the Metropolis criterion is the free enthalpy given by :

$$W=P\left(V_{\sigma^{*}}-V_{\sigma}\right)+\frac{1}{2}\left(U_{\sigma^{*}}-U_{\sigma}\right)+Nk_{B}T\ln\left(\frac{V_{\sigma}}{V_{\sigma^{*}}}\right) \tag{10}$$

where $V_{\sigma^{*}}$ and V_{σ} are respectively the new and old volumes of the system, $U_{\sigma^{*}}$ and U_{σ} being respectively the new and old energies when changing the microscopic state. Note that the temperature plays a major role in the Metropolis criterion.

The manuscript is organized as follows :

In chapter 1, we review different existing studies on the melting phenomenon. We will see that the melting transition is not well understood in spite of numerous investigations over decades. Indeed, existing theories are not able to give a complete description of the mechanisms underlying this phase transition. This has motivated our work. In the chapter, we build our algorithm and we apply it to the melting of bulk 3D rare-gas crystals. We will give detailed results obtained for Ar, Kr and Xe. In this thesis, we are using a classical approach, hence the case of Ne will not be treated, because of non negligible quantum effects due to its weak mass. The reason for using rare-gas crystals was to calibrate our algorithm with these well studied materials. Indeed, the three rare gas chosen can be easily described by simple potentials such as the Lennard-Jones potential because of the isotropic bonds which govern in these crystals. We find that in order to get a good agreement for the melting temperature, we should modify the parameters of that potential.

In chapter 2, we will apply our algorithm to a semi-conductor material, Silicon. As we will see, all the numerical approaches of the melting transition

of Si diamond structure (which are not so numerous) have failed to obtain the correct melting temperature of this material. Several artificial techniques have been implemented but some of them are questionable (see the voids nucleated method used in Monte Carlo simulation by Agrawal et al.[2]). After the presentation of the two potentials used for modeling Si diamond structure, namely the Stillinger-Weber and Tersoff potentials, and of ours results, we will propose a modification of some parameters of the Stillinger-Weber potential in order to obtain the melting temperature in agreement with experimental measurements. Such an approach has been used by Agrawal et al. for the Tersoff potential. We will present also this modification. Another material has also been studied with our algorithm: the bulk face-centered cubic lattice of Silver atoms. As we will see, using the two currently popular potentials for simulations of metals, the melting temperature obtained with our algorithm is in good agreement with experiments. This material was used next to study the behavior of the (111) surface of a silver sample.

In chapter 3, we will study the thermal behavior of the Ag(111) surface which is, as we will see, well investigated in the literature. Indeed, surface behaviors of crystals have already been studied a long time ago (1969) [3]. It is well known that surfaces of metals (almost all metals) have contraction of the inter-layer distances of the first topmost layers. The case of the Ag(111) surface is one of the most studied surfaces both experimentally and theoretically. An anomalous lattice relaxation of the topmost inter-layer distances, namely a crossover between contraction and expansion with increasing temperature, is suspected for this surface. As we will see, this anomalous behavior is still a subject of controversy. Note that, probably due to difficulties of implementation, the Monte Carlo method has never been used to study this behavior before. Hence, our study is the first Monte Carlo contribution to this problem. Our main results are reported in [4]. The study of the (111) surface of silver is also due to the fact that it will be used as a substrate to study physical properties of silicene which is a 2D honeycomb lattice of Si atoms.

In chapter 4 we will introduce this promising material which is probably the most serious concurrent of the graphene which has an analogous structure: a 2D honeycomb lattice of C atoms. Indeed, experimentally, the most favorable surface for the growth of silicene is the (111) surface of Ag. That is why a thorough understanding of this surface was needed. We will describe the thermal behavior of a free-standing silicene sheet even if experimentally such a configuration has never been obtained so far. The reasons why we study such a configuration are numerous. Firstly we can mention that the study of such a stand-alone material is needed in the case where the interaction from the substrate is negligible. Furthermore, experimentally it is possible to grow a free sheet of graphene so we expect that it will be done

for silicene in the near future. Secondly, theoretical studies of free-standing silicene, based on density-functional theory (DFT) calculations have already been done and prove the stability of this hypothetical situation. Thirdly, this is probably the best approach to the problem: we begin to study the system in the simplest situation and we will introduce afterwards interactions with the substrate in order to better describe the actual experimental configuration. Interactions with the substrate have been studied but will not be presented in this thesis because the results are too preliminary. Calculations are in progress. One of the main difficulties is to choose an appropriate potential to describe the silicene-substrate interaction.

The last chapter is devoted to a general conclusion of the present thesis.

Chapter 1

Melting of Bulk Rare-Gas Crystals

1.1 Introduction

Melting of crystals has always been a fascinating subject for more than a century since the discovery of the empirical Lindemann's criterion [5]. The Lindemann's criterion says that if the average of vibration amplitude u, namely $\sqrt{\langle u^2 \rangle}$, exceeds a certain value, usually 10% of the distance between nearest-neighbors, then the melting occurs. Times and over again, many authors have tried to find out microscopic precursor mechanisms that lead a crystal to melt. Until 30 years ago, one of the favorite pictures of melting is the softening of a phonon mode due to thermal fluctuations. The atoms no longer have restoring forces which keep them staying close to their equilibrium positions: they move around freely and the system goes to a liquid state. The soft-mode picture has encountered some scepticism because in real crystals as well as in simulations one observes that well below the melting temperature (T_m), many defects, dislocations, interstitial atoms, *etc* are excited. Therefore, it is hard to believe that the system stays in a periodic structure with propagating phonon modes up to T_m . Evidence of defects is found in many works [6, 7, 8, 9]. Another question that is unsolved in a clear manner is the form of the potential that binds the atoms together in a given lattice structure. From a microscopic point of view, the potential should come mainly from the symmetry of atomic orbitals. But ab-initio calculations are still far away from being able to use realistic potentials [10]. Empirical potentials have been used instead to study melting. One can mention the popular 6-12 power Lennard-Jones (LJ) potential [11, 12], various similar power potentials, the many-body Gupta's potential [13], the Stillinger-Weber (SW)

potential [14], the Tersoff potential [15, 16] and the Embedded Atom Model potential (EAM) [17]. Two-body potentials such as the LJ one crystallize atoms in the FCC at low temperatures and nothing else; this comes from the fact that LJ potential is isotropic so the atoms are crystallized in the most dense isotropic structure, namely the FCC lattice. In order to stabilize other structures, several phenomenological potentials have been introduced, often without a microscopic justification. For example, the SW potential or the Tersoff potential stabilize the diamond structure at low temperatures. These potentials have been used with success to calculate properties of Si clusters [18] and amorphous Si crystals [19].

In this chapter, we use the LJ potential to study the melting of rare-gas crystals which have the FCC lattice structure at low temperatures. In the case of rare gas, it is amazing that such a simple question was not studied with precision so far in spite of an abundance of experimental data on Ar, Xe, Ne and Kr. Most of the melting studies concerning rare gas were done in particular cases: small clusters [19], adlayers on a substrate, etc. The main reason to avoid to study the bulk melting may be due to some technical difficulties such as periodic boundary conditions, volume expansion with temperature, etc. Previous Monte Carlo (MC) studies of bulk melting have been carried out with LJ potential but emphasis was put on the melting mechanism rather than on the precise melting temperature in real materials [7, 8].

The purpose of this chapter is therefore to test whether or not the experimental T_m can be reproduced by MC simulation using the values of the parameters given in literature for all the materials tested here. For example in rare gases, they are deduced in the gaseous state long time ago [20]. We will show here that by appropriate choices of technical procedures, we are able to obtain melting temperature for various rare gas *directly* from our simulations, unlike previous methods [21, 22, 23, 24] which have had recourse to various means and some thermodynamic functions to deduce it. We find in this work the melting temperatures for several rare gases are higher than experimental values. A revision of the values of LJ parameters widely used in the literature for more than 50 years should be made in order to better describe the solid state of the rare gas. Note that in a recent work [23], a hypothetical thermodynamic integration path is used to find the relative free energies of the solid and liquid phases, for various system sizes, at constant cutoff radius, in an attempt to explain the overestimate of the melting temperature with the LJ potential. However, due to various approximations, several results were not physically clear, in particular why the melting temperature oscillates with increasing cutoff distance.

In the case of Silicon, it is more difficult to have a good agreement with

experiments as we will see in the next chapter. Indeed, unlike the LJ potential, SW and Tersoff potentials, are more difficult to modify because of the huge number of parameters and because they contain a many-body contribution. This is even more true for the Tersoff potential, where the many-body part is not so transparent. In the case of the SW potential, the many-body part concerns only the lattice-geometrical part, so modifications are easier. For Silver, as we will see in the next chapter, the melting temperature simulated with our algorithm is in good agreement with experiments, with the two potentials used.

The organization of the present chapter is as follows: In Sec. 1.2 we present an overview of different principal theories and numerical works dealing with melting of materials since 1891, in Sec.1.3 we show details of our algorithm and finally in Sec.1.4, we present our results obtained for rare-gas crystals.

1.2 Melting transition: historic developments

Lindemann's criterion

Sutherland was one of the pioneer scientists who considered atoms as hard spheres vibrating around their equilibrium position [25]. He was the first to propose that the melting transition occurs when the atomic distance between particles reaches a certain value with respect to the atomic diameter. This model leads the calculation to an important consequence: all elements have almost the same ratio of vibration amplitude to the atomic spacing. Nineteen years later and following Sutherland's idea, Lindemann [5] shows that when the temperature reaches the melting point, the displacements of crystal atoms are so large that some collisions between neighboring atoms occur. The instability created by these collisions could be responsible for the melting transition. In 1956, Gilvarry [26] has proposed the formulation of the Lindemann's criterion which says that the melting occurs when the square root of the mean-square amplitude of thermal vibrations of atoms reaches around 10% of the nearest-neighbor distance. This criterion was often used and tested. This was the case in 1982 when Cho [27] found that the Lindemann parameter (the critical ratio of vibration amplitude over the nearest-neighbor distance) depends on the structure of the lattice. For bulk centered cubic (BCC) or face centred cubic (FCC) or also hexagonal compact (HCP) the Lindemann parameter is different. Even if the Lindemann's criterion is still widely used, it's a one-phase theory and this model does not explain the mechanisms responsible for the melting transition.

Born's criterion

When the temperature rises, the inter-atomic distance increases. This phenomenon implies a decrease of the restoring force and then, the shear modulus decreases. Sutherland has studied the dependence of the shear modulus with temperature for metals. In his work [25], he proposed an empirical law with the following expression :

$$G = G_0 \left(1 - \frac{T}{T_0})\right)^2 \tag{1.1}$$

where G is the shear modulus. As we can see with this model, the shear modulus fall to zero when $T = T_0$. For Sutherland, the melting point could be the temperature at which the rigidity falls to zero. In 1938, Brillouin [28] pointed out a difference between macroscopic rigidity and the microscopic one. Indeed, he has observed that the macroscopic rigidity of a solid falls to zero at the melting temperature while the microscopic one has a non zero value. By the consideration of the anisotropy of crystalline phases, he emphasized that the different rigidity coefficients would not become zero at the same temperature. He proposed that melting occurs when one of the rigidity coefficients falls to zero.

In 1939, Born [29] proposed his criterion for the melting of crystal which suggests that melting occurs when one the shear modulus becomes zero. The main problem of this theory is that the liquid phase is not described. The first-order behavior of the melting transition is then not treated. Indeed, the main characteristic of a first order transition is the heterogeneity of the system during the transition. During the transition, some parts of the system are in the liquid state while other parts are in the solid state.

Role of the defects as melting mechanism

The importance of the role of defects in the melting mechanism was understood by Gorecki [30]. He studied the role of vacancies in melting transition of metals. For him, there is a correlation between the bonding energy of metal and the vacancy formation energy. One of his major results concerns the value of 0.37% which is the equilibrium vacancy contraction at the onset of melting for many metals in different lattice configurations. Using this model, the volume change on melting can be explained by the fact that the volume increases because of the formation of vacancies at the melting temperature. Also the electric resistivity can be interpreted by vacancies formation. Indeed, when vacancies are created, electrons have more difficulties to go through the material. The latent heat can also be interpreted in terms of

the energy associated with the formation of vacancies in metals. This theory is also well supported by one experiment. Indeed, the gamma irradiation which creates vacancies allows experimentalists to lower the melting point proportionally to the irradiation.

In the same period (1979), Nelson and Halperin studied the melting transition in 2D systems. They show that the melting is due to defects [6]. It is the same phenomenon which occurs with the XY 2D model where we have a Kosterlitz-Thouless transition.

In 2001, a Monte Carlo study of the role of defects in the 3D melting transition was carried out by Gómez, Dobry and Diep [7], using the LJ potential. They show that defects which occur in the solid phase are responsible for the melting. They monitored the number of defects by integrating the radial distribution function (RDF) between two neighboring minimum. They found that, although the sample temperature is below the melting point, a lot of defects are created (around 26% of the total number of sites). This result is in contrast with the scenario of the phonon soft-mode responsible for the elasticity instability at the melting point, as we have seen above with the hypothesis of a defect-free crystal structure. They have also evaluated the percentage of defects just above the melting point and found a value of 80%.

Using RDF for the defects (Fig. 1.1) and histograms (Fig. 1.2), they have also studied their structure. More precisely, they have found that the defects

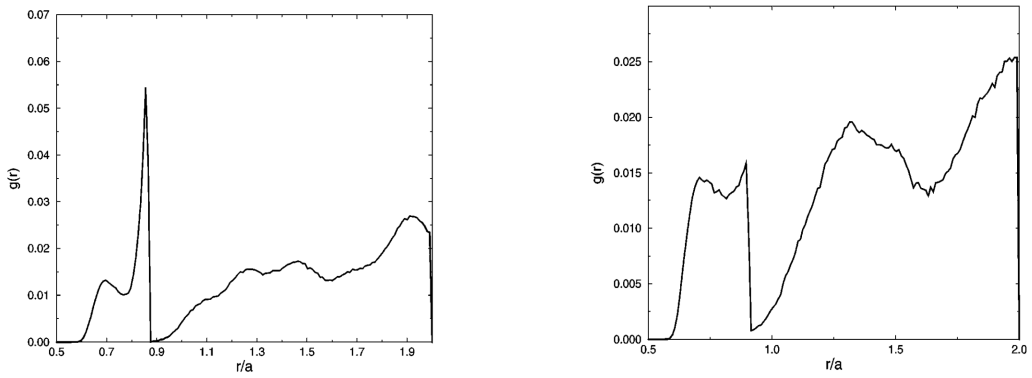

Figure 1.1: Radial distribution function between defects of coordination 13 just below the melting point (0.76 in reduced unit) (taken from Ref. [7]).

form clusters and that they are linked over large distances near the transition. Indeed, we can see in the histograms that the probability to observe clusters of large sizes increases with the temperature (Fig. 1.2). The appearance of the third and the fourth peaks at temperatures near the melting transition is in supports of the idea that the clusters are not isolated but linked. The

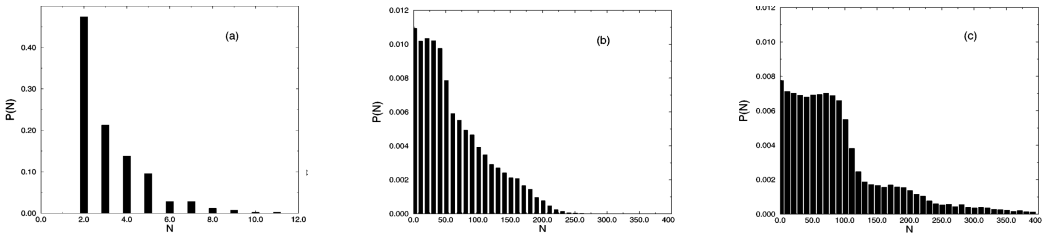

Figure 1.2: Histogram of the number of defects in a cluster.Left : $T = 0.3$, center: $T = 0.58$ and right: ($T = 0.725$ (taken from Ref. [7]).

authors used the expression "strings of defects" which summarizes very well the results obtained.

In an other work [8] (the first one where strings of thermally excited defects are seen), it is shown that the strings of defects are dislocation lines like it was suggested in [31, 32]. Their computations are consistent with the melting theory based on the saturation of the crystal by dislocation loops of all sizes including open lines crossing the system.

Extrapolation using the results from clusters

More recently in 2008, Pahl et al. have numerically extrapolated the melting temperature of bulk Ar starting from clusters [33, 34]. Using complete Mackay icosahedra which are more stable configurations for cluster containing less than 1000 atoms they studied cluster of size 13, 55, 147, 309, 561 and 923. These "magic numbers" are given by the following formula :

$$N = 1 + 2\sum_{k=1}^{n}\left(5k^2 + 1\right) \tag{1.2}$$

They found a linear behavior of the melting temperature with the increasing of the cluster sizes, provided that the number of atoms in the cluster be greater than about 100. When we deal with clusters of a few hundreds (around 923 atoms at maximum), it is obvious that surface effects cannot be neglected. Indeed, the ratio between surface and volume is again in favor of surface effects domination over volume effects. As we can see in Ref. [34] (Fig. 8), the behavior of the melting temperature with clusters of less than 100 atoms is different from the behavior of clusters of more than 100 atoms. With clusters of 100 to 923 atoms the behavior is linear while this is not the case before 100 atoms. Although 923 particles is a quite good number of atoms, it is not clear that after that limit the surface effect on the melting temperature follows this linear behavior. The fact that the melting

temperature can be extrapolated from clusters with increasing sizes is then questionable. Indeed, there is a huge difference between a cluster of 923 particles and a macroscopic sample of materials. We are not sure that such a linear behavior will continue until the macroscopic level will be reached. Noya and Doye [35] have questioned this convergence by monitoring the heat capacity curves for different sizes of clusters. Indeed, a premelting phenomena remains for clusters with sizes greater than 309 atoms. Furthermore, Pahl et al. [33, 34] have also compared their clusters results with their bulk calculations using periodic boundary conditions for system sizes less than 256 particles. Unfortunately, as we will see below, we find a threshold of 500 atoms for the saturation of the melting temperature with periodic boundary conditions. To finish, they also used the minimum image convention like us, but for all the sizes tested, they never used the same cutoff for the potential so it is difficult to analyze their results.

1.3 Our algorithm

1.3.1 Motivation

As we have seen in the previous section, a lot of artificial tricks or hypothesis are used to modeling the melting of a material. The major motivation of our work was to built an algorithm which minimizes the use of these artificial manipulations. For example, we don't want to introduce artificial voids into the system as it as been done in several works with the two widely used techniques for modeling the melting transition: molecular dynamic simulations (MD) and MC simulations. In order to fulfill our objectives, we have used MC simulations. Indeed, unlike in MD simulations, the MC method allows the system to have defects created by the huge quantity of random numbers used (several tens of millions of MC steps in this work). Indeed, sometimes, a non-favorable configuration can be accepted thanks to the Metropolis criterion. That's why fluctuations can be seen in all the quantities monitored. The introduction of defects (artificially) is a widely used practice with MD simulations (see Refs. [36, 37, 38]). This procedure is essential in this technique because the atoms follow the Newton laws of motion so that defects cannot be naturally created. In Ref. [2], Agrawal et al. have artificially introduced voids in a silicon bulk crystal in order to reduce the melting temperature that they find well above the experimental one. With MC techniques, it is not necessary to apply this method. We think that superheating due to the difficulty to break the crystalline order cannot happen with MC simulations because the method is based on statistical averages in the phase space with-

out following vibration modes and because the tremendous number of Monte Carlo steps used in this work. The phase space is then well explored. That's why, without a free surface in our sample, starting from a perfect crystal, we can have the formation of defects with increasing temperature during the simulation, a thing which is not possible with the MD technique.

1.3.2 The algorithm

The modeling of the melting transition is difficult for several reasons. One of these reasons is the off-lattice behavior. Another one is that we have to perform our computations in the NPT ensemble, in order to take into account the volume variation with temperature, and the volume fluctuations with time. This second characteristic is difficult to take into account when we use the periodic boundary conditions (PBC).

In this subsection, we will describe precisely how we have done to take into account these behaviors.

Firstly, a diagram of the algorithm can be found in Fig. 1.3.

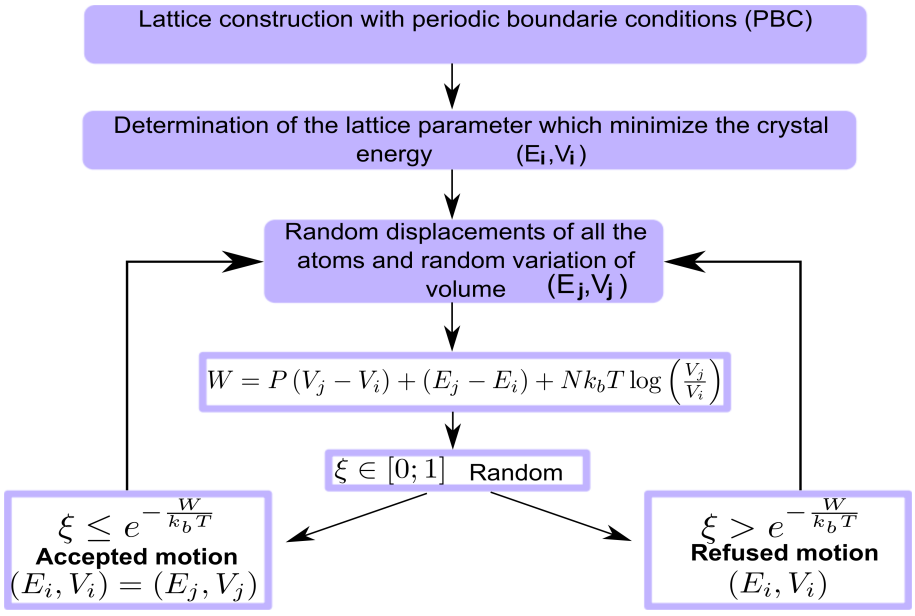

Figure 1.3: Diagram of the algorithm.

For all simulations, we have to consider a finite size system with PBC, because of the finite available memory in the computer. Of course, different sizes of system can be tested but always limited by the memory. The

simulation box corresponding to the system is a cubic box[1] (for a cubic system) which contains all the system atoms. Example of simulation boxes are represented in Fig. 1.4

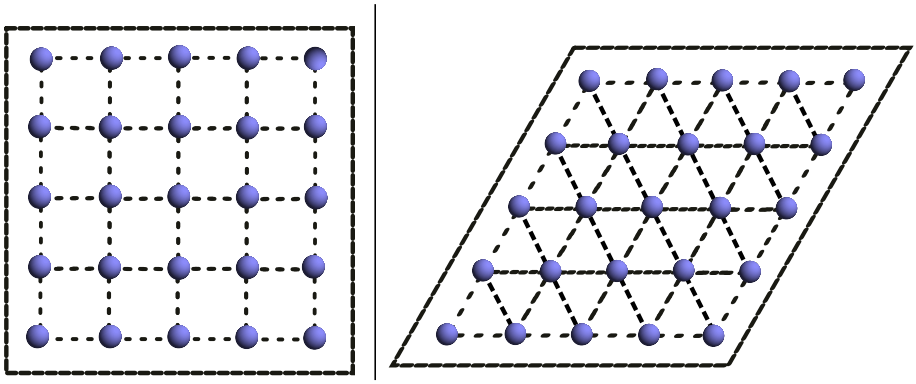

Figure 1.4: Simulation boxes for 2D-square lattice and for 2D-triangular lattice

The off-lattice behavior of the atoms can be described as follows: when the crystal melts, all the atoms can go everywhere, in the simulation box. In this case, the crystalline structure is completely broken. Why is this a difficulty for the algorithm ? For each atom, when the algorithm is running, we have to compute different quantities which depend on the neighborhood of the considered atom. When the atoms are fixed each to a node of the lattice or when the atoms can move but near its node, the list of the neighbors is always the same. This list is known as the Verlet list [39, 40]. The knowledge of the list of neighbors allows the algorithm to be faster. If we don't use tricks to accelerate the algorithm, we have to compute $\frac{1}{2}N(N-1)$ terms with most of them turning out to be zero. With his early version, the computing time was cut by a factor of 10. We have used a modified version rather than the original one. In this former version, for a particle, the algorithm builds a table containing all the particles within a distance r_n from that particle. In this algorithm, the list is updated every $n-1$ Monte Carlo Step (MCS). No error was made as long as r_n is sufficiently larger than the potential cutoff r_c. The number of MCS n can be determined by considering the worst case for the displacements, namely when a particle moves in the same direction and with the same maximum magnitude while the others go in the opposite direction with the same maximum magnitude. The problem of this version is that the number of MCS n, does not depend on the temperature. As we

[1]Depending on the crystal considered, the box can be of different shape like parallelepipedic

can easily understand, this number of MCS must be different at low T when the atoms are almost fixed on the nodes of the lattice, and at high T when the crystal is melted. As we can see, this former version was not the optimal one.

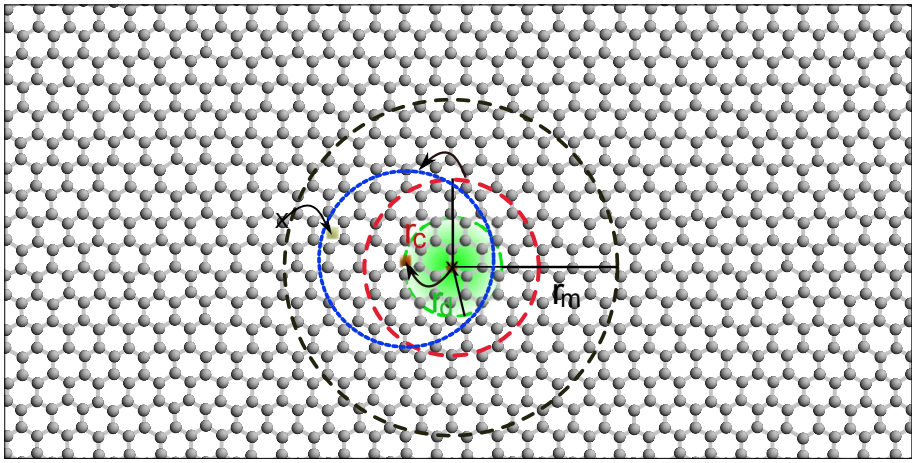

Figure 1.5: Illustration of the worst case considered for the determination of the radius r_d within the neighbors list can be conserved without update. The green sphere is the area where the atom can move without changing it neighbors list. The red circle is the potential cutoff sphere and the black one is the neighbors sphere. The blue sphere represents the displacement of the red one when the atom undergoing the MCS has accomplished its displacement.

We have modified the previous algorithm in order to take into account the dependence of n on temperature. The new algorithm is able to determine itself the number of MCS to do before the update of the list of neighbors.

For the convenience of the reader, we denote S_n the sphere containing the neighbors and S_c the potential cutoff sphere.

The algorithm is as follows: for each atom (at the beginning of the program) the list of neighbors is built and the atom's nearest node of the lattice is saved. For each MCS we compute the distance between the new position of the atom and its node. When this distance is greater than the value r_d , the old position is replaced by the new one and it becomes the new 'node'. The list of neighbors is then updated. With this procedure, the temperature is taken into account automatically. As we can easily understand, the value of r_d is of great importance. Indeed, if this radius is too small, the list of neighbors is too often updated and then we do not earn any CPU time. Conversely, if r_d is too great, the list of neighbors can be wrong. These two

last points are illustrated in Fig. 1.5, in the simplified case of a 2D lattice. We have made our choice by considering the worst case: at each MCS the considered atom goes straightly in the same direction; This direction is chosen as follows: the nearest atom outside S_n is the closer of all this outside atoms. In the worst case, this outside atom goes in the direction of the atom undergoing the MCS. As $r_c < r_n$, when the outside atom comes in the neighbors list, we do not have to update the neighbors list immediately. When the atom under consideration moves, S_c moves with it and the previously outside atom then interacts. It happens when the two considered atoms have moved one half of the difference $r_n - r_c$. In our simulation we have chosen to take $r_d = 0.2\,(r_n - r_c)$ to have a sufficient safety margin. We can mention that this factor 0.2 can be modified until 0.5. Our decision to take 0.2 is arbitrary but allows us to have reasonnable CPU time for the considered systems in this study.

Of course, as we can imagine, when the temperature is greater than the melting temperature, the list is more often updated than at low temperature where the list is almost never updated. That is why, for high temperatures we need more CPU time than at low temperatures to achieve the same number of MCS.

Another important case is the treatment of the atoms on the edge of the simulation box. Let us discuss these further. When one atom is on the edge of the simulation box, a little displacement can put the atom out of the box. In this case, the PBC are applied and we reput the atom on the other side of the box. The PBC is only a manner to simulate an infinite crystal. The PBC can be seen as instantaneous copies of the system (26 copies in 3D, 8 copies in 2D and 2 copies in 1D). An instantaneous snapshot of a system with its PBC is shown in Fig. 1.6.

When the considered atoms leave the box in one direction, one of its 26 copies on the opposite direction comes into the system. The new atom of the system is then the copy of the previous atom. This new atom has a list of neighbors which does not change while the distance between it and its attached node is less than r_d. That is why these atoms have a different treatment than the core's atoms.

The last trick that we have used is that we have saved the 26 copies of each atom. An atom with its 26 copies are moved in a parallel manner. With this procedure, we do not have to make copies of the system at each MCS. Furthermore, for each copies of one atom, the list of neighbors is built hence, when the periodic boundray conditions are applied and when an atom of the system go out of the simulation cell, the list of neighbors of this last one is replaced by the list of neighbors of the corresponding copy of the atom. This procedure allows us to save CPU time.

This optimization allowed us to simulate systems with 4000 particles for about 20 million MCS during 4 weeks in the cluster of computers of the University of Cergy-Pontoise. For each temperature, a simulation was run in an independent node of the cluster. In its original version, Verlet algorithm was at least 10 times faster than the algorithm without any optimization. In our case, the speed of the algorithm is much greater than the Verlet speed. Without this optimization, the CPU time needed was discouraging.

When we use the PBC we have to avoid having a copy of the considered atom in its list of neighbors. This can create some artificial correlations. To avoid this well-known phenomenon in simulations, we are in the minimum image convention: all the dimensions of the simulation box are chosen at least twice the potential cutoff.

Now let us discuss about the volume variations in the NPT statistical configuration. When the temperature is increased, the system tends to dilate. This implies an increase of the volume of the simulation box. How can we associate this behavior with the previous considerations namely the node distances and the PBC ? The solution that we have taken is to use the reduced coordinates. We can describe the mechanism as follows: the positions of the system atoms are saved in reduced coordinates with the dilatation coefficient. In this set of coordinates, the volume of the simulation box does not change. When we compute distances between atoms, we multiply the reduce distance by the dilatation coefficient to get the real one and then we can compute the energy or RDF.

The volume fluctuates during the simulation time at each temperature. We took into account the real volume when we calculated the necessary quantities.

1.4 Application to rare-gas crystals[2]

1.4.1 Interaction potential

The Lennard-Jones potential is an empirical potential which is well suited for noble gas atom interactions. Rare-gas atoms, in their crystalline state, are slightly modified relative to the atomic stable configuration they have in the gaseous state. This little deformation can be described by the van der Waals interaction. This interaction is attractive and responsible for the cohesion of the crystal of these rare-gas materials. The interaction is usually modeled by the power 6 of the inverse of the interatomic distance. The power 6 can be justified by the fact that the van der Waals interaction is dipolar. Indeed,

[2]Published work, see Ref. [41]

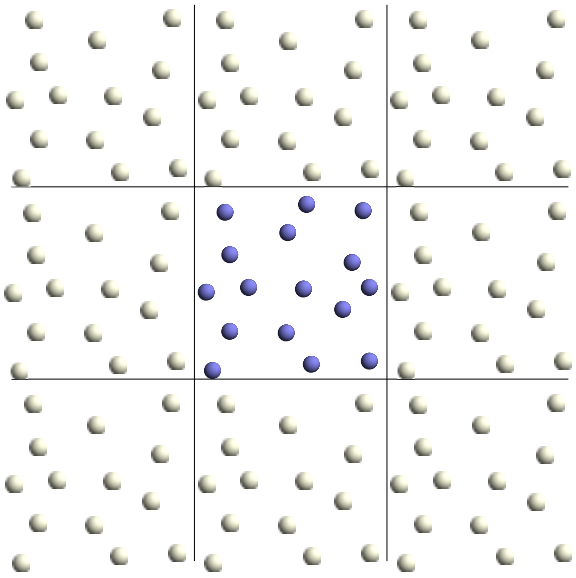

Figure 1.6: 2D periodic boundary conditions of a system (blue atoms). In 2D, an atom has 8 copies of itself. The lines indicate the simulation box.

we consider two atoms (1 and 2) separating by a distance r. Let $\overrightarrow{p_1}$ be the dipolar moment of the atom 1, the dipolar moment of the second atom induced by the atom 1 is proportional to $\frac{p_1}{r^3}$ ($p_2 \simeq \frac{\alpha p_1}{r^3}$). Furthermore, two atoms with a dipolar moment have an interaction energy proportional to the product of the moment, divided by the power 3 of the interatomic distance: $\frac{p_2 p_1}{r^3} \simeq \frac{p_1^2}{r^6}$. That is why we consider the power 6 of the interaction distance.

In order to avoid the collapse of the crystal into a single point, and to be in agreement with the Pauli exclusion principle, a repulsive part is also taken into account. This interaction is mathematically described by the power 12 of the inverse of the interatomic distance.

The repulsive part of the potential is greater than the attractive part at small distances, and inversely at long distances. After this analysis, the potential has the following expression:

$$V(r) = 4\epsilon \left[\left(\frac{\sigma}{r}\right)^{12} - \left(\frac{\sigma}{r}\right)^{6} \right] \tag{1.3}$$

where ϵ and σ are adjustable parameters which depend of the material. The values of these parameters used for noble gas [20] (Ne, Ar, Kr and Xe) are reported in Tab.1.1. The representative curve of the potential is plotted in Fig. 1.7.

If we write the expression of the distances between atoms compared to

Table 1.1: Lennard-Jones parameters (from [20]).

Element	ϵ (eV)	σ(Å)	T_m (K)
Ne	0.00312075487	2.74	24
Ar	0.01042332126	3.40	84
Kr	0.01404339691	3.65	117
Xe	0.01997283116	3.98	161

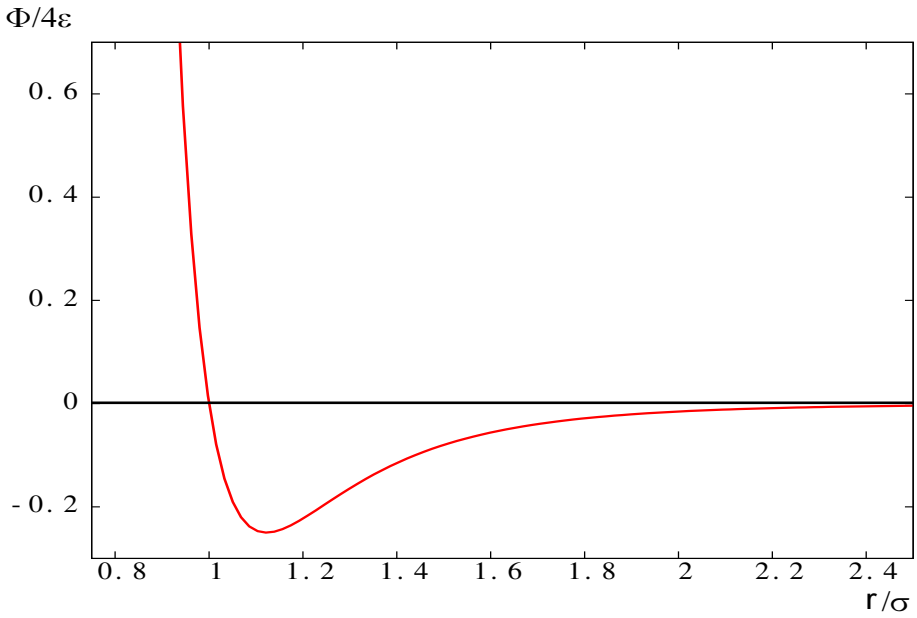

Figure 1.7: Curve of the Lennard-Jones potential.

the nearest neighbor (NN) distance taken as unit length we obtain :

$$U = \frac{1}{2}\sum_{\overrightarrow{r}} V\left(\overrightarrow{r}\right) = 2\epsilon\left[A_{12}\left(\frac{\sigma}{r}\right)^{12} - A_6\left(\frac{\sigma}{r}\right)^{6}\right] \tag{1.4}$$

where

$$A_n = \sum_{\overrightarrow{r}\neq 0} \frac{1}{\alpha\left(\overrightarrow{r}\right)^n} \tag{1.5}$$

with α being the multiple of the nearest neighbor distance corresponding to $\overrightarrow{r}$.

The lattice constants A_n depend on the lattice structure. In the case of rare gas, the lattice is FCC, we have $A_{12} = 12.13$ and $A_6 = 14.45$ [42].

These two last quantities are useful to find the equilibrium nearest-neighbor distance satisfying: $\frac{\partial U}{\partial r} = 0$. Starting from Eq.1.4, we have:

$$\begin{aligned} \frac{\partial U}{\partial r} &= 2\epsilon \left[6A_6\sigma^6 \frac{1}{r^7} - 12A_{12}\sigma^{12}\frac{1}{r^{13}} \right] \\ \frac{\partial U}{\partial r} &= 0 \\ \iff \quad 6A_6\sigma^6\frac{1}{r^7} &= 12A_{12}\sigma^{12}\frac{1}{r^{13}} \\ \implies \quad r_0^{th} &= \left(\frac{2A_{12}}{A_6}\right)^{\frac{1}{6}}\sigma \end{aligned} \tag{1.6}$$

where r_0^{th} is the first nearest-neighbor distance minimizing the crystal energy.

Now, if we put the result given in Eq. 1.6 into the Eq. 1.4, we can obtain the equilibrium cohesive energy of noble solids :

$$U_0 = -\frac{\epsilon A_6^2}{2A_{12}} = -8.6\epsilon \tag{1.7}$$

In Tab. 1.2, we can see the agreement between theoretical and experimental values (Data coming from [43, 44, 45]). The greater the atomic weight is, the better the results are. This phenomenon is a consequence of the fact that the zero-point energy has been neglected. Here we consider the atoms in a classical point of view, and then, at zero temperature, we supposed that all the atoms are perfectly localized with zero kinetic energy [46]. As we know[3], the zero-temperature kinetic energy is proportional to $\frac{\hbar^2}{M(\Delta_x)^2}$, where M is the weight of the element. The more M is important, the smaller is this kinetic energy.

[3] using the uncertainty principle of Heisenberg

Table 1.2: Nearest-neighbor distance and equilibrium cohesive energy at atmospheric pressure for noble solids.

	Ne	Ar	Kr	Xe
$r_0^{Exp.}\left(\mathring{A}\right)$	3.13	3.75	3.99	4.33
$r_0^{Th.} = 1.09\sigma$	2.99	3.71	3.98	4.34
% of error	$\simeq 4.47$	$\simeq 1.06$	$\simeq 0.25$	$\simeq 0.23$
$U_0^{Exp.}(eV.atom^{-1})$	-0.02	-0.08	-0.11	-0.17
$U_0^{Th.} = -8.6\sigma$	-0.027	-0.089	-0.120	-0.172
% of error	$\simeq 35$	$\simeq 11.25$	$\simeq 9.09$	$\simeq 1.17$

Using the lattice parameters A_6 and A_{12} we can also compute the bulk modulus :

$$\begin{aligned} B &= -V\left(\frac{\partial P}{\partial V}\right)_T \Longleftrightarrow B = \\ v\frac{\partial}{\partial v}\left(\frac{\partial u}{\partial v}\right) \Longleftrightarrow B &= 2\epsilon\left[\frac{1}{\sigma^2}\frac{A_6^{\frac{7}{3}}}{A_1 2^{\frac{4}{3}}}\right] \end{aligned} \tag{1.8}$$

In this subsection we will show our MC results for Ar, Kr and Xe. We did not perform simulations on Ne because of its quantum effects, namely the zero-point energy due to its weak atomic mass. Indeed, as previously noted, we used a classical approach. In this approximation, every atom can be precisely localized. As we know, this is not correct because of the Heisenberg uncertainty principle which implies that the kinetic energy at 0 K is proportional to $\frac{\hbar^2}{M(\Delta x)}$. Here, we consider that the cohesive energy of our crystal is only a potential energy, that is why we do not consider the case of Ne. We can see in Tab. 1.2 the percentage of error for the NN distance and the cohesive energy. The materials are ordered with increasing atomic mass.

In a more quantitative way, we can use the de Boer parameter which is defined as follows: $\Lambda = \frac{h}{\sigma\sqrt{M\epsilon}}$. In Tab. 1.3, we give the values of this parameter for several rare gas (Ref. [46]).

Table 1.3: de Boer parameter Λ for rare gas.

^{4}He	Ne	Ar	Kr	Xe
2.6	0.59	0.19	0.10	0.064

Λ^2 roughly represents the ratio between the kinetic energy and the potential energy. It allows us to measure the importance of the quantum effects.

In the following we show first the results obtained for the Ar crystal, using the Bernardes parameters. These will put in light the necessity to modify the original parameters. Next, we will show the new results obtained with the modified parameters.

1.4.2 Monte Carlo results using the Bernardes parameters

Let us show first the results for Ar obtained by using the values listed in Table 1.1. We will discuss next the modification necessary for obtaining the results in agreement with experiment. In order to take a correct average of physical quantities, we record spontaneous values of all physical quantities during each MC run. We have to go to several million of MC steps before observing statistical equilibrium. We show an example of the energy per atom E versus MC time in Fig. 1.8 for $N = 256$ atoms at two temperatures $T = 92$ K and 94 K. At $T = 92$ K, the system is still in the solid phase. Its energy is stabilized after about one million MC steps per atom. However, at $T = 94$ K, the system melts after three millions of MC steps per atom: E is stabilized in the liquid phase only after such a long MC time. It is very important to emphasize that the convergence time to equilibrium depends on various MC parameters such as value of displacement magnitude r, volume variation δ etc. So, nothing can replace an observation of the time-dependence of physical parameters during the simulation, although this consumes a huge computer memory.

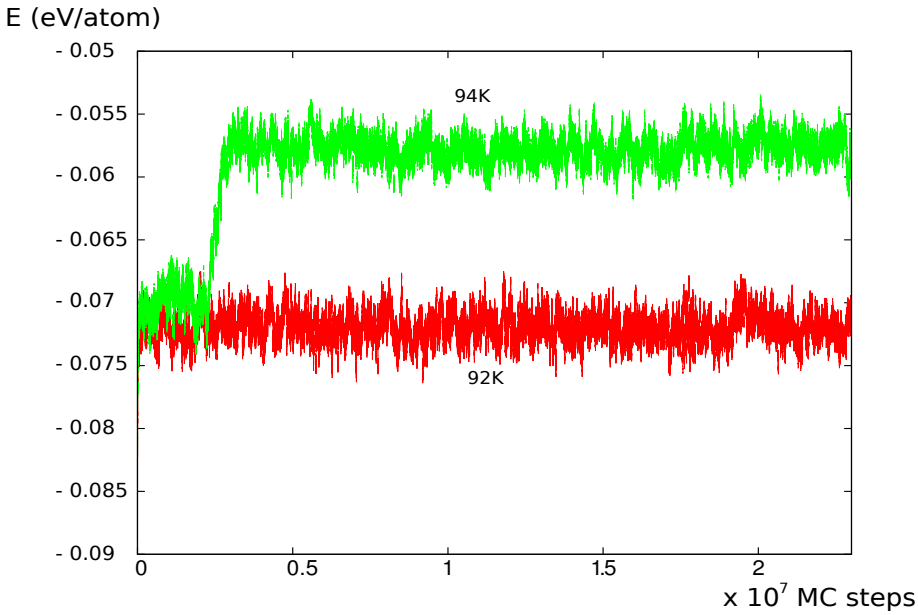

Figure 1.8: Energy per atom versus MC time for two temperatures: above (94K) and below (92K) the melting temperature.

We show in Fig. 1.10 the energy per atom E versus T in the case of Ar with $N = 256$ atoms, using the parameters given in Table 1.1.

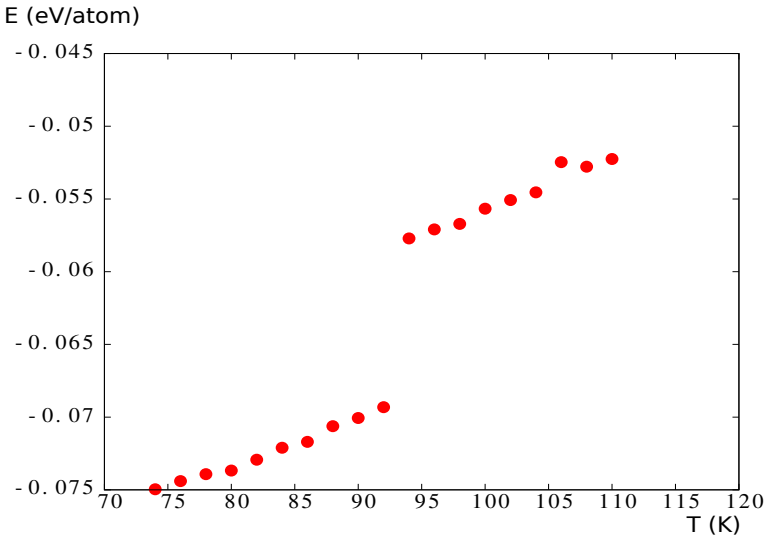

Figure 1.9: Energy per atom E versus temperature T with Bernardes parameters. $T_m \simeq 93K$. Argon crystal, N = 256 atoms. Run of 50 million of MC steps / atom

We observe here that the melting occurs at $T_m = 93K$ with a large latent heat. This value of T_m is rather far from the experimental data given in Table 1.1. We return to this point later.

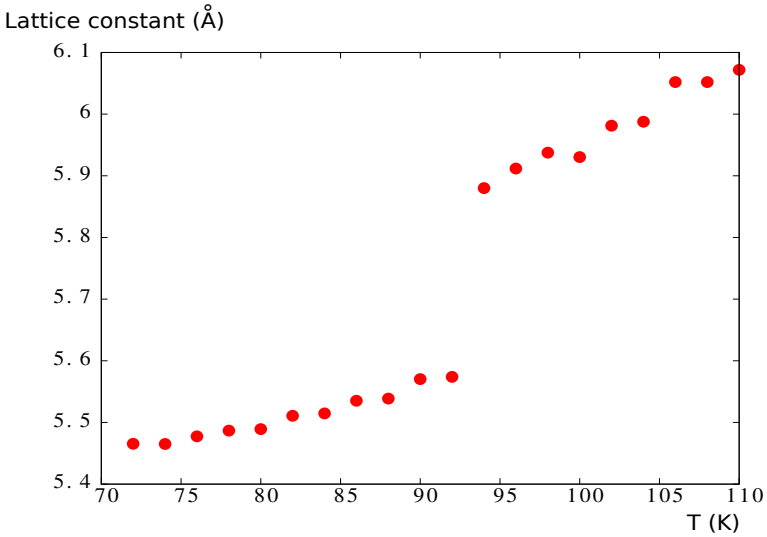

Figure 1.10: Evolution of the lattice constant against temperature T with Bernardes parameters $T_m \simeq 93K$. Argon crystal, N = 256 atoms. Run of 50 million of MC steps / atom

We also display in Fig. 1.10 the lattice constant versus T showing a jump at 93 K.

We show now the snapshots of the system for different temperatures in Fig. 1.11 below and above the melting. As seen, the system just starts to be spatially disordered at 92 K, and is well in the disordered phase (liquid) at 100 K.

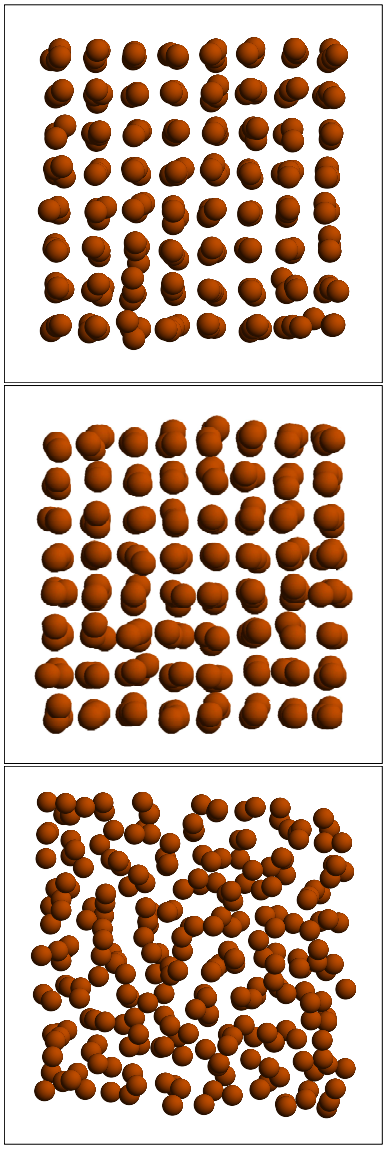

Figure 1.11: Instantaneous pictures of the supercell of Ar for different temperatures, respectively, from up to down: 75K (far below T_m), 92K (close to T_m), and 100K (above T_m). N = 256 atoms. After 35 million of MC steps.

The radial distribution function for Ar is shown in Fig. 1.12 at several temperatures.

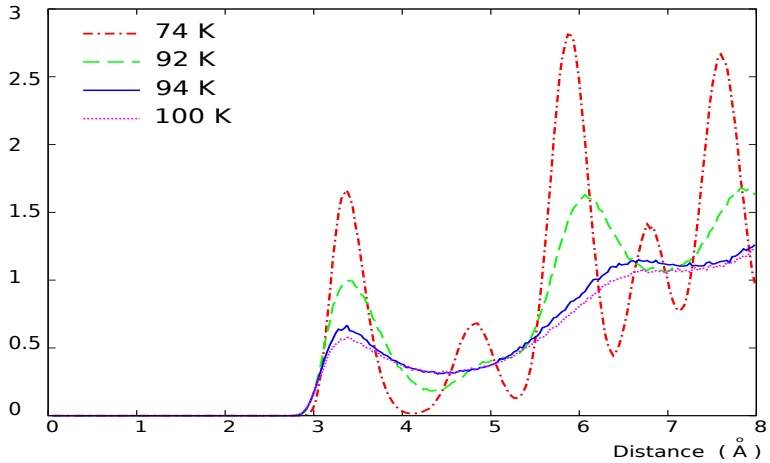

Figure 1.12: Radial distribution of Ar for different temperatures: below melting T=74K (dashed red) and T=92K (dashed green), above melting T=94K (solid blue) and T=100K (solid magenta), N=256 atoms. Run of 50 million of MC steps / atom

One sees clearly the peaks at first, second, and third neighbor distances for $T < T_m$ indicating the crystalline phase, while there is no such clear distinction for $T > T_m$ where a liquid phase sets in. Let us discuss now the difference between our value of T_m $(N = 256) = 93$ K with the experimental value T_m (exp)=84K. Clearly, the parameters given in Table 1.1 which have been deduced with experimental data for gaseous Ar do not well describe the melting of solid Ar. Note however that the above value of T_m is for N = 256 atoms. We consider larger samples below to see the variation of T_m. In order to modify correctly the LJ parameters while respecting the known properties of Ar, we use the listed values of LJ parameters to estimate the size effect, namely to find the value of T_m $(N = \infty)$ for an infinite crystal. Once this task is done, then we look for the parameters (ϵ , σ) which give correctly the experimental T_m(exp). The effect of the cutoff distance will be examined in the following section.

Size effect and effect of the cutoff distance

The size effect is an important fact when we work with numerical simulations because of the finite size of the simulation cell. In second-order phase transitions, finite-size scaling laws allow us to calculate the critical exponents by varying the system size [47, 48, 49, 50]. The correlation length is infinite at

the critical point in the thermodynamic limit. However, in first-order transitions in infinite systems, the correlation length is finite at the transition pointT_c , the two phases coexist [51, 52, 53, 54, 55] and the energy is discontinuous. In simulations at finite sizes, if physical quantities such as T_c, the maximum of the specific heat C_v and the susceptibility, etc., depend on L_d (system volume) then the transition is of first order [51, 52, 53, 54, 55]. For very weak first-order transition, only with extremely large sample sizes together with a high-performance technique such as the Wang-Landau flat histogram technique that we could see evidence of first-order transition (see, for example, Ref. [56]). In this work, we did not perform these types of finite-size analysis. We just considered a few system sizes to see the variation of T_m : T_m is increased but saturated at 102 K for sizes larger than 500 atoms as shown in Fig. 1.13. The same kind of behavior can be observed with Kr and Xe in Fig. 1.15. Indeed, the size of 5 lattice constants is the minimal one to avoid artificial size effects which degrades the quality of results. After 5 lattice constants for the length of the supercell, the melting temperature T_m is not modified for Ar, Kr and Xe.

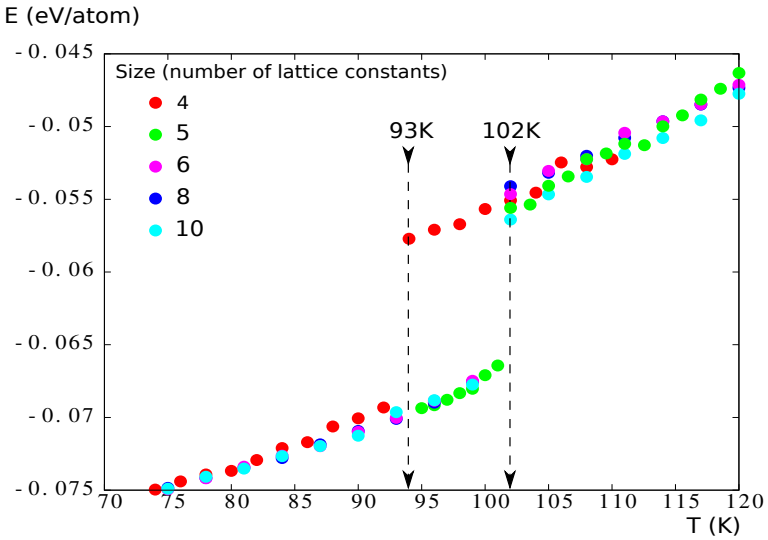

Figure 1.13: Energy per atom versus T with various system sizes from $N =$ 256 (4 FCC lattice cells) to $N = 4000$ (10 FCC lattice cells). The arrows indicate T_m for the smallest and largest sizes.

Now, we examine the effect of the cutoff distance r_c. For large r_c, the contributions of far neighbors are small. From a certain value of r_c, T_m does not significantly vary with all the considered materials. This is due to the fast decaying term $\frac{1}{r^6}$ of the LJ potential. As observed in Fig. 1.14, T_m is

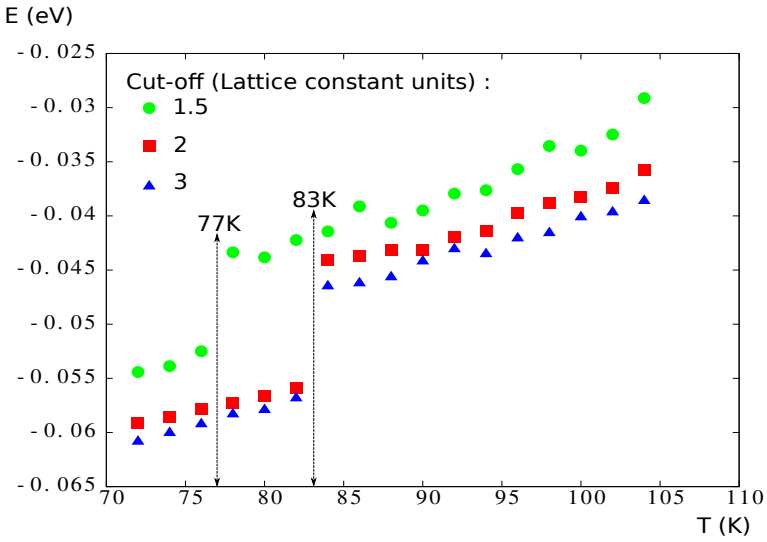

Figure 1.14: Energy per atom versus T with various values of r_c for Ar crystal with $N = 500$. The left arrow indicates T_m for $r_c = 1.5l$ and the right arrow indicates T_m for $r_c = 2l \simeq 10.6\mathring{A}$ and $3l \simeq 15.9\mathring{A}$. Note that l is the FCC lattice constant which is equal to $r_0\sqrt{2}$ where $r_0 = 3.75\mathring{A}$ is the NN distance.

saturated for $r_c \geq 2$ for all the three materials tested, *i.e.*, $r_c \geq 10.6\mathring{A}$ in the case of Ar. Beyond this value, the contributions in energy of the others atoms become so small that even if we use larger size of system it still suffices to warrant the main conclusion, namely that the original LJ parameters yield incorrect melting temperature which is about 20% higher than the experimental one, i.e., much greater than the errors induced by finite-size or cut-off effects shown in Figs. 1.13 and 1.14 where finite-size and cutoff effects are indeed negligible on the scale of interest. The disagreement comes from the fact that the values of the Bernardes parameters were calculated with a low-density gas using the second virial coefficient [57]. These parameters are therefore questionable as we can see in Refs. [58, 59, 60]. The values of the nearest-neighbor distance, the cohesive energy calculated using the Bernardes parameters taken from these papers are listed in Table 1.2. We can see the differences between experimental values and theoretical ones for all cases Ne, Ar, Kr, and Xe.

The Bernardes parameters also yield a high melting temperature found in our simulations with respect to the experimental one. At this stage, it is interesting to note that MD simulation of melting of a perfect crystal with periodic boundary conditions produce superheating, namely a state in which the system stays in the "unstable" crystalline state in a small temperature

region above the melting temperature due to the lack of defects (surface or dislocations) to trigger the melting [2].

There is an empirical rule which states that the melting temperature of a crystal without any surface and any defects, is 20% [2] higher than the true thermodynamic melting temperature T_m. However in MC simulations, defects and dislocations are naturally created in the crystal by means of random numbers used in every MC step for atom displacements. Thus, the superheating should not exist. Agrawal et al. have shown in Ref. [2] that for Ar, with MC simulation, T_m is about 15% higher than the experimental value. With our results for Ar, we find an increase of about 20%. For Kr, we find an increase of 13% for N = 256 atoms after 23×10^6 MC steps per atom. This increase is more important if we consider larger sizes as seen in the case of Ar. As said, the high values of T_m in MC simulations are not due to the superheating as in MD simulations. Rather, we believe that these high values are due to the inaccuracy of the listed Bernardes parameters. In the following section, the modification of the Bernardes parameters is shown.

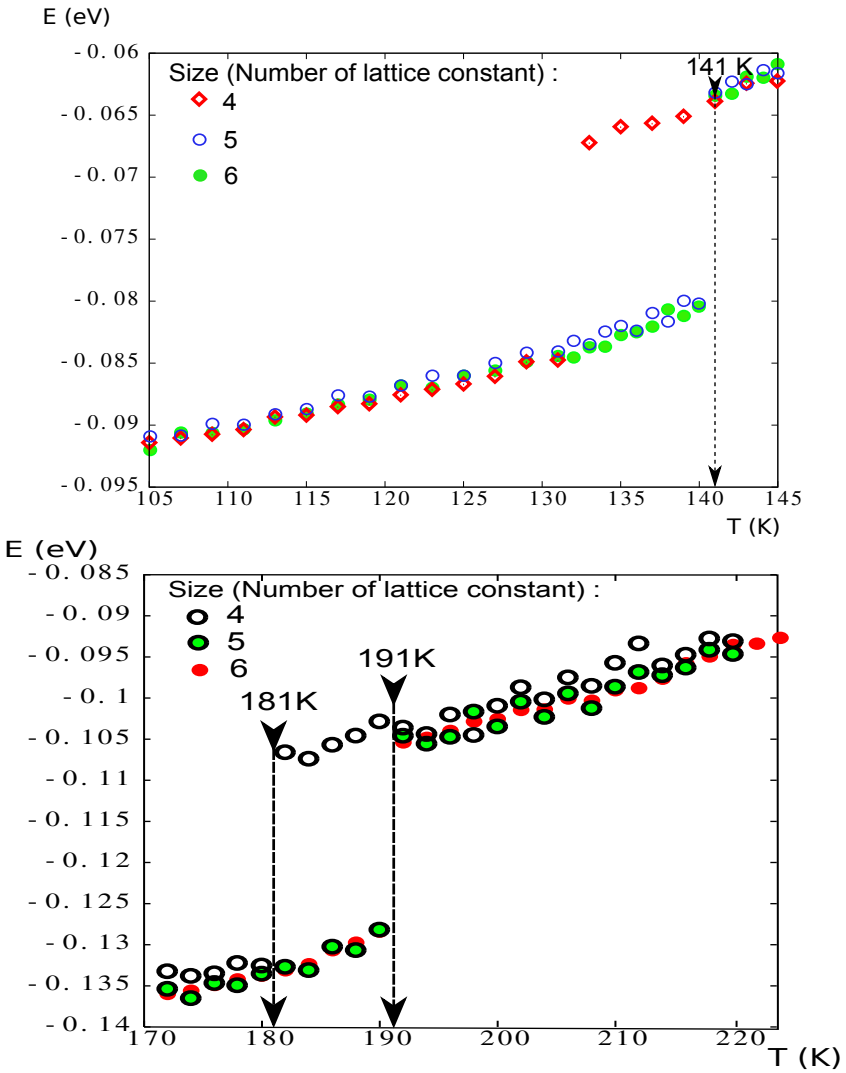

Figure 1.15: Top : Energy per Kr atom versus T with various system sizes from $N = 256$ (4 FCC lattice cells) to $N = 864$ (6 FCC lattice cells). The arrows indicates T_m for largest size. Bottom : Energy per Xe atom versus T with various system sizes from $N = 256$ (4 FCC lattice cells) to $N = 864$ (6 FCC lattice cells). The arrows indicate T_m for smallest and largest size.

1.4.3 Modification of the LJ Bernardes parameters

In order to reduce the simulated T_m value, we propose to modify the value of ϵ, the prefactor of the LJ potential, and the coefficient σ. We have done simulations with different pairs of (ϵ, σ) for Ar, Kr and Xe. The values of these parameters were computed with two constraints: the ground state energy and nearest neighbor distance should be respected. It turned out that T_m depends essentially on ϵ for the three materials. There is however an optimal value of σ which corresponds to the experimental nearest-neighbor distance (cf. Table 1.2).

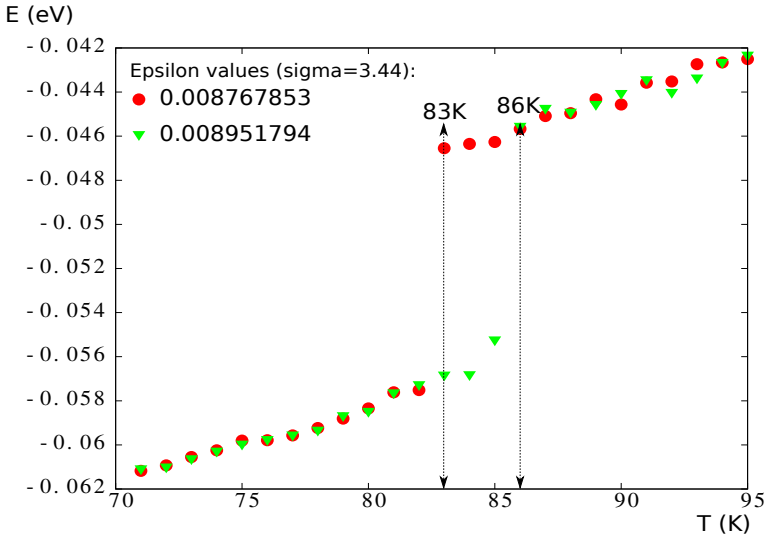

Figure 1.16: Energy per atom versus T for two selected values of ϵ, with $\sigma = 3.44\mathring{A}$, for an Ar crystal with $N = 500$. The arrows indicate T_m for the two indicated values of ϵ.

Table 1.4: Modified (ϵ, σ) for noble solids.

	Ar	Kr	Xe
$\epsilon^{Old}(eV.atom^{-1})$	0.01042332126	0.01404339691	0.01997283116
ϵ^{New}	0.008767853	0.01197446324	0.01718091625
%	$\simeq -15.88$	$\simeq -14.73$	$\simeq 13.97$
$\sigma^{Old}\left(\mathring{A}\right)$	3.40	3.65	3.98
$\sigma^{New} = -8.6\sigma$	3.44	3.66	3.97

We show in Fig. 1.16 the curves obtained for Ar with two selected values of $\epsilon = 0.008767853$ and 0.008951794 which give, respectively, $T_m = 83$ K and

86 K. These values of T_m are in agreement with the experimental value 84 K within statistical errors. Note that the modified ϵ is about 15% smaller than the original Bernardes value $\epsilon = 0.01042332126$ in the case of Ar. In Table 1.4, we have reported all the computed values of (ϵ, σ) for the three considered materials.

1.5 Conclusion

In this chapter, we have studied the melting transition by Monte Carlo simulations. We have described an algorithm which we use to study with efficiency phase transitions in the case of bulk 3D materials. We have applied our algorithm to rare-gas crystals (Ar, Kr and Xe) and obtained directly from our simulations physical quantities such as internal energy, lattice constant and radial-distribution function as functions of temperature. We have shown that melting occurs with a large latent heat and a jump in the lattice constant. Effects of system size and cutoff distance have been investigated.

For rare-gas crystals, in order to make a correction to the over-estimation of the melting temperature given by the LJ-Bernardes set of parameters, we have proposed a new parametrization of LJ potential, for Ar, Kr and Xe. This new parametrization is obtained by fitting the cohesive energy, the lattice constant and the melting temperature. We recall that this is not a surprise because the Bernardes-LJ parameters already yield theoretical NN distance, cohesive energy, and bulk modulus different from corresponding experimental ones (see Table 1.2). Our results for those rare gas are in good agreement with experiments.

In the following chapter, we will study, using our algorithm presented in this chapter, the Si bulk diamond structure and the Ag face-centered cubic lattice. We focus our attention in these two materials because they are used to study the surface effects and the 2D silicene crystal in the remaining chapters of this thesis.

Chapter 2

Bulk Silicon and Silver Crystals

Silicon and Silver are two materials which are commonly used in electronics industry. A deep understanding of the thermal behavior of these is then of great interest. Silicon crystalize in a diamond structure, while Silver crystalize in an face-centred-cubic lattice. In order to modelling such behaviors we have to consider two differents kind of potentials. The potentials used in this work regarding Silicon, are able to modelling the tetrahedral geometry of a diamond structure by the mean of two different approaches (geometrical and physical). For Silver, the two potentials used are able to modelling the FCC structure. Further details are given in the following.

2.1 Silicon

Silicon is the most used material in the electronics industry, and there have been many investigations of this material spanning several decades. Despite this fact, it is difficult to find in the literature results on the melting of Silicon perfect 3D infinite crystal. One of the difficulties encountered when working with Silicon is how to stabilize the diamond structure because it is not the most dense: the tetrahedral environment of a silicon atom results from energy considerations only if there is an anisotropy in the potential. That is why classical pair-potentials like Lennard-Jones potential, which are isotropic, do not work because they are potentials which depend only on the distance between two atoms. In such potentials, when the temperature increases, the system crystallizes in the FCC structure which is energetically most favorable because of the high packing fraction of this phase.

There are several potentials able to describe silicon phases. Balamane et al. [61] have done a comparative study of six many-body empirical potentials which are: the Pearson-Takai-Halicioglu-Tiller potential (PTHT), the

Biswas-Hamann potential (BH), the Stillinger-Weber potential (SW), the Dodson (DOD), the Tersoff-2 [62] and the Tersoff-3 [63] (resp. T2 and T3) where 2 and 3 denote two distinct sets of parameters for the same potential function. Inspired by their analysis and in order to compare our results with the existing ones, we have studied silicon with SW and Tersoff potentials. We have reported in Fig. 2.1 the comparison of the two-body potential functions for the potentials treated in [61].

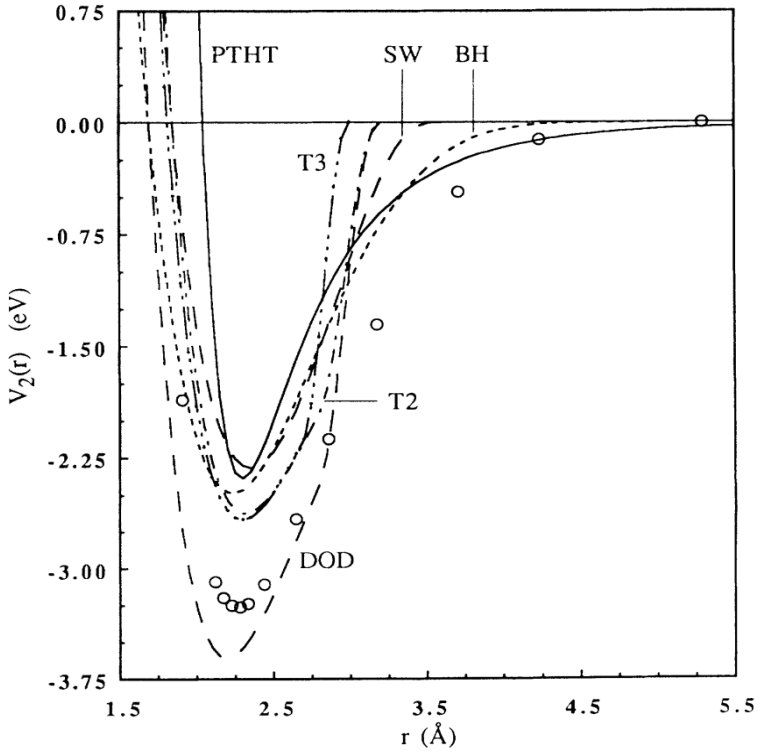

Figure 2.1: Comparison of the two-body potential functions for silicon. The open circles correspond to *ab initio* calculation (taken from Ref. [61]).

As we can see in Fig. 2.1, the two-body terms of SW, T2, T3 have almost the same behavior. The PTHT and the BH are more like LJ potential with a slow convergence toward zero energy. DOD differs from SW, T2 and T3 by the depth of the well of energy. The global behavior of these potentials is almost the same. The slope of the large-distance part of these curves ($\geq 2.5\mathring{A}$) is greater in the case of SW, T2 and T3 potentials than that in the other cases. This could explain why the melting temperature obtained with these three potentials is rather high.

Fig. 2.2 shows the three-body part of all these potentials. These curves are obtained by deforming an equilateral triangle with initial bond lengths

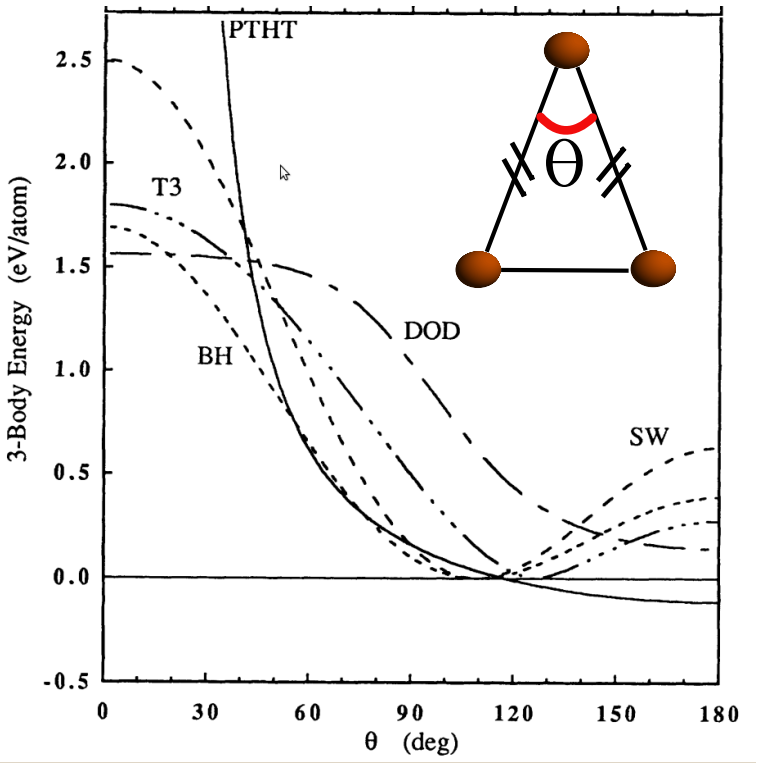

Figure 2.2:
Three-body energy versus angle of silicon atoms forming isosceles triangle (taken from Ref. [61]).

being the equilibrium distance given by the two-body term and computing the new configurational energy. For the SW we can see the minimum of energy for $\theta \simeq 109°$, the tetrahedral angle in the diamond structure. For the T3, as we can see the angle does not have this value. For the T3, it is the competition between the two-body and the three-body part which gives the lower energy for the diamond structure.

The PTHT is the sum of a two- and three-body terms. This potential uses the LJ potential for the two-body term and the Axilrod-Teller potential for the three-body term. The use of this last one has no theoretical justification to describe bonding in covalent material [64], that is why we have decided to not use PTHT.

We did not use the BH and DOD potentials because they have not been tested, so it was difficult for us to compare our results with results in the literature.

There is also the Keating potential [65] which is suitable for phonon description but which is not accurate when the distortion of the lattice becomes

large. Thus, this potential cannot be used in our simulations where the temperature will be increased until the liquid phase.

The Tersoff potential used in this work is denoted by Tersoff-4 (T4) (see Ref. [16]) which is the same as T3 but which is also able to take into account multi-component systems (C-Si and Ge-Si systems with a good accuracy for modeling SiC defects) by adding one more parameter: χ. The T3 is the T4 when $\chi = 1$.

2.1.1 Stillinger-Weber potential

In 1985, Stillinger and Weber [66] have succeeded in the creation of a temperature- and density-independent potential which is able to describe some properties of silicon. It was not so obvious that such a potential-energy-function is valid because of the presence of conduction electrons.

In order to construct their potential, they started from the most general form of a potential-energy function ϕ describing the interaction between N identical atoms. This function contains a sum of different parts which are : the single-atom part, the two-body part, the three-body part, ...

They decided to use only the two- and the three-body parts because of the strong directional bond which exists in silicon-diamond structure.

$$V = \epsilon A \left[\sum_{i,j} v_{ij}^{(2)}\left(r_{ij}\right) + \frac{\lambda}{A} \sum_{i,j,k} v_{jik}^{(3)}\left(r_{ij}, r_{ik}\right) \right] \tag{2.1}$$

with

$$v_{ij}^{(2)}\left(r_{ij}\right) = \left[B\left(\frac{r_{ij}}{\sigma}\right)^{-p} - 1 \right] \times exp\left(\frac{1}{\frac{r_{ij}}{\sigma} - a}\right) \times \Theta\left(a - \frac{r_{ij}}{\sigma}\right) \tag{2.2}$$

and

$$v_{jik}^{(3)}\left(r_{ij}\right) = exp\left[\frac{\gamma}{a - \frac{r_{ij}}{\sigma}} + \frac{\gamma}{a - \frac{r_{ik}}{\sigma}}\right] \times \left(cos\theta_{jik} + \frac{1}{3}\right)^2 \times \Theta\left(a - \frac{r_{ij}}{\sigma}\right) \times \Theta\left(a - \frac{r_{ik}}{\sigma}\right) \tag{2.3}$$

where $v_{ij}^{(2)}$ is the 2-body part and $v_{jik}^{(3)}$ the 3-body one. As the cosine of the tetrahedral angle in the diamond structure is equal to $-\frac{1}{3}$ (see Fig. 2.3), when each silicon atom is on a site of the perfect diamond structure, the

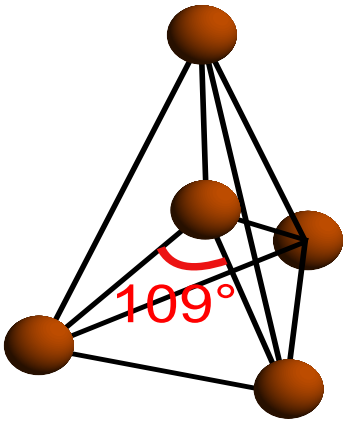

Figure 2.3: Tetrahedral configuration of the atoms in the diamond structure. The value of the angle is around 109°, the cosine is equal to $-\frac{1}{3}$.

three-body part is equal to zero (see Fig. 2.4). If we analyze more in detail this last term we can understand that it is a purely geometrical term.

The parameters for the SW potential are given in table 2.1.

Table 2.1: Stillinger-Weber parameters for silicon Ref. [66]

Parameter	Value
ϵ (eV)	2.16826
A	7.049556277
B	0.6022245584
σ(Å)	2.0951
p	4
a	1.80
λ	21.0
γ	1.20

In order to check if this potential is suitable for our algorithm, we have plotted the energy from the two-body part against the nearest-neighbor distance and the three-body part against the silicon-silicon angle in Fig. 2.4. As we can see, when the angle of the three-body term is equal to about 109°, the energy of this term is equal to zero. When the configuration is deformed, the energy given by the three-body increases (whatever the deformation is, *i. e.* with smaller or greater angle). When the angle becomes greater than 180°, the energy decreases until the angle reaches the value of around 251°, which is equal to 360°-109° [the symmetrical configuration of the first one (109°)].

As we can see, the configurational energy is lower for the nearest-neighbor (NN) distance $r_0 \simeq 2.35\mathring{A}$. This distance coincides with the NN distance in a diamond structure with a lattice parameter of $5.43\mathring{A}$ ($\frac{\sqrt{3}}{4} \times 5.43 \simeq 2.35\mathring{A}$), namely silicon.

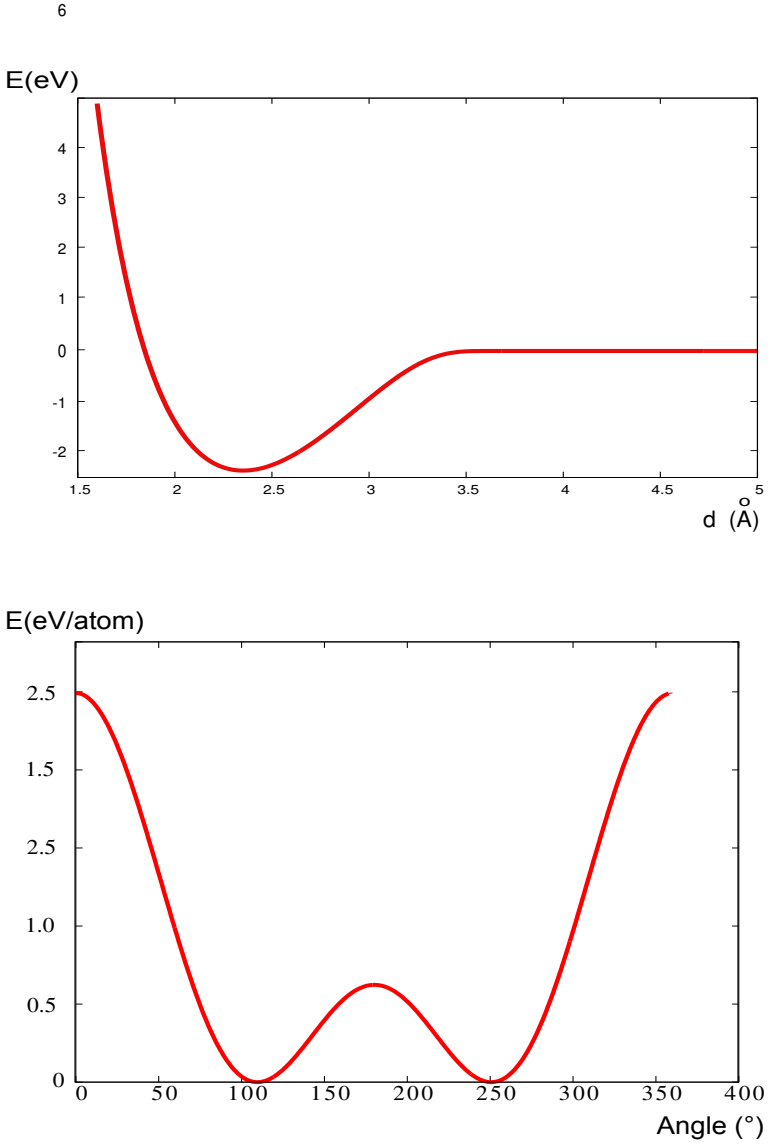

Figure 2.4: Top: two-body part of the Stillinger-Weber potential; Bottom: three-body part.

As we can see in Fig. 2.5, the configuration with the lower lattice energy is the diamond one. Hence, when we will start our MC simulation, the diamond structure will not be easily broken, as will be the case using a classical pair

potential like the LJ one. Energetically, as the diamond structure has the lowest energy, the structure is stable. Indeed, if we begin a Monte Carlo simulation without a configuration in the lowest energy state, the configuration cannot be stabilized. The system will become quickly disordered.

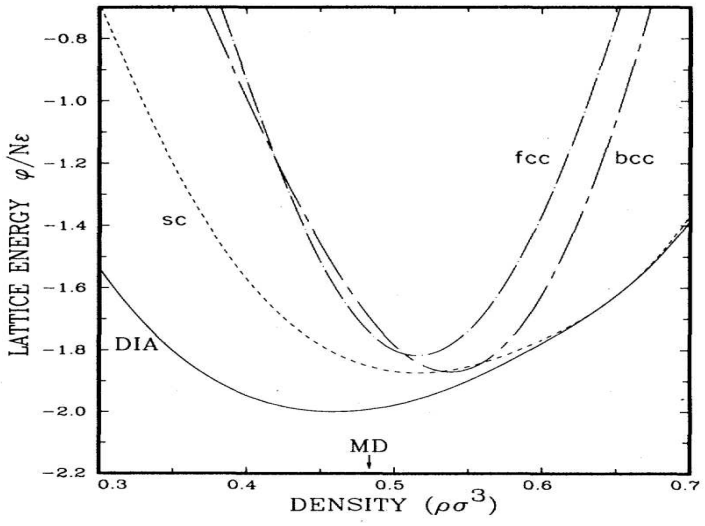

Figure 2.5: Energy (in reduced unit) curve for different structures of lattice (FCC, SC, BCC and diamond), using the SW potential for silicon (taken from Ref. [66]).

Stephenson et al. [67] have proposed a modification of the SW potential in order to better describe the Si(111)-(7x7) surface of silicon. Indeed, the SW potential has been used with the (001)-(1x1), (001)-(2x1) and (111) surfaces with a good accuracy but it fails when Stephenson et al. tried to use it for adatoms on the Si(111)-(7x7) surface. As we will see when we try to describe surface atoms of silicon, there are some difficulties because this potential is fitted for bulk values. We will return to this problem later.

2.1.2 Tersoff potential

The second potential widely used for the modeling of silicon is the Tersoff potential. This empirical potential was introduced by Tersoff in 1986 [15] in order to increase the accuracy of some potentials introduced earlier in an attempt to describe the Silicon. For example, the Keating potential [65] was very suitable to describe a crystal of Silicon with a small distortion but when the reconstructions are more drastic, the bond lengths of re-bonded atoms are inaccurate. The Keating potential is very suitable for describing phonons or elastic distortions.

Tersoff has built his potential because existing potentials describe well the tetrahedral silicon but fail to describe non-tetrahedral forms in a satisfactory manner. The Tersoff potential is not a two- and three-body potential like the SW-potential. It has the form of a Morse pair-potential with the bond-strength parameter depending upon local environment. The Tersoff potential is the first one which incorporates the structural chemistry of covalent systems like silicon. This potential was introduced after the work of Ferrante, Smith, and Rose who have shown the universal behavior of calculated binding-energy curves for solid cohesion and chemisorption [68, 69] by use of a three-parameters rescaling. The work of Abell on this universal behavior assuming a Morse or Morse-type potential convinces definitively Tersoff to built his potential using a Morse pair-potential.

As we have said before, there are four updated Tersoff potentials by Tersoff himself. The first version of this potential [15] that we will denote (T1), was a first approach to build a potential able to model tetrahedral bonds without the use of a two- and three-body potential. Indeed, Tersoff was suspicious about the capability of a many-body type potential to describe a wide range of bonding geometries. Stillinger and Weber themselves have concluded, after a deeper study, that they are unable to describe the energetics of all the diverse bonding geometries with a three-body potential. This information was confirmed by the work of Biswas et al. [70].

T1 had also some problems because the energies of phonons were too high and the diamond structure was not the most favorable structure, energetically. Indeed, T1 yields a zero-energy formation for one defect (hexagonal-site intersticial) so the ground state of this potential cannot be the diamond structure. As Dodson showed in Ref. [71], the problem reflects not only a bad parametrization but also a more general problem. So, MC simulations as well as MD simulations could not be done with T1.

Tersoff has improved his first version and has built the T2 version [62]. After this version, the potential's expression is almost still the same, so for the convenience of the reader, the expression of the potential is given just

below:

$$V_{Tersoff} = \frac{1}{2}\sum_{i\neq j} V_{ij} \tag{2.4}$$

where

$$V_{ij} = f_c(r_{ij})\left[A\exp\left(-\lambda r_{ij}\right) - b_{ij}B\exp\left(-\mu r_{ij}\right)\right] \tag{2.5}$$

$$b_{ij} = \chi\left(1+\beta^n\zeta_{ij}^n\right)^{\frac{-1}{2n}} \tag{2.6}$$

$$\zeta_{ij} = \sum_{k\neq i,j} f_c(r_{ik})g\left(\theta_{ijk}\right) \tag{2.7}$$

where

$$g\left(\theta_{ijk}\right) = 1 + \frac{c^2}{d^2} - \frac{c^2}{\left[d^2+\left(h-\cos\theta_{ijk}\right)^2\right]} \tag{2.8}$$

and the cut-off function :

$$f_c(r_{ij}) = \begin{cases} 1 & r_{ij} < R, \\ \frac{1}{2}+\frac{1}{2}\cos\left[\pi\frac{(r_{ij}-R)}{S-R}\right] & R < r_{ij} < S, \\ 0 & r_{ij} > S \end{cases} \tag{2.9}$$

The major modification with respect to the former expression resides in the b_{ij} term which measures the bond order. Starting from the fact that the bond strength between an atom and its neighbors depends on the number of neighbors (more neighbors imply less strength for each bond). Tersoff argues that the most important variable is the coordination number of an atom. He understood that the final atomic configuration will be obtained by a trade-off between increasing the number of neighbors with as constraint the minimization of the system energy.

The expression for b_{ij} comes from the observation of Tersoff that with Morse functions in the expression 2.5, the cohesive energy is independent of the coordination number when $b_{ij} \;\; \alpha \;\; z^{-\frac{1}{2}}$. If it is not, the previously cited trade-off will be in favor of the most dense structure (coordination 12) or in favor of the diatomic molecule (coordination 1).

With this new expression, Tersoff obtained good results for describing energy of the diamond structure as the lowest energy than other structures as shown in Fig. 2.6.

However, there are again some problems with this parametrization which is not optimized, as Tersoff said himself. For example, as we can see in Fig. 2.6, the energy of the $\beta - tin$ structure is too high (normally $\beta - tin$ is

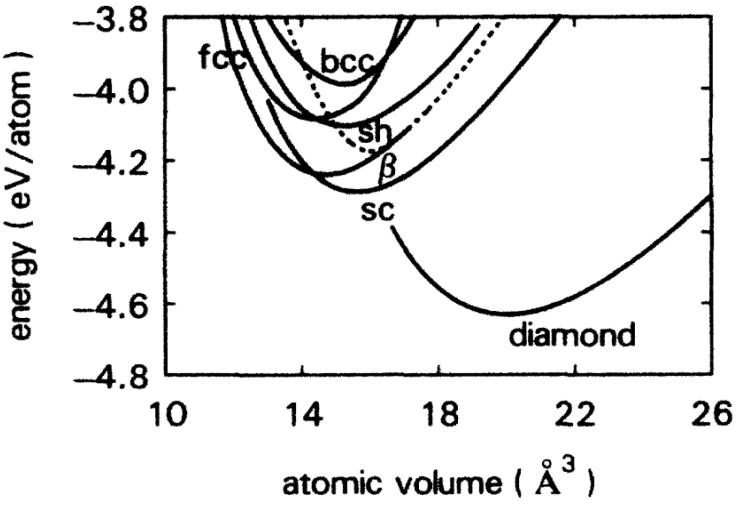

Figure 2.6: Energy curve for different structures of lattice (FCC, SC, BCC, diamond, $\beta - tin$ and simple hexagonal), using the T2 potential (taken from Ref. [62]).

the first structure which appears with the increase of pressure). Hence, at high pressures this parametrization will not be useful. With this new form, improvements have been done in the calculation of phonon dispersion curve (no phonon data were taken into account in the fitting procedure).

Results on the elastic constants (c_{11}, c_{12}, c_{44} and ζ) were quite good, apart from c_{44} which is underestimated. This underestimation may come from a weak strength for the bond-angle, as Tersoff has analyzed in his paper. Another improvement in the determination of the elastic constants was done in Ref. [63] by means of a new parametrization.

Finally, the last improvement of the potential was done by Tersoff in Ref. [16]. This new parametrization allows for consideration of multi-component systems between Si and C atoms or between Si and Ge atoms. In this thesis we have used the last version with the parameters given in Table2.2 :

The last (but not the least) important property when we do simulations is the calculation speed using this potential. Indeed, as the cutoff of the potential is relatively short, our Verlet lists are small, hence the computation of energy and other quantities is very fast, compared to the LJ potential for example.

Table 2.2: Tersoff parameters for the potential given by Eqs. 2.4 to 2.9

Parameter	Value
A (eV)	1830.8
B (eV)	471.18
λ (Å^{-1})	2.4799
μ (Å^{-1})	1.7322
β	1.1×10^{-6}
n	0.78734
c	1.0039×10^{5}
d	16.217
h	-0.59825
R (Å)	2.7
S (Å)	3.0
χ	1.0

2.1.3 Monte Carlo results

All simulations were done with a diamond structure, with at least 512 atoms (4 lattice cells in each direction) and at most 2744 atoms (7 lattice cells in each direction). For each temperature, we have done 45×10^6MC steps. We recall that without using a cluster of computers where simulation for each temperature runs on an independent node of the cluster, the time required for this simulation would be discouraging even with all the optimizations.

At the beginning of the algorithm, before the MC updating algorithm, a systematic search of the ideal lattice parameter at 0 K is carried out. This procedure is done for all potentials. Hence, plots of these curves for SW and T4 potentials are shown in Fig. 2.7.

As we can see, the lattice constant found is in perfect agreement with the experimental value ($5.43\mathring{A}$). Furthermore, the minimum of the energy found, is also in good agreement with the value given in the literature.

After this first step, the thermalization time begins. As this step of the simulation depends on the system which is studied, we do not know in advance how long it should be. So, for each temperature we have recorded the energy curve versus MC time. This huge quantity of data is very useful for several reasons. First of all, it allows us to estimate the number of MC steps necessary for the thermalization of the system. We can also ensure that no problem occurs in the runs. Indeed, some problems can appear after several thousands of MC steps and quantities such as energy or also interatomic distance, can be affected by mistakes or inappropriate choices of

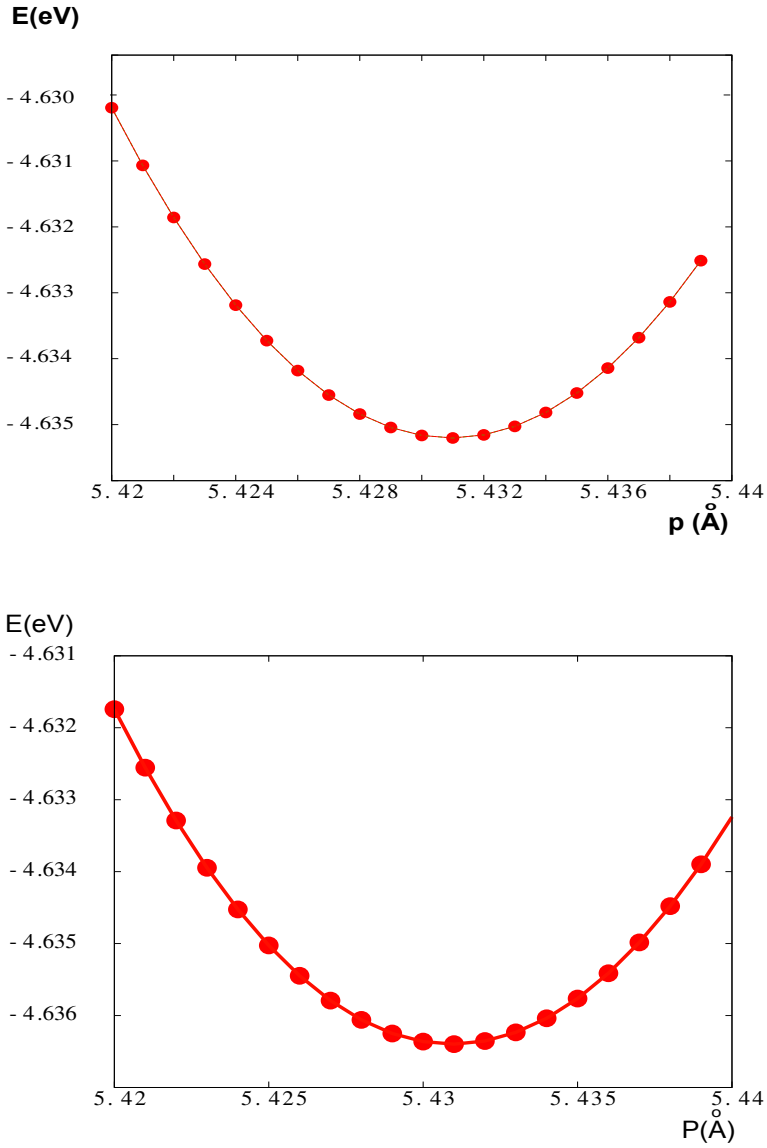

Figure 2.7: Energy versus lattice constant with the T4 (upper) and the SW (lower) potentials.

atomic motion amplitudes. The systematic investigation on all the recorded data allows us to avoid all kinds of problems. Of course, as one can imagine, this consumes a huge quantity of computer memory. The thermalization time depends also of the temperature. In order to ensure that we have a long enough equilibrating time, we have systematically taken longer than required equilibrating times for all temperatures.

As we can see in Fig. 2.8, after the melting, the number of MC steps

necessary to begin the averaging on the energy is about 8×10^6. The equilibrating time is the same for the two potentials. Hence, we average all the quantities after 8×10^6 MC steps. Averages are carried out on a minimum of 5×10^6 MC steps.

The energy versus number of MC steps is plotted in Fig. 2.8 for a system containing 1728 atoms. The curve shows a jump of the energy after several millions of MC steps. This leap, corresponding to the latent heat, comes for temperatures greater than 3200 K, using the T4 potential. Although the precision in temperature is equal to 50 K, the melting temperature is obviously too high. In Fig. 2.9, we have plotted the curve of the energy versus temperatures, using the SW and T4 potentials.

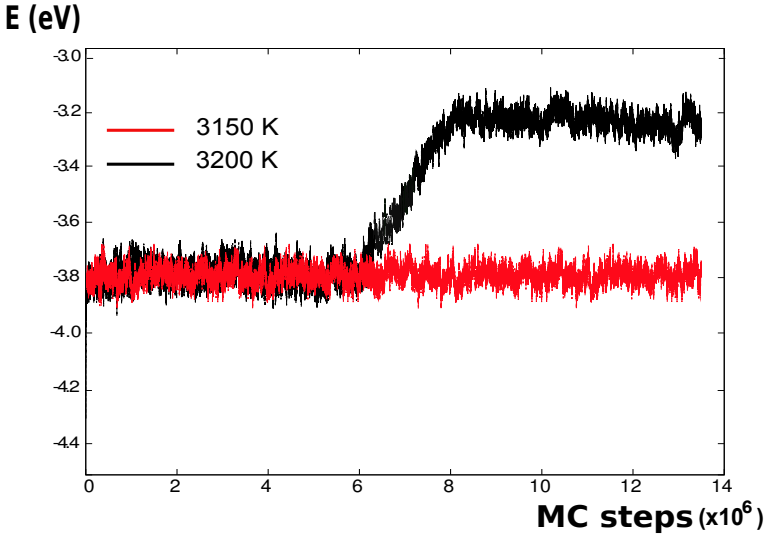

Figure 2.8: Energy versus MC steps below (red) and above (black) the melting temperature (using the T4 potential) for a Si supercell of 1728 particles (diamond 6x6x6).

As we can see, the same behavior occurs in the same range of temperatures, $\simeq 3150K \pm 25K$ for the T4 potential and $2950K \pm 50K$ for the SW potential, for the two potentials. The size effect of the simulation cell has been tested. For a 4x4x4 diamond cell (512 atoms) the melting temperature is saturated, whatever the potential used. This overestimation of the melting temperature is a well-known problem for the T4 potential (both with MD and MC techniques). The overestimation with the SW potential is less known. To our knowledge, there are no results using direct Monte Carlo simulations on this subject. Stillinger and Weber have done MD simulations with their potential, using a 216-atom cubic cell with fixed volume.

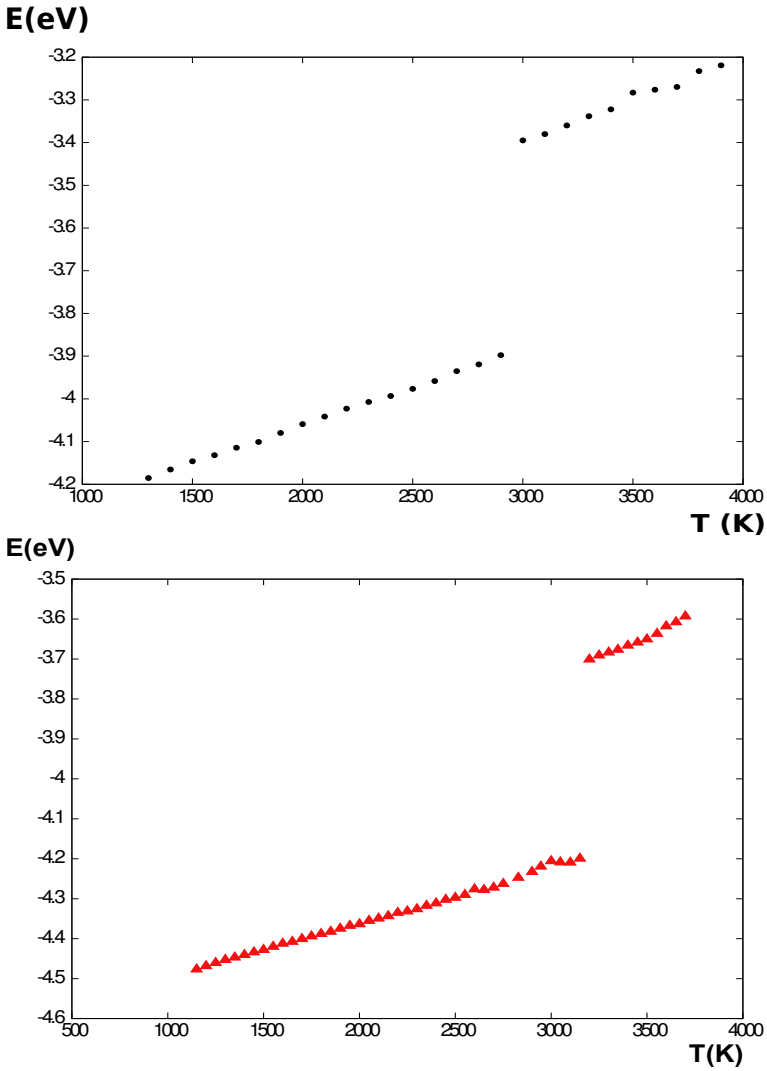

Figure 2.9: Energy versus temperature using SW (upper) and T4 (lower) potentials for Si.

We emphasize that the NPT method is more appropriate for simulations of melting than the NVT one. It is one of the major problem when one uses MD simulations. In Ref. [66], the melting temperature is around 2012 K ($T^* = 0.08$ in reduced units). In order to assign this value they take the middle of the temperature area where an overlapping of the liquid-phase energy over the crystalline-phase energy takes place (see Fig. 3 in Ref. [66]). This criterion is empirical. If we take the greatest temperature (before the overlapping region) we find 2591 K ($T^* = 0.103$) for the melting temperature which is not so far from our value ($2950K \pm 50K$). Later, Yoo et al.

[72] have done MD simulations using the SW and T4 potentials. They found melting temperatures equal to 1691K ($T^* = 0.0672$ in reduced units) with the SW and 2584K with the T4 potential (at zero pressure). They have used a coexistence's method where a solid cell and a liquid cell are put in contact. As we can see, using the same technique (MD), two melting temperatures are found. In Ref. [2], MC simulations with T4 have been performed for the determination of the melting temperature. They have used the voids-nucleated method, which is imported from the MD. This method lowers the melting temperature. If no void is used, the melting temperature is around 3047K (see Fig. 3 in Ref. [2]). This temperature is in good agreement with our result ($\simeq 3150K \pm 25K$). We did not use the voids-nucleated method because we think that in a MC algorithm, voids are naturally created with the tremendous quantity of random displacements used in our runs. For the SW potential no such voids-nucleated study exists (to our knowledge) so the comparison is impossible. We can only say that with both MC and MD techniques, the melting temperature of Si found with the SW potential is lower than the melting temperature found with T4. This behavior can be explained by a more detailed analysis of the curves shown in Fig. 2.1. Indeed, if we compare the curves corresponding to the SW and T3 potentials, we can see that the slope of the SW curve, on the right of the minimum of energy, is lesser than in the case of the T3. In other words, the dilatation is easier in the case of the SW potential than in the other case.

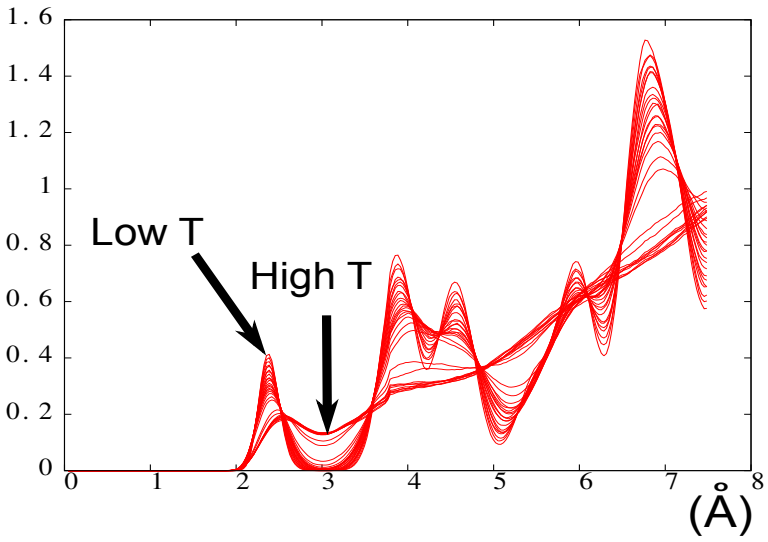

Figure 2.10: Radial-distribution function for several temperatures(1300K–3300K), using SW potential for Si.

Agrawal et al. [2] have modified β, n and h parameters to lower the melting temperature. The new values of these parameters are respectively 1.15×10^{-6}, 0.988 and -0.74525. The three parameters are involved in the b_{ij} term of the Tersoff potential. They have decided not to attempt to change the parameters A, B, λ, μ and χ because the properties of the solid such as binding energy and NN distance may be very sensitive to their modification. They did not attempt, neither, to change R, S, c and d because the resulting modification in the melting temperature is not appreciable while the density and cohesive energy are strongly affected. We have applied their modifications and tried to improve their results. It appears from this study that their modification is the optimal one. Indeed, we have tried several set of values for these three parameters without changing the cohesive energy and lattice constant.The melting temperature found with their parametrization is the lowest one. The plot of the energy versus temperature with the parametrization proposed by Agrawal et al. is shown in Fig. 2.11. As we can see, the melting temperature is lowered to $T_m = 2125K \pm 25K$, compared to the 2069K obtained by Agrawal et al. in Ref. [2] for a crystal without voids.

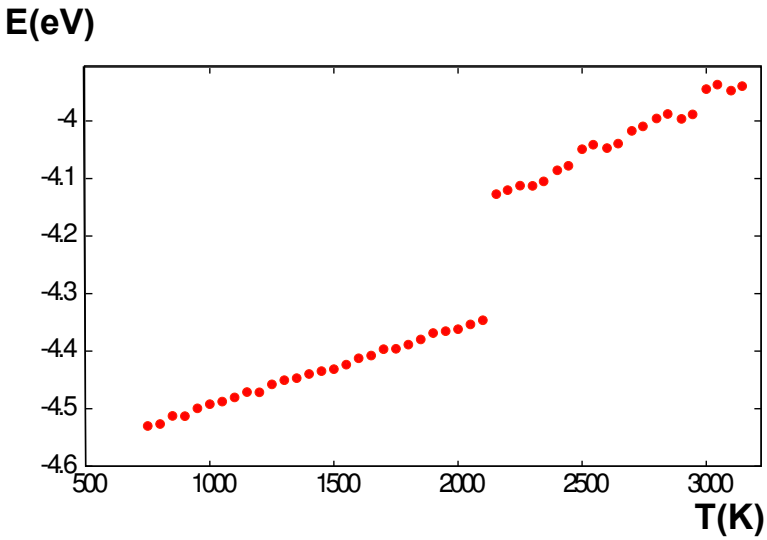

Figure 2.11: Energy versus temperature using the Tersoff potential, with the parametrization proposed in Ref. [2].

This new parametrization gives a value for the density of liquid at the melting transition equal to $2.589 \pm 0.013 g.cm^{-3}$, in good agreement with experimental value $2.583 g.cm^{-3}$. In this sense, the new parametrization improves the T4 result which is $2.225 gcm^{-3}$. The ratio $\frac{\delta V}{V_s}$, where V_s is the volume of the solid and δV the volume change, is equal to -11.8%, at

the melting transition. This result is in good agreement with experiment (-11.9%).

Unfortunately, the melting heat $\simeq 19.3 KJ.mol^{-1}$ in Ref. [2] and in our work (see Fig. 2.11) is in poor agreement with experimental value of ($50.6 KJ.mol^{-1}$). The T4 parametrization gives $44.8 KJ.mol^{-1}$ (see Fig. 2.9).

Other comparisons of the T4 and the new parametrization can be found in Ref. [2].

For the SW potential, there is no previous MC work. We have tried to modify the original SW parametrization in order to lower the melting temperature.

We have modified only two parameters namely ϵ and A. The idea was to weaken the three-body part without changing the two-body part. We have tried to find the balance between a weak three-body part in which the diamond structure is not stable, and a strong three-body part. Of course, the energy of the perfect diamond structure and the lattice constant are the two constraints one wishes to satisfy. The results are shown in Fig. 2.12.

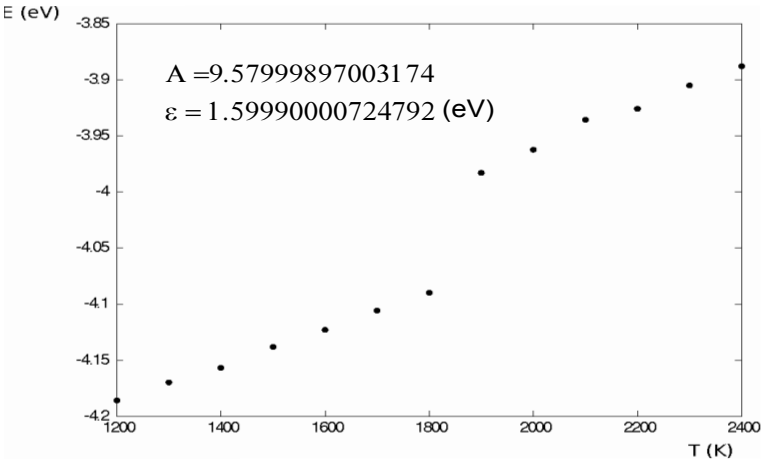

Figure 2.12: Energy versus temperature using the SW potential with the new parametrization.

As we can see, the melting temperature is lowered. With this new parametrization, the diamond structure is again the lowest-energy configuration. It is understandable because we tune the three-body part, without canceling it. As in the case of the modified T4, the melting latent heat is in bad agreement with experiments ($\simeq 9.6 KJ.mol^{-1}$) with this new parametrization. We can explain this result because since we have weakened the three-body part, the system has less energy to liberate at melting.

We did not investigate more in detail the new parametrization of the

SW potential because as Tersoff has analyzed, a potential with a two- and three-body parts cannot describe a wide range of bonding geometries.

2.2 Silver

In order to study the melting transition of Ag crystal we have used two potentials which are widely used namely the Gupta potential and the embedded-atom-method potential (EAM). This study allows us to apply our algorithm to metallic materials. In the following, we first present the two potentials used and we will show our MC results about the melting temperature of Ag crystal.

2.2.1 The Gupta potential

In computer simulations of metals, the Gupta potential is one of the most used semi-empirical potentials. There are multiple reasons for this success but the main ones are: the accuracy of its results for metals and it is easy to implement.

The Gupta potential is derived from the Gupta's expression of the cohesive energy of the bulk material and is based on the second-moment approximation of the electron density of states in the tight-binding theory. It includes implicitly some many-body interactions.

This potential has been used for the study of structural phase-transitions [73, 74, 75], thermodynamical properties [76], surface properties [13, 77] and clusters [78, 79, 80] of transition metals.

The expression of the potential of an atom at the position $\overrightarrow{r}_i$ is as follows:

$$V(\overrightarrow{r}_i) = E_0 \left[A \sum_{j \neq i}^{n} e^{-p\left(\frac{r_{i,j}}{r_0}-1\right)} - \sqrt{\sum_{j \neq i}^{N} e^{-2q\left(\frac{r_{i,j}}{r_0}-1\right)}} \right] \tag{2.9}$$

where A is a constant given in eV, r_0 the equilibrium NN distance in the bulk metal, p the repulsive-interaction range and q the attractive one. $r_{ij} = \|\overrightarrow{r}_i - \overrightarrow{r}_j\|$ is the distance between the atoms i and j and E_0 an energy constant given by the fit with the melting temperature of bulk Ag. The first sum runs over a cluster of n atoms surrounding atom i, and the sum in the square root runs over all atoms. In Eq. (2.9), the first part is a Born-Mayer pairwise repulsion energy term and the second part is the many-body attractive contribution.

The parameters used are reported in Table 2.3.

Table 2.3: Gupta parameters for Silver used with Eqs. (2.9)

Parameter	Value
A (eV)	0.09944
p	10.12
q	3.37
r_0(Å)	2.892
E_n	2.52

2.2.2 Embedded Atom Method : EAM

Murray, Daw and Baskes and several authors [81, 17, 82] have proposed a method based on density-functional theory called EAM. This potential is semi-empirical and is useful for computing the energy of an arbitrary arrangement of atoms. This technique has been widely used in the past, for modeling several problems such as point-defect properties [17], surface relaxation [17, 83] (as we will see in the next chapter), surface reconstructions [84], surface and bulk phonons [85], thermal expansion [86] and liquid structure [87] etc.

We have used a version of the EAM potential given in Ref. [88]. This version is the same as the original one, with an optional improvement which allows the possibility to study binary alloys.

The parameters of the EAM potential used in this work for silver are reported in Table 2.4.

In the EAM potential, the total potential energy is given by :

$$E_p = \sum_i \left[F_i\left(\rho_i\right) + \frac{1}{2} \sum_{j \neq i} \phi\left(r_{ij}\right) \right] \tag{2.10}$$

where ϕ_{ij} represents the pair energy between two atoms i and j separated by r_{ij}. F_i is the embedding energy function which represents the energy to embed an atom into a local site with electron density ρ_i. The electron density ρ_i has the following expression :

$$\rho_i = \sum_{j \neq i} f\left(r_{ij}\right) \tag{2.11}$$

with

$$f\left(r_{ij}\right)=\frac{f_e \exp\left[-\beta\left(\frac{r_{ij}}{r_e}-1\right)\right]}{1+\left(\frac{r_{ij}}{r_e}-\lambda\right)^{20}} \tag{2.12}$$

The embedding function have the following form:

$$F\left(\rho\right)=\begin{cases} \sum_{i=0}^{3} F_{n_i}\left(\frac{\rho}{\rho_n}-1\right)^i & \rho<\rho_n \quad where \quad \rho_n=0.85\rho_e, \\ \sum_{i=0}^{3} F_i\left(\frac{\rho}{\rho_e}-1\right)^i & \rho_n\leq\rho<1.15\rho_e, \\ F_e\left[1-\ln\left(\frac{\rho}{\rho_e}\right)^{\eta}\right]\left(\frac{\rho}{\rho_e}\right)^{\eta} & 1.15\rho_e\leq\rho \end{cases} \tag{2.13}$$

The pair energy expression between atoms i and j is :

$$\phi\left(r_{ij}\right)=\frac{A\exp\left[-\alpha\left(\frac{r_{ij}}{r_e}-1\right)\right]}{1+\left(\frac{r_{ij}}{r_e}-\kappa\right)^{20}}-\frac{B\exp\left[-\beta\left(\frac{r_{ij}}{r_e}-1\right)\right]}{1+\left(\frac{r_{ij}}{r_e}-\lambda\right)^{20}} \tag{2.14}$$

Note that MC simulations using EAM yield the bulk melting temperature at 1170K for Ag as given by Ref. [82]. In that work, Foiles et al. have computed the Gibbs free energy of solid and liquid phases. The melting point being the temperature where those two curves are crossing.

Table 2.4: EAM parameters for silver used with Eqs. (2.10)-(2.14).

Parameter	Value	Parameter	Value
r_e	2.891814	F_{n_1}	-0.221025
f_e	1.106232	F_{n_2}	0.541558
ρ_e	15.539255	F_{n_3}	-0.967036
α	7.944536	F_0	-1.75
β	4.237086	F_1	0
A	0.266074	F_2	0.983967
B	0.386272	F_3	0.520904
κ	0.425351	η	1.149461
λ	0.850703	F_e	-1.751274
F_{n_0}	-1.729619		

2.2.3 Monte Carlo results

We have used FCC samples containing 256, 500 and 864 atoms. As we can see in Fig. 2.13, the melting temperature is saturated for systems with more than 500 atoms. Hence, in the following we have used samples of 500 atoms. The number of MC steps used for the thermalization is 5×10^6MC steps and the averages were done over 30×10^6MC steps.

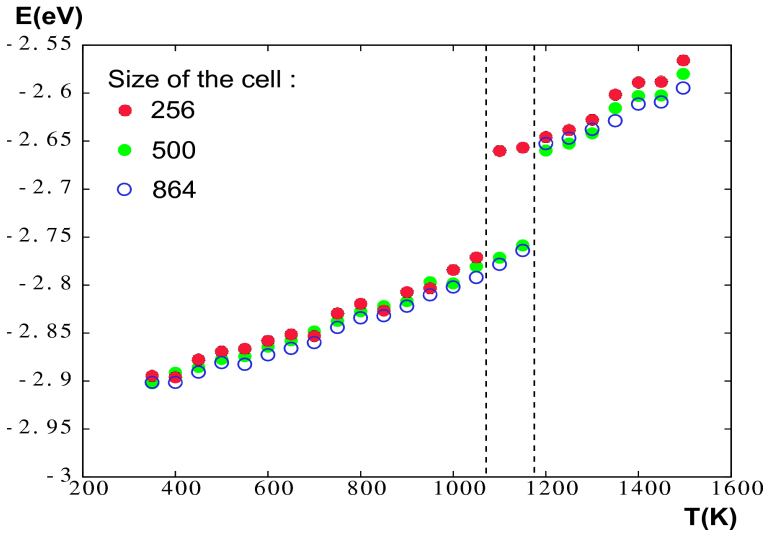

Figure 2.13: Energy versus temperature using the Gupta potential for Ag, for different sample sizes.

We have also tested the cutoff of the potential. For cutoff greater than 1.3 lattice constants (i.e. for a sphere containing more than the third-neighbor distance), the melting temperature is saturated. Hence, we have used a cutoff distance equal to 1.3 lattice constants.

In Fig. 2.14 we have plotted the curve of energy versus temperature with the two potentials used.

As we can see, the melting temperatures ($\simeq 1225K \pm 25K$ with the EAM and $\simeq 1195K \pm 25K$ with the Gupta potential) are in reasonable agreement with experiments ($T_m = 1235K$).

2.3 Conclusion

In this chapter, we have used the algorithm elaborated in the previous chapter to study the phase transition in the case of bulk 3D semi-conductors (Si) and metals (Ag). We have obtained directly from our simulations, physical

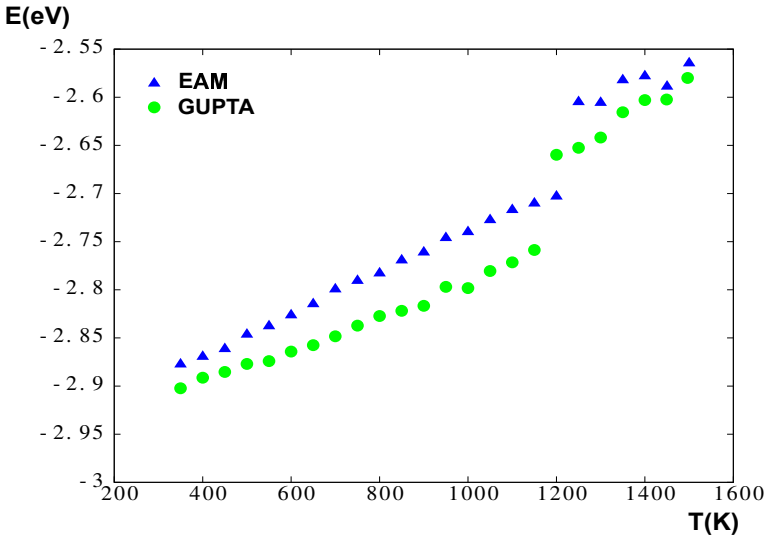

Figure 2.14: Energy versus temperature using Gupta and EAM potentials.

quantities such as internal energy, lattice constant and radial-distribution function as functions of temperature.

For Si, the two well-known potentials used (namely Stillinger-Weber and Tersoff potentials) give an overestimation of the melting temperature. For the Tersoff potential this problem is well documented in the literature. We have seen that a modification of three parameters was already done by Agrawal et al. in order to avoid this problem. But as we have seen, this modification is limited, the melting temperature found is still too high. The value of the melting heat lost it accuracy, with this new parametrization.

We have seen that, for the SW potential, modifications can be done easily. Indeed, only two parameters in the geometrical part of the potential are necessary (ϵ and A). As we have also seen, the general form of this potential is not well adapted for modeling of all bonding geometries. Hence, in the following of the thesis, when we will speak of silicene, we will not use this potential.

Finally, we have succeeded to modeling the melting transition of Ag, using the Gupta potential and the EAM potential. Indeed, a good agreement between previous results (in literature), experimental results and our results is found.

In the following chapter we will use the results concerning the bulk-3D Ag for modeling the Ag (111) surface.

Chapter 3

Melting and Lattice Relaxation of (111) Surface of Silver[1]

3.1 Introduction

The increasing interest in nanometric devices has inevitably leads scientists to search for a deeper understanding of surface physics.

It is well known that surface atoms of a material have a behavior different from that of bulk atoms, mainly because of the reduced number of neighbors and the surface geometry.

Surface effects are seen in diffusion barriers, vibrational amplitudes of surface atoms, surface phonon frequencies and surface magnetic excitations. All these properties depend sensitively on the first inter-layer distance namely the inter-layer distance between layer 1 and 2.

Different kinds of surface behavior can occur according to the nature of the material and the surface orientation. The case of metallic materials has been well studied theoretically [89, 90, 13, 91, 92, 93, 94] and by means of different experimental techniques [95, 96, 97].

The contraction of the lattice spacing has been experimentally observed by Medium Energy Ion Backscattering (MEIS) [95], Low-Energy Electron Diffraction (LEED) [96] or X-ray scattering [98]. Other methods such as elastic He scattering and electron energy-loss spectroscopy have also been used. From a theoretical point of view, Gupta has shown analytically that for classical pairwise potentials (Lennard-Jones, Morse, ...), inter-layer distance near the surface exhibits a dilatation. He has also shown that the Tight-Binding-Potential (TBP) and the so-called Gupta potential (GP) lead to a contraction of inter-layer distance at metallic surfaces.

Despite the large number of experimental and theoretical techniques used

[1] Published work, see Ref.[4]

to observe this phenomenon, there exists an unsolved question on how the contraction evolves with increasing temperature. There are two contradictory answers in the literature: X-ray scattering [98] and LEED [96] as well as molecular dynamics (MD) simulations using the Embedded Atom Method (EAM) [94] and [99] show the surface inter-layer distance always smaller than the bulk one at the same temperature, namely surface is contracted, whereas MEIS experiments [95] and ab-initio density-functional theory (DFT) calculations [100] show an anomalous thermal expansion of the surface at some temperature below the bulk melt.

Facing this long-standing unsolved question, we wanted to carry out a Monte Carlo (MC) study in an attempt to understand further these contradictory results. To our knowledge, there are no MC simulations in the literature thus far on this subject, although some MC simulations have been used to reproduce experimental patterns such as the surface blocking pattern during scattering process (see Ref. [97] for the Pb (110) surface). Given the tremendous number of numerical studies on surface problems, it is surprising that no MC simulation has been performed so far to study the variation of the surface inter-layer distance.

The purpose of this chapter is thus to investigate by MC simulation the variation of the lattice spacing between the topmost layers of the (111) silver surface with the increasing of the temperature.

In order to simulate such a behavior as accurately as possible, we have considered potentials which describe as well as possible the material. The EAM potential is often used in MD simulations and especially for the Ag (111) surface [94, 99, 101]. Working with this potential allows us to compare our results with other numerical studies using the same potential. Furthermore, the EAM potential reproduces accurately the bulk melting temperature of Ag with MC simulation [82]. On the other hand, the Gupta potential describes well the surface and cluster behaviors [78, 102, 103, 104, 105]. The melting temperature of bulk Ag is also well reproduced with this potential. That was the reason why the two potentials GP and EAM have been used for many years to simulate silver material and other metallic crystals. However, as will be seen below, the two potentials, although yielding the same result for low-temperature surface contraction, give different results at higher temperature for the surface contraction and the surface melting.

In Section 3.2 we will show a summary of the study of the (111) surface of silver, both in theory and experiments. In Section 3.3 we present our results on the (111) surface of Ag where we briefly describe our algorithm and discuss two relevant quantities to compute. Concluding remarks are given in Section 3.4.

3.2 Study of the (111) surface of silver: historic developments

The fact that the (111) surface of silver has a contraction at room temperature was well established 50 years ago. Many metals surfaces follow this behavior. There is only a few exceptions to this rule.

In 1993, Statiris et al. experimentally studied the Ag(111) surface with the Medium Energy Ions Scattering technique (MEIS)[95].

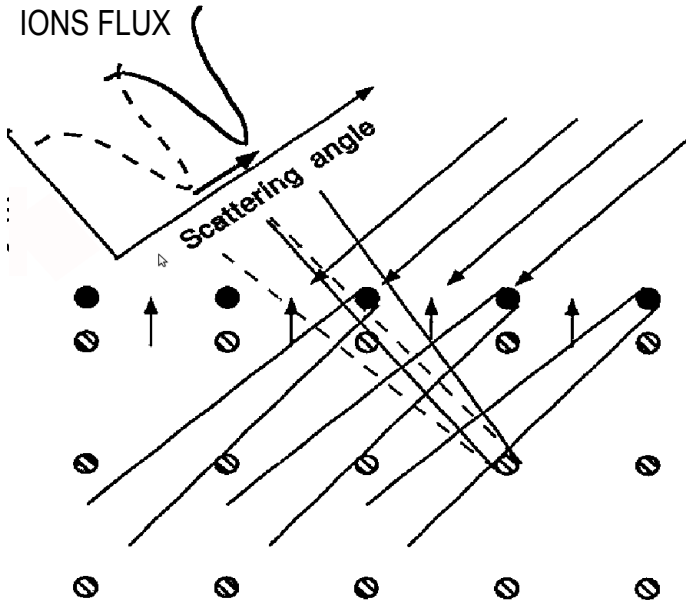

Figure 3.1: Schematic figure illustrating the MEIS technique (Taken from Ref.[95]).

The principle is the following. When atoms on the first layer of the sample are in their "bulk positions" the atoms on the second layers are visible if we look at them from an appropriate angle. The idea of the MEIS is that when the first layer has a displacement, the atoms on the second layer will be hidden by the atoms of the first layer (see Fig.3.1).

Figure 3.2 shows that the first inter-layer distance (between layers 1 and 2, 1 being the outer) is contracted until $\simeq 800K$, and after this temperature, an expansion can be observed. Hence with this technique, there is a contraction-

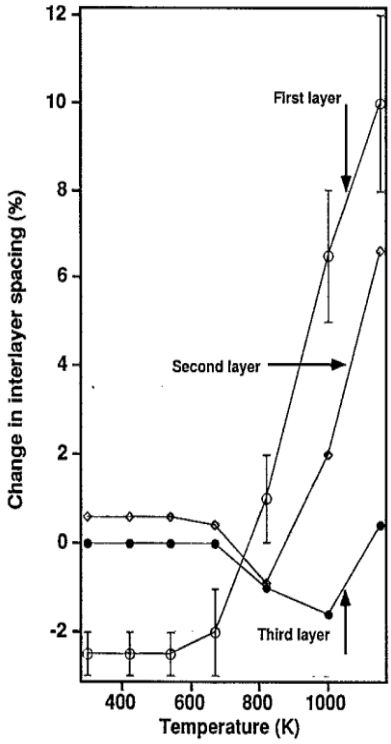

Figure 3.2: Evolution of the inter-layer contraction with the temperature, measured by MEIS (taken from Ref.[95]).

expansion crossover. The first inter-layer spacing is contracted by -2.5% of the bulk inter-layer spacing at 300K, and is in expansion at 1100K(10% of the bulk inter-layer spacing).

Inspired by this striking result, Lewis [94] performed MD calculations using EAM potential on this surface. Figure 3.3 shows his result.

As we can see in Fig. 3.3, the first inter-layer distance is contracted for all the temperatures (up to $\simeq 1100K$). Although their results are in poor agreement with MEIS experiments (value and behavior), an excellent agreement with calculations done by Methfessel et al. using the all-electron-full-potential-linear-muffin-tin-orbital method[106], is found at low temperatures. Indeed, they found $\Delta_{12} = -1.4\%$ for the first inter-layer distance. Unfortunately, the comparison between the two approaches is only possible concerning this particular point because no calculation on other inter-layer distances were reported.

In 1997, Narasimhan et al. [107] have done the first DFT calculations on the thermal expansion of the Ag(111). In this study, the changes in the first inter-layer distance Δ_{12} as a function of temperature, were evaluated

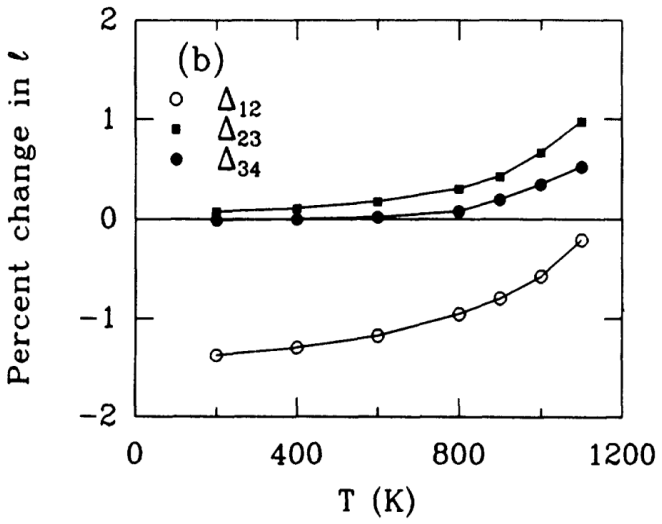

Figure 3.3: Evolution of the inter-layer contraction with the temperature, computed by EAM-MD (taken from Ref.[94]).

by the minimization of the Helmholtz free energy of the system with respect to Δ_{12}. They started with the computation of the static energies and phonon frequencies at T=0K using DFT within the local density approximation (LDA), and then extended their results to finite temperatures. In order to do this extension, they used the quasiharmonic approximation (QHA). In their simplified computation, the first layer moves as a whole. With this simplification, they find good agreement between their results and the result obtained by MEIS experiment. The anomalous expansion was attributed to the softening of parallel vibrational modes of the surface atoms. In their analysis, the anharmonicity of the perpendicular modes was not responsible of the anomalous expansion.

In 1998, Narasimhan again performed a more detailed study using ab-initio DFT, in order to clarify this problem. His results on the anomalous thermal expansion of the Ag(111) surface are in excellent agreement with the MEIS observations as we can see in Fig.3.4. He found a marked softening of surface phonon modes and a large enhancements in the mean square displacements of the surface atoms which could probably be responsible of this anomalous expansion at high temperatures.

One year later in 1999, Al-Rawi et al. [99] did an EAM-MD study of anharmonic effects on the Ag(111). Indeed, anharmonic effects are expected to be enhanced at the surface because of the broken inversion symmetry and the reduced local atomic coordination. Hence, they may lead to the

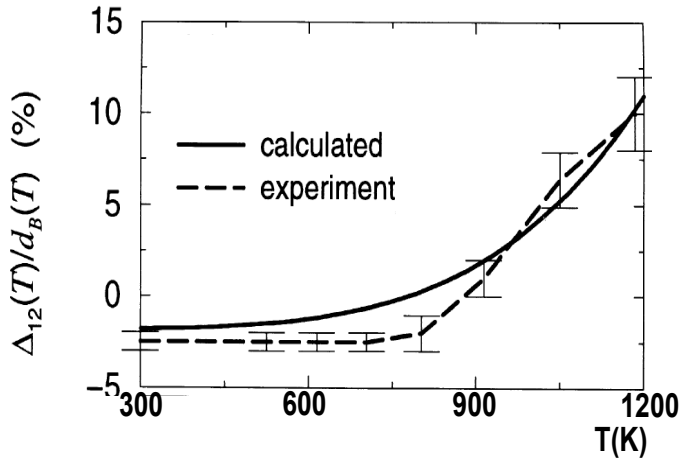

Figure 3.4: Comparison between DFT calculations and MEIS observations, for the first inter-layer distance of the (111) surface of silver (taken from Ref.[100]).

observations obtained by MEIS experiments.

In order to monitor the anharmonic effects, they have computed the mean square vibrational amplitude (MSVA). Effectively, the MSVA variations with temperature are good indicators of the strength of anharmonic effects. The expression of this last quantity is the following :

$$\left\langle u_{l\alpha}^2 \right\rangle = \frac{1}{N_l} \sum_{i=1}^{N_l} \left\langle \left[r_{i\alpha}(t) - \left\langle r_{i\alpha}(0) \right\rangle \right]^2 \right\rangle \tag{3.1}$$

where N_l is the number of atoms in layers l, $_{i\alpha}(0)\rangle$ is the equilibrium position of atom i in layer l and $\langle ... \rangle$ is a time-average and α can be x,y or z, the Cartesian components.

Their results of MSVA versus temperature show that the z-component (perpendicular to the plane) is larger than the other components. However, they found an increase in the x-component of the MSVA (in the first-three considered layers) at around 1100K. They attributed this increase to a disordering of the surface due to vacancy-adatom pair creation.

Nevertheless, the enhancement of anharmonic effects on the Ag(111) surface is not strong enough to give rise to the crossover from the contraction toward the expansion, as we can see in Fig.3.5. The contraction at 300K is equal to 1.35% which is not in good agreement with 2.5% given by MEIS experiments. Furthermore, in their study, they pointed out that the DFT calculation given in [107] did not include the full dynamical behavior of the system. They have also demonstrated that failing to include the full dynam-

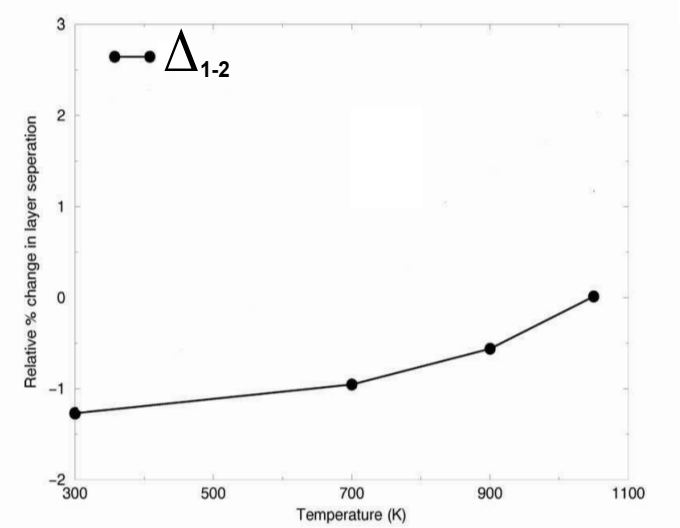

Figure 3.5: First inter-layer distance of the (111) surface of silver relative to the bulk (taken from Ref.[99]).

ics can give erroneous results on the thermal behavior of the surface.

In 1999, Xie et al.[108] reported on DFT computations using a more complete description of the dynamics but still within the QHA. They reproduced the anomalous thermal expansion observed in previous DFT calculations [107], but in a more moderate way. They found that the top-layer relaxation of Ag(111) changes from an inward contraction (-0.8%) to an outward expansion ($+6.3\%$) as the temperature increases from $T = 50K$ to $T = 1150K$.

In 2000, Soares et al. have studied the Ag(111), using Low-Energy Electron Diffraction (LEED) experiments over temperature between 128K-723K. Their results are shown in Fig.3.6 (left).

Their results exhibit a contraction at low temperatures and an expansion at high temperatures. The main problem in their analysis is that they used a temperature-independent bulk inter-layer spacing. Then, the expansion observed arises at a temperature ($\simeq 370K$) lower than in the case of MEIS. This crossover temperature increases at $\simeq 700K$ if we plot the evolution of the bulk inter-layer spacing with the temperature (see Fig.3.6 on the right).

LEED and MEIS are also in disagreement with each other about the value of the contraction of Δ_{12} at low temperatures. Indeed, MEIS shows a contraction equal to 2.5% of the bulk inter-layer spacing at 300K, while LEED leads to a contraction equal to 0.5%.

For the first inter-layer spacing, the two experimental techniques cited above are thus in agreement qualitatively but not quantitatively. For the

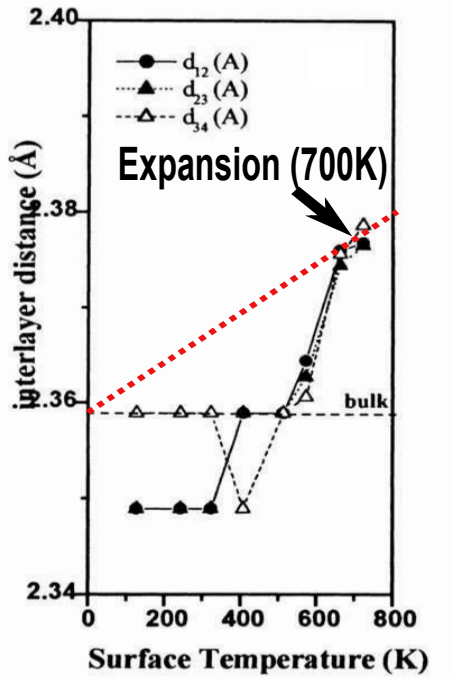

Figure 3.6: The first three inter-layer spacings of the (111) surface of silver. The original bulk line is shown with black dashed line and the modified bulk line with red dashed line (taken from Ref.[96]).

other interior inter-layer spacings, LEED gives a contraction at low temperatures for Δ_{23}, while MEIS gives an expansion. For Δ_{34}, MEIS and LEED experiments are in a quite good agreement (qualitatively) at low temperatures.

Finally, in 2001, Botez et al. have measured the thermal expansion of the Ag(111) surface by X-ray scattering. They have used synchrotron X-ray diffraction for temperatures between 300 and 1100K. They have found that Δ_{12} is essentially bulk-like at low temperatures (within the error margin). These results are very questionable given the fact that a large quantity of works shows a contraction at low temperatures.

Given this existing controversy, and in the lack of MC simulations on the subject, we decided to study this fascinating problem.

3.3 Monte Carlo Results

Before showing the results that we have obtained, we start with a presentation of two important quantities that we have computed namely the ge-

ometrical structure factor and the $\emptyset_6$ parameter. We then describe some modifications that we have made in the algorithm in order to take into account the surface of the sample. Finally we show our MC results.

3.3.1 Computed quantities

Geometrical Structure Factor

When the temperature increases, we can see, in radial-distribution function, that the peaks corresponding to the second-nearest-neighbor distance and the following neighbor peaks are broadened (almost disappeared) while the short ordering remains stable as seen by the sharp peak of first-nearest-neighbor distance. Note that the loss of the long-range-order is the loss of translational order, while the short-range-order is an orientational order. When temperature increases further, the short-range-order is lost just before the melting.

The geometrical structure factor is an useful tool to monitor the loss of the long-range-order at the surface of a sample containing one kind of atoms. It is based on the diffraction of an incident beam of particles (electron, photons X ...) by a crystal. This phenomenon was discovered in 1913, by W. H. and W. L. Bragg, when they observed the presence of some intense peaks in the diffraction pattern of crystalline structures using X-ray. This phenomenon is due to the interference of reflecting waves by crystal atoms. This behavior was not observable with liquids or all disordered phase.

As we know, when the wave-length λ (typically in the same range of the inter-layer distance), and the incident angle have certain values, the interference can occur and we can see a diffraction pattern with some intense peaks namely the Bragg peaks. The well-known equivalent criterions of Bragg and von Laue give us a condition to have realize a diffraction [46].

The structure factor is based on the von Laue formulation[2] of the interference principle applied to the topmost layers of the surface. It gives us information on the intensity of the diffracted beam; In the ideal case of perfect scattering, the value is 1 when we have constructive interferences and 0 in the case of destructive interferences.

With MC simulations, it is possible to compute this structure factor by choosing an appropriate reciprocal lattice vector corresponding to the structure studied[3]. In our case, the Ag(111) surface, the wave-vector is given by the following expression: $\overrightarrow{K} = 2\pi\left(1; -\sqrt{3}; 0\right)$. Given this vector, the computation of the structure factor is given by the following formula :

[2]This formulation uses explicitly the reciprocal lattice.

[3]Details of the determination of the reciprocal lattice vector are given in Appendix A.

$$S_{\vec{K}} = \frac{1}{N_l} \left\langle \left| \sum_{j=1}^{N_l} e^{i\vec{K}.\vec{d_j}} \right| \right\rangle \tag{3.2}$$

where $\vec{d_j}$ is the position vector of an atom in the layer, N_l the number of atoms in a layer. The angular brackets $< ... >$ indicate thermal average taken over MC run time.

The geometrical structure factor of the Ag(111) is shown in Fig. 3.7. When the sample contains different kinds of atoms, we have to consider the atomic shape factor but in this work only mono atomic systems have been tested.

The O_6 parameter

When melting occurs, orientational order is lost; this cannot be seen in radial distribution function or in the geometrical structure factor. When the temperature increases, the second-nearest-neighbor distance and the greater ones are not well defined; then the corresponding peaks of the radial distribution function disappear. Only the first peak corresponding to the first-nearest-neighbor distance is still present in the liquid state. Because the short-range-order is a orientational order, we have to introduce a parameter which allow us to measure the orientation of the different cells constituted by an atom and its nearest neighbors.

The $\emptyset_6$ (hexatic) parameter is computed as follows:

$$O_6 = \frac{\left| \sum_{jk} W_{jk} e^{i6\Theta_{jk}} \right|}{\sum_{jk} W_{jk}} \tag{3.3}$$

with

$$W_{jk} = e^{-\frac{\left(z_j - z_k\right)^2}{2\delta^2}} \tag{3.4}$$

where the sum runs over the nearest neighbor pairs and Θ_{jk} is the angle which the $j-k$ bond, when projected on the xy plane, forms with the x axis. The δ parameter is taken as one-half the average inter-layer spacing. The weighting function, W_{jk}, allows us to differentiate the "non coplanar" and the "coplanar" neighbors. With a coplanar neighbor, the weighting function takes a maximum value. This parameter has been used by several authors [99]. We have decided to use this one, in order to easily compare our results with existing results in the literature. As a remark, this is not the only way to monitor a molten layer; we also have the intralayer pair correlations which loses their crystalline shell structure and the monitoring of the energy of the

atoms in the layer which is larger in a molten layer than the energy of the atoms in a bulk crystalline plane.

We have calculated the spatial average of O_6 taken over all atoms of the surface layer and then its thermal average over MC run time. We plot the averaged O_6 parameter and the $S_{\vec{K}}$ structure factor versus temperature in Fig. 3.7.

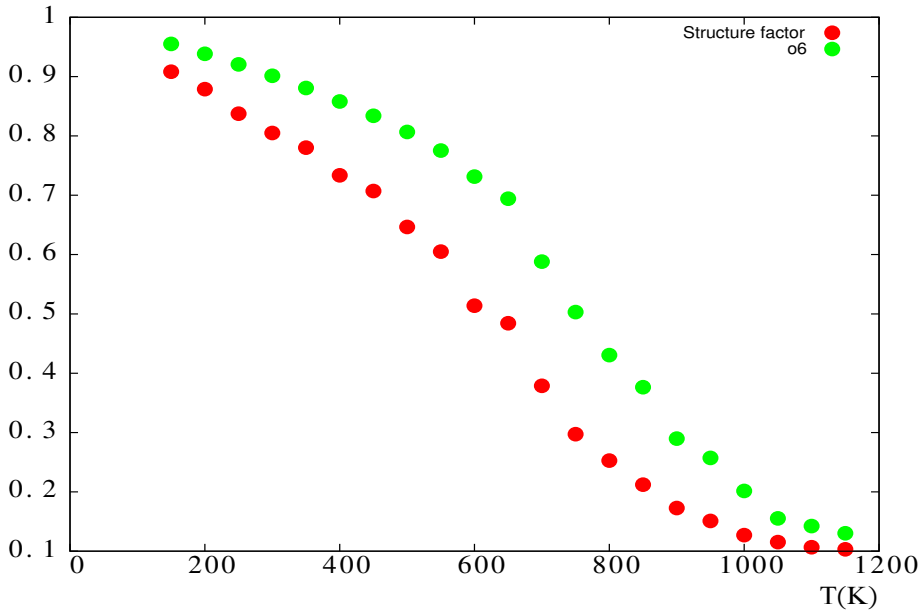

Figure 3.7: Structure factor $S_{\vec{K}}$ (green) and O_6 order parameter (red) of the first layer versus temperature for the EAM potential.

3.3.2 Model and algorithm

In this surface problem we have used xy in-plane periodic boundary conditions (xy-PBC). A picture of the system with the xy-PBC is shown in Fig. 3.8.

The number of moving layers is adjustable in order to monitor if our result depend on this parameter. The other layers of atoms are fixed. Their presence allows us to simulate the bulk condition below the surface. We have taken a number of fixed layers corresponding to a depth equal to 1.5 times the cutoff distance of the Verlet lists. Indeed, it is very important to take a sufficient number of fixed layers in order to fill correctly the Verlet lists of the moving atoms in the inner layers. Though these deep atoms are fixed, their positions depend on the simulation temperature, they are taken from

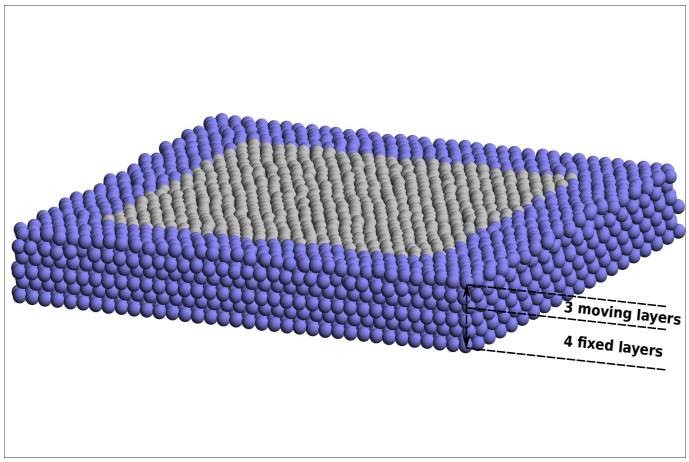

Figure 3.8: Ag(111) surface with xy-periodic boundary conditions. Atoms in the inner rectangular area belong the system while the atoms on the rectangular belt are images from the xy-PBC.

the results of bulk Ag obtained in the previous chapter. With this technique, we favor a fast convergence to equilibrium. In order to illustrate this idea, we show in Fig.3.9 the instantaneous energy E and the structure factor S as functions of number of MC steps. As seen, after less than a few thousands of MC steps these quantities reach stabilized values.

Note that by using the correct value of the lattice constant at each temperature for interior layers far from the surface, we take into account temperature effects although we neglect local fluctuations in those far layers. The effect of such an approximation has been tested by varying the number of moving layers (see below).

Of course, before using this value for the lattice constant we have compared our results with existing experimental ones. The comparison is shown in Fig. 3.10. Using the least square approximation, we obtain the linear thermal expansion $d_{nn}(\mathring{A}) = \alpha_L T + 2.87053$, with the coefficient $\alpha_L = 6.27617 \times 10^{-5}$.

The atoms of the surface layers are then moved one by one, each in a random direction with a random distance from its current position: the new position of each atom is accepted or not according to the Metropolis updating criterion. For the surface relaxation, we only compute $U_{new} - U_{old}$. It is an NPT ensemble but not with a constant V (volume) because of the open space next to the surface: the surface can contract or expand in the z-direction

We have studied a system of 256 atoms per layer in which atoms in the first three layers are allowed to relax at each MC step. From the fourth layer

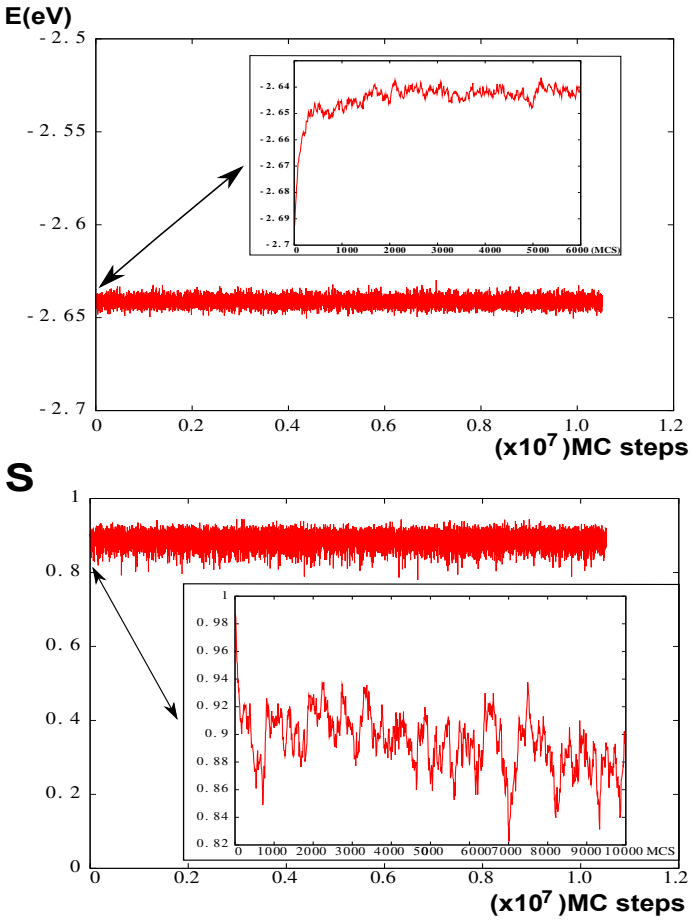

Figure 3.9: Energy at 200K(upper) and structure factor at 300K (lower) versus MC steps, for the first layer of the system. Short-time regions are enlarged for detail.

inward, the atoms dilate uniformly with temperature using the computed bulk values. For comparison, we have also considered a system of 100 atoms per layer. In addition, in the case of 256 atoms per layer, we have considered 2, 3, 4 and 5 moving layers. As we will see in the following, the thermal relaxation of the first moving layers is not significantly different for these two surface sizes, and the topmost inter-layer spacing varies very little from 3 moving layers. Therefore, except otherwise stated, we show the results for 256 surface atoms and 3 moving layers in the following. Usually, our simulations are carried out over 10 million MC steps per atoms. We discarded the first five million for equilibrating although we see above that the equilibrating time is much shorter. We have averaged physical quantities over the last five millions of MC steps to have good statistics.

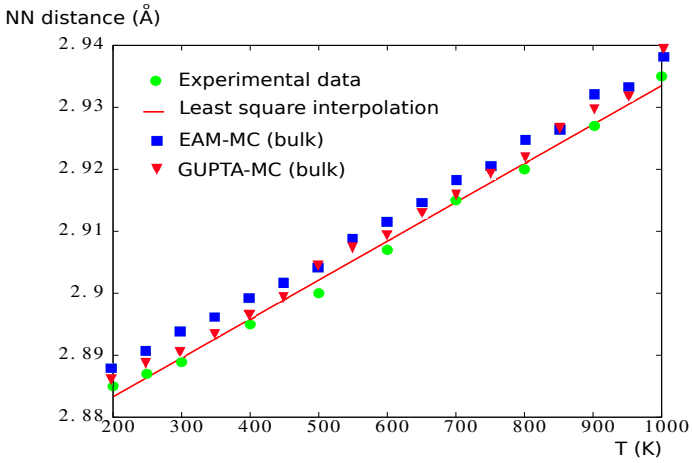

Figure 3.10: Thermal expansion by MC simulation for both potentials. Experimental data by X-ray diffraction measurements from Ref. [109] are shown by green circles, and the least square linear fit by the red line.

3.3.3 Results

Surface melting

The first step is the monitoring of the surface stability versus temperature. Of course, our calculations have been carried out for temperatures below the bulk melting temperature (T_m) because we use the temperature-dependent bulk lattice spacing below T_m shown in Fig. 3.10 for bulk atoms. Note however that very close to T_m, the thermal coefficient changes its behavior: it increases rapidly with T in a nonlinear manner. We have therefore heated the system from the ground state to temperatures between 200 K and 1200 K, just below T_m, with a step of 50 K.

The mean displacement amplitude allows us to establish the validity domain of temperatures. This quantity is computed as follows: at each MC step, we compute a spatial average of all separation distances between atoms with their ground-state node positions and then we compute its thermal average through MC steps. As we can see in Fig. 3.11, with the Gupta potential, after 1000 K the atoms undergo a sudden jump indicating a phase change: the surface becomes disordered (melted) between 1000 K and 1050 K. A study is needed to determine the precise surface melting temperature but this is not the goal of this thesis.

For the EAM potential, we have obtained a result different from that of MD simulation : the surface melting temperature takes place at about 700 K, while MD simulation finds it at 1100 K [99]. In order to see clearly this

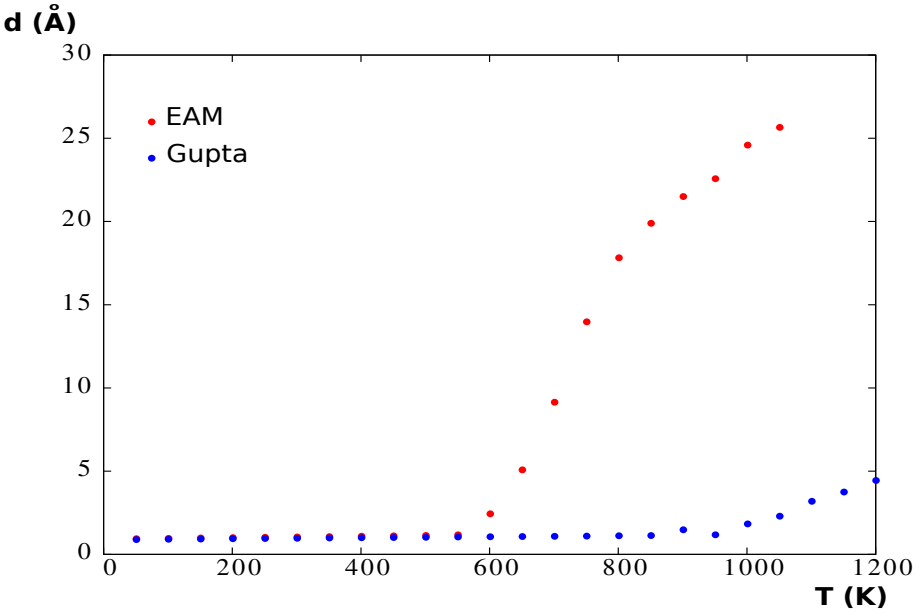

Figure 3.11: Mean displacement amplitude (in $\mathring{A}$) between atoms and their perfect ground state positions computed with Gupta and EAM potentials.

surface melting, we have computed the structure factor and the O_6 parameter for the topmost layers, with the EAM potential. Results are shown in Fig.3.7.

We observe that the long-range and short-range orders are lost at the same temperature: the melting of the surface occurs at around 700 K where both order parameters change their curvature.

Let us compare the MD and MC methods for the same potential EAM.

The MD simulation is quite different with the MC simulation : the most remarkable difference resides in the fact that MD uses periodic atom configurations. This yields a "superheating" which overestimates the melting temperature [2] in various materials such as in Refs. [110, 38, 111, 112, 36].

In order to reduce the melting temperature, these authors have suggested to introduce artificially void defects into the system to initiate the melting. Note that the determination of the melting temperature by MD is rather imprecise: for Ni, Ref. [82] gives $T_m = 1740$ K obtained by MC simulation, but the authors could not determine it with precision by the MD method (see their discussion on p. 5913 of Ref. [82]): it is estimated to be between 1600K and 1800K. For Ag, they did not calculate T_m with MD. To our knowledge, the bulk melting temperature for Ag by MD method was not available in the literature.

As said above, the MD overestimates the ordering by using ordered configurations, unlike the MC which leaves the atoms to take random positions

even at temperatures far below T_m. This may explain why with EAM, the MD gives surface melting at 1100 K (see Ref. [99]) while the MC gives it at 700 K.

Now, let us compare the results from two potentials obtained by the same method (*i. e.* MC). As seen in Fig. 2.14 of chapter 2, the EAM yields a higher energy, the temperature then destroys more easily the surface ordering. Due to a lower energy, surface atoms in the Gupta case are more strongly attached to the interior part, so we need a much higher temperature to make the surface melt.

We believe that the high "thermal stability" of surface atoms is the reason why the Gupta potential was suitable for the study of clusters of very few number of atoms: they survive in a solid state at finite temperature unlike clusters calculated with the Lennard-Jones potential [78].

For both potentials, a contraction of the lattice spacing between two topmost layers occurs but its temperature dependence is different in the two cases, as will be shown below.

Surface contraction

In order to see the variation of the inter-layer distance at the surface, we have plotted in Fig. 3.12 the z-position distribution obtained for the two potentials EAM and GP. As we can see, when the temperature increases, the three peaks which represent the z coordinates of the three moving layers, are shifted to the left, indicating a contraction toward the bulk. Note that the two potentials lead to the same behavior.

In these two z-axis distribution functions, we can see that at a given T, the deviation of the topmost layer from its perfect position is largest. This deviation becomes smaller for the next two layers and it should disappear at a few layers from the surface. This observation justifies our approximation to let only the three topmost layers to relax. Previous theoretical results and experimental data also give support to our hypothesis.

In order to examine closely the inter-layer contraction, we have plotted in Fig. 3.13 the inter-layer distance Δ_{12} between layers 1 and 2, at different temperatures. This quantity is determined by averaging over the corresponding peaks during MC simulation time. We only focus our attention on Δ_{12} since for this quantity there is a general agreement between experiments and between experiments and theories. For inner layers, there is no such agreement between experiments and theories, and even between experiments, depending on the technique used: LEED [96], MEIS [95], ...

Let us comment the results shown in Fig. 3.13. Several remarks are in order:

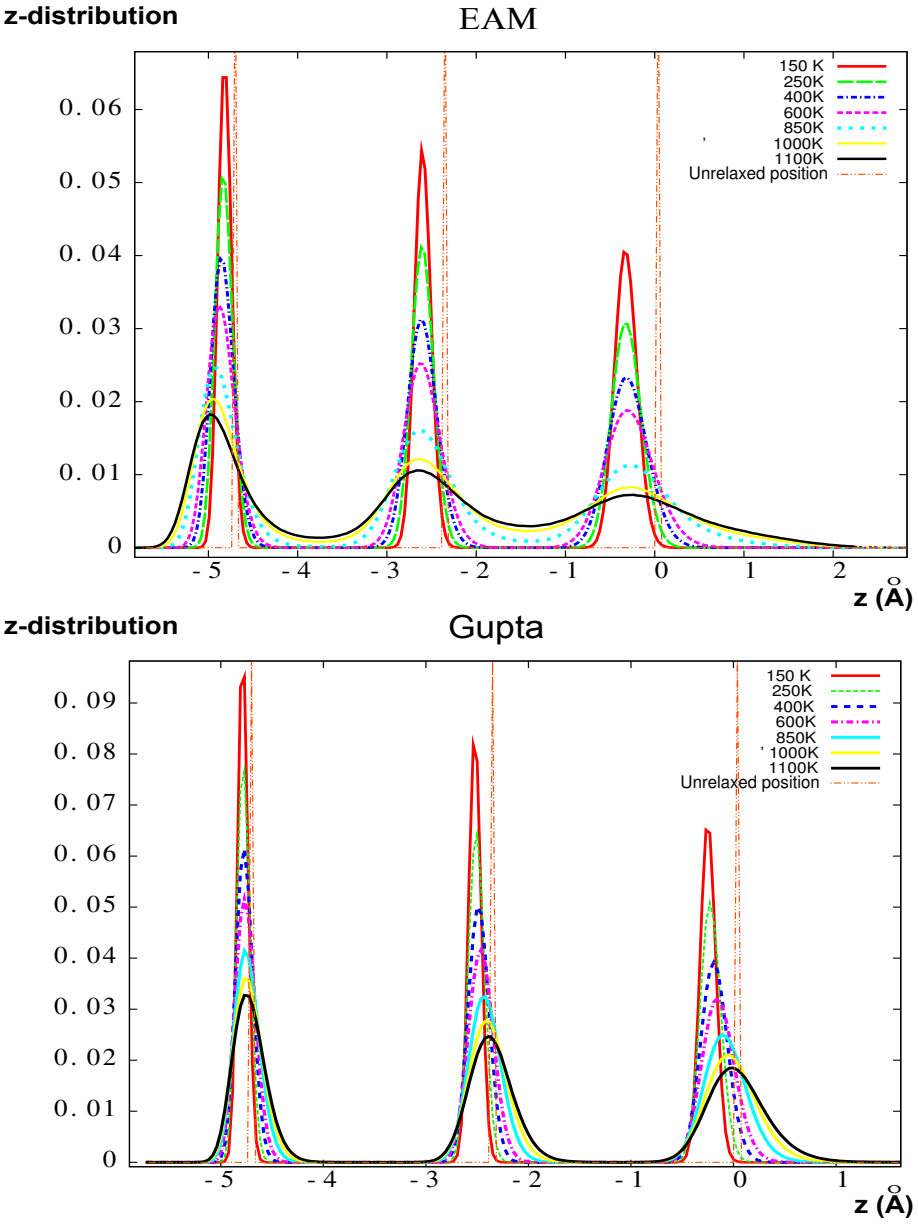

Figure 3.12: z-position distribution at different temperatures calculated with EAM and Gupta potentials. The surface at its non-relaxed position corresponds to z=0.

i. At low temperatures, for both potentials, Δ_{12} has a contraction of about 2.5% at 300 K, compared to a contraction of 0.5% with MD simulations using EAM potential [94, 99]. Experimental contraction of 2.5% was observed in Ref. [95].

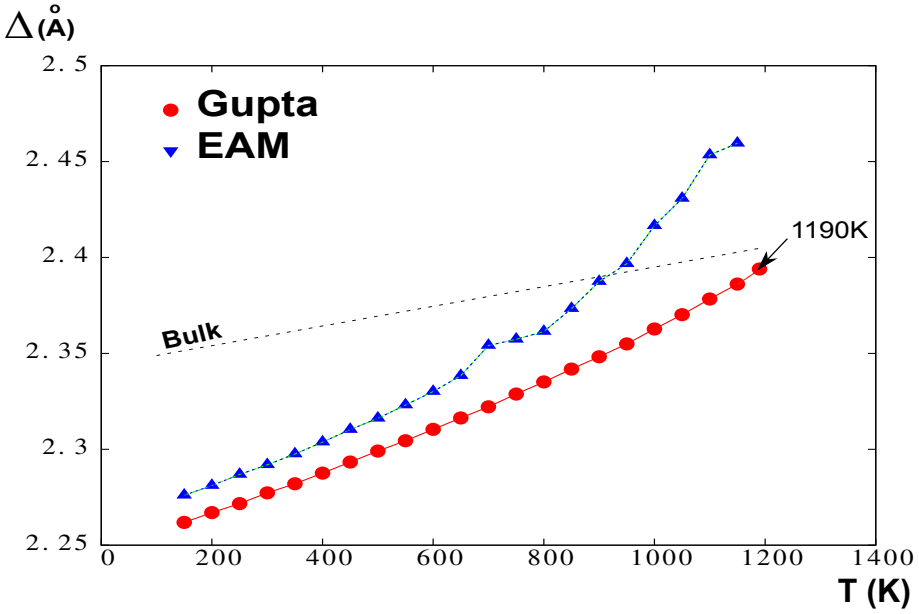

Figure 3.13: Inter-layer Δ_{12} computed with Gupta and EAM potentials. Dashed line represents the bulk inter-layer spacing.

ii. The distance Δ_{12} increases with increasing temperature: in the case of EAM potential, Δ_{12} crosses the bulk limit at $\simeq$ 900 K, indicating a surface expansion, in agreement with experimental results in Ref. [95]. This "expansion" was not found by MD simulations with EAM potential (see Refs. [94] and [99]) up to 1100 K and in LEED [96]. A surface expansion was observed in an ab-initio DFT calculation [100].

iii. As we can see in Fig. 3.13, MC results with GP do not show the above-mentioned anomalous expansion up to 1190 K slightly above the surface melting temperature observed above with this potential. We will give below an explanation about this point, at least from our MC results.

As said above, the contraction of the first inter-layer distance Δ_{12} has been observed by both MEIS and LEED at low temperatures. For Δ_{23} , the distance between the second and third layers, these two methods are not in agreement: at low T, MEIS finds a little expansion of Δ_{23} while LEED finds a contraction. Here, our computations are in agreement with the LEED results.

Let us discuss now the controversial point on the anomalous expansion of Δ_{12}, namely the transition from contraction to expansion when Δ_{12} crosses the bulk line (see Fig. 3.13). As said earlier, this has been experimentally

observed by MEIS at about 750 K [95]. We have found this with our simulations using EAM potential at $\simeq$ 900 K. Our expansion is about 5% at 1150 K, with respect to the bulk value. Let us comment on the MEIS results [95]: i) a change of behavior is observed at 670 K very similar to ours, ii) an expansion of the inter-layer spacing is observed below T_m in agreement with ours (see our Fig. 3.13), and iii) surface vibration amplitudes spectacularly increase (see Fig. 4 of Ref. [95]). This last point was attributed by the authors as anharmonic effects. We believe that such a sharp change of surface vibration amplitudes, according to the Lindemann's criterion, is a signature of a transition to a two-dimensional liquid layer. Our results on the order parameters shown in Fig. 3.7 supports this interpretation.

The disagreement between our MC result and MD result using the same potential EAM resides not only in the difference in surface melting temperatures (ours is 700 K, the MD one is 1100 K) but also in the existence of the anomalous expansion. In addition, our MC simulation finds the contraction of the surface inter-layer spacing of $\simeq$ 2.5% at low T while the MD simulation finds a contraction of 0.5% [99]. Note that we find a bulk melting temperature of $\simeq$ 1200 K by MC simulation. To our knowledge, the bulk melting temperature calculated by the MD method is not available in the literature.

For GP, we do not observe the anomalous expansion up to 1190 K as shown in Fig. 3.13. So the existence or not of an anomalous expansion depends on the potential at least with our MC results. Let us explain this as follows:

i. With the EAM potential: The surface melts at a temperature much lower than that of the anomalous expansion. As we can see in Fig. 3.13, at around 700 K, the melting of the first layer causes the apparition of a little peak but Δ_{12} is still smaller than the bulk inter-layer distance. The fact that the anomalous expansion does not occur at the melting temperature of the first layer means that the melted surface is in a "two-dimensional" liquid state in the temperature region between 700 K and 900 K. This liquid surface layer is "detached" from the remaining crystal only at temperatures higher than 900 K. More accurate experiments of surface melting are desirable to allow a better understanding of this point.

ii. With the GP: Since the surface melts at $\simeq$ 1000–1050 K (see Fig. 3.11), if there is an anomalous expansion, this should happen at a higher temperature. Given the fact that with EAM, our MC result indicates the anomalous expansion occurring 200 K above the surface melting

temperature, the same scenario with the GP cannot be possible because the bulk system melts already at $\simeq 1200 - 1235$ K.

To close this section, let us summarize here that (i) the surface melting occurs below the bulk one, but the distance to the bulk melting temperature depends on the potential: the EAM and Gupta potentials give the same bulk melting temperature but different surface melting temperatures and (ii) an anomalous dilatation of surface is possible only at a temperature much higher than the surface melting temperature.

As mentioned above, all shown results were obtained with 256 surface atoms and 3 moving layers. The surface-size effect is very small between 100 and 256 atoms as shown in Fig. 3.14. The effect of the number of surface moving layers is also very small from 3, as seen in the same figure. This is the reason why most of our simulations were performed with 256 atoms and 3 moving layers.

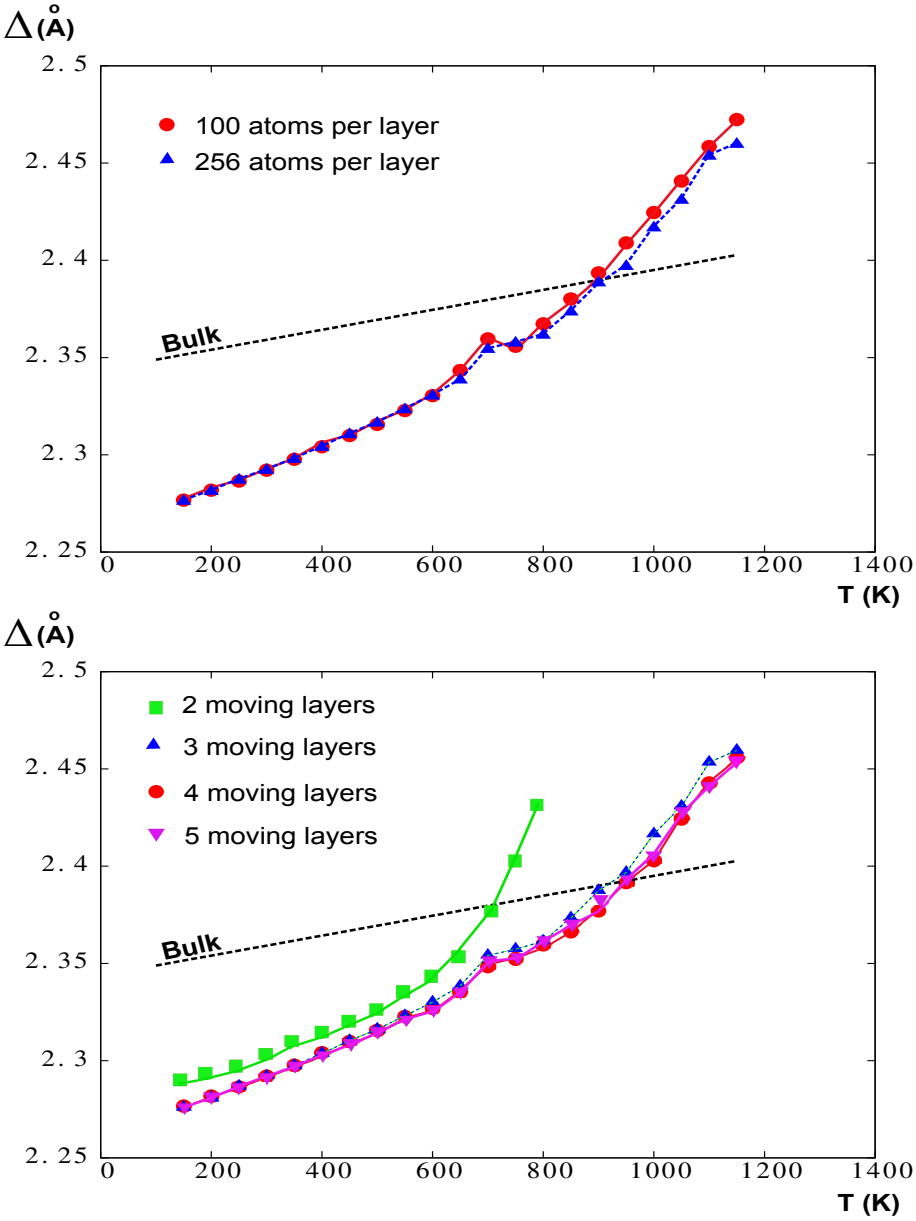

Figure 3.14: Upper: surface relaxation for two surface sizes 100 and 256 atoms. Lower: surface relaxation for 2,3,4 and 5 moving layers in the case of 256 surface atoms. From 3 layers, the results are not strongly affected.

3.4 Conclusion

In this chapter we have studied the (111) surface of silver. After a summary of historic developments on the subject, presenting different theoretical and experimental approaches which have been used during the last 50 years, we have studied the behavior of the first inter-layer distances between the topmost layers of the sample with increasing temperature, which has not been well studied before. In order to shed some light on this problem we have performed MC simulations for the first time on this subject with both EAM and Gupta potentials. Our results show two different surface melting temperatures for the (111) surface of a silver sample for these potentials in spite of the fact that they yield both the same bulk melting temperature ($\simeq 1200$ K). The EAM potential yields a surface melting at $\simeq 700$ K and the Gupta potential shows a surface melting at $\simeq 1000 - 1050$ K close to the bulk melting.

However, both potentials show a contraction of the topmost inter-layer distance at low temperatures, in good agreement with experiments and theories. Our results of the temperature-dependence of the inter-layer contraction indicate a strong potential-dependence: the variation of the contraction with increasing temperature shows a difference of the two potentials. Using the EAM potential, our MC simulations show an anomalous thermal expansion, namely the distance between the topmost layers is larger than that between two adjacent bulk layers. This can be explained by the fact that the anomalous thermal expansion occurs only at a temperature much higher than the surface melting temperature: the already-disordered surface layer is loosely attached to the crystal. This surface "dilatation" is in agreement with ab-initio DFT calculations [100] and MEIS experiments [95], although as discussed above, it was not clear if the surface in MEIS experiments was in solid or liquid state.

On the other hand, using the Gupta potential, our results show that the surface inter-layer distance varies with the temperature but it is always smaller than the bulk distance at least up to temperatures close to the bulk melting. We attribute the non-observation of a surface dilatation in this case to the fact that surface melting occurs too close to the bulk melting. The existence of surface dilatation has been observed in MEIS experiments [95] but not in LEED experiments [96] and in X-ray scattering [98]. We think that this difference comes in part from the difference of surface flatness, surface cleanness (contaminated or not) and experimental conditions.

We hope that experimentalists can resolve this important question on anomalous high-temperature behavior of the Ag (111) surface. Experiments to determine the melting temperature of the Ag (111) surface are also needed

in order to choose the most suitable potential for modeling Ag surface and Ag bulk crystal.

Chapter 4

Thermal Behavior of Stand-alone Silicene Sheet[1]

4.1 Introduction: Historic developments

Silicene is a quasi-two-dimensional honeycomb lattice of Si atoms. It is the Si counterpart of the well-known two-dimensional honeycomb Carbon material called "graphene". Due to this similarity and due to the high similar potential in application devices, we will first recall main properties of graphene and then those of silicene, before showing our results on the latter.

4.1.1 Graphene

As we know, graphene properties were theoretically predicted in 1947 by Wallace [114] who was studying the structure of electronic energy bands and Brillouin zones of the Graphite using the tight binding approximation. In his calculations, Wallace treated the graphite as independent honeycomb lattices because of the great distance between the planes of carbon atoms ($3.37\mathring{A}$) in comparison with the small distance between atoms in the hexagonal cells ($1.42\mathring{A}$). With this approximation, he has given the value for the effective mass of the conductivity electrons which is $m_{eff.} = \frac{1}{18}$ of the electron mass, and the value of the resistivity of one layer of graphite $\rho \simeq 5 \times 10^{-5} ohm - cm$.

At that time, many scientists were sceptical about the existence of a C-based 2D material with honeycomb lattice. Over a period of several years, it was believed that free-standing 2D crystals could not exist because thermal fluctuations supposedly displaced the atoms with the same magnitude as the nearest-neighbor distance, destroying the crystalline structure at finite temperatures. Furthermore, for a long time, experimental growth of thin

[1]Submitted work, see [113]

films was limited to a certain thickness much larger than one monolayer. Hence, the possibility to produce a 2D material was quite inconceivable.

In 2004, graphene was finally isolated by Geim and Novoselov for which they obtained the Nobel prize of physics in 2010. In Ref. [115], a few multilayer films of graphene (1,2 or 3 layers) have been produced with a remarkably high quality. Since then, graphene has drawn the attention of the whole scientific community. This material is found to be metallic and stable under ambient conditions. Geim *et al.* have shown that it exhibits a strong ambipolar field effect which can be induced by applying an external voltage. Depending on the applied voltage, the concentrations of holes and electrons are modified, hence, the conductivity of the material changes. Furthermore, the huge concentrations of electrons and holes (up to $\simeq 10^{13}$per cm^2) and the measured room-temperature mobilities (up to$\simeq$ 10000 $cm^2.V^{-1}.s^{-1}$) are really attractive for potential devices applications. Figure 4.1 illustrates this behavior.

As we can see in Fig. 4.1, the resistivity has a peak because of the substitution of one type of carrier by another one. On the left of the peak, the system is a hole-conductor and in the right it is an electron conductor.

In Ref. [116] also reported was the determination of the carrier mobilities from field-effect and magneto-resistance measurements. They obtained mobilities μ in the range of 3000 to 10000 $cm^2.V^{-1}.s^{-1}$. These mobilities are practically independent of the temperature and they are only limited by the scattering on defects. Such high mobility values are in agreement with high μ observed in intercalated graphite [115] and in carbon nanotubes. Despite this agreement, these high values are surprising because of the small distance between the interface and the 2D gas. Furthermore, graphene offers huge sustainable currents($10^8 A/cm^2$), so applications in nanotechnology devices such as transistors are very promising.

Novoselov et al. have succeeded in the preparation of graphene using the micro-mechanical cleavage [117, 118]. In Ref. [118] it was reported that the charge carriers in graphene mimic relativistic particles. The electron transport was suggested to be governed by Dirac's relativistic equation. The charge carriers then have behaviors which are characteristic of two-dimensional Dirac fermions, namely the high conductivity of graphene and the half-integer quantization of Hall conductance occurs.

One of the most remarkable properties of graphene is that electrons at the Fermi level have an effective mass equal to zero. It is the only physical system where fermions of zero mass can be found. Of course this property is of great interest for fundamental physics.

Other remarkable properties are the high thermal conductivity and the strong mechanical resistivity (over 100 times greater than the resistivity of a

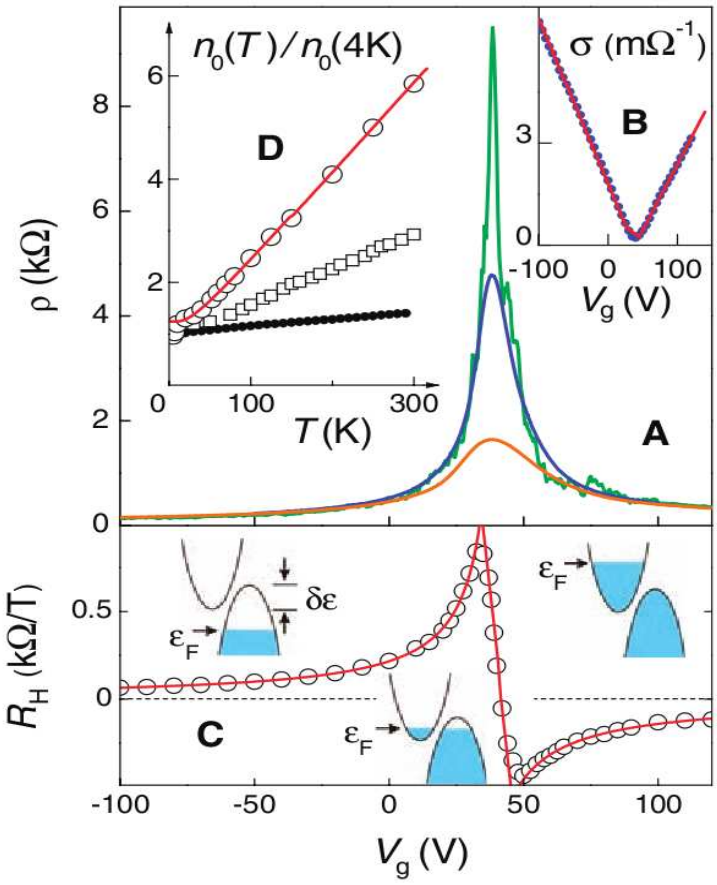

Figure 4.1: Field effect in a few-layer graphene. **(A)** Dependence of resistivity ρ on gate voltage V_g for different T=5 (top), 70 and 300K (bottom). **(B)** Change in the film conductivity obtained by inverting the 70K curve (dots). **(C)** Hall coefficient R_H versus V_g (T=5K).**(D)** Temperature dependence of carrier concentration with respect to the thickness of the film (open circles for film in (A), squares for a thicker film and solid circles for a multilayer graphene of $\simeq 5nm$. Red curve in B, C and D are the dependence calculated by the authors from their model of 2D semi-metal (taken from Ref. [115]).

hypothetical iron film of the same dimension). Graphene is also supposed to be a good material for spin transport due to a small spin-orbit interaction.

Unfortunately, the graphene is really expensive to produce in a massive way and the actual Si-based technology implies some difficulties to use graphene in the present electronic industry.

4.1.2 Silicene

As we have seen in [117], it is shown that other 2D-materials can be obtained using the micro-mechanical cleavage. The idea of a 2D material based on Si, did not take a long time to emerge in the scientific community. Indeed, one natural question that the scientific community has asked is the following : does the other group-IV elements in the periodic table (namely Si and Ge) have a stable 2D honeycomb structure?

This question was asked before the first synthesis of isolated graphene, as we can see in Ref. [119]. Takeda and Shiraishi did a theoretical study of Si and Ge analogs of graphite using first-principles total-energy calculations. In Ref. [119] it was theoretically proved that Si-based honeycomb structures prefer to form the corrugated stage (see Fig.4.2).

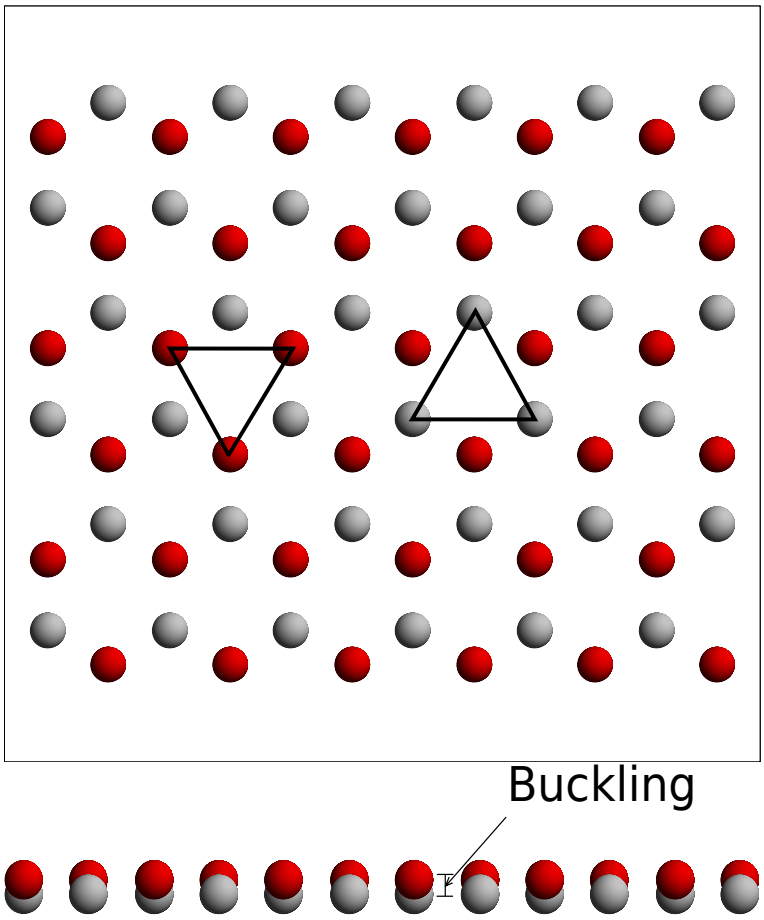

Figure 4.2: Illustration of a buckled honeycomb lattice. Top-view *(upper)* and side-view *(lower)* of the honeycomb 2D-lattice

As we know, the honeycomb lattice is formed by two inverted triangular lattices (see the upper part of Fig. 4.2). The corrugated form is a honeycomb lattice formed by two triangular sub-lattices which are not in the same plane (see the lower part of Fig. 4.2).

In 2009, Cahangirov et al. studied two- and one- dimensional honeycomb structure of Si and Ge by first-principle calculations of structure optimization, phonon modes and ab-initio finite temperature molecular dynamics within density functional theory (DFT)[120]. Here, one-dimensional honeycomb lattices are wires composed by a few number of hexagons in width. They have shown that the Si- and Ge- honeycomb structures can be stable if they are buckled. Indeed as we can see in Fig.4.3, the planar honeycomb structure seems to be unstable for the two materials.

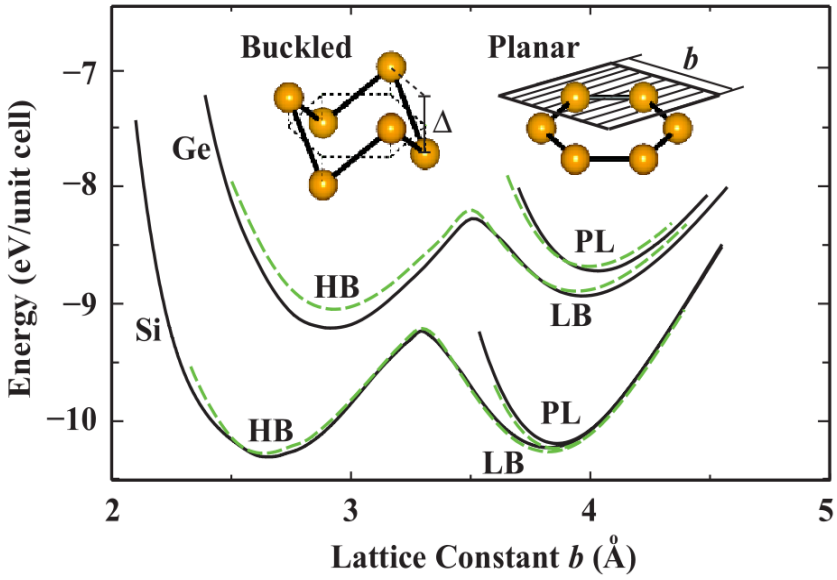

Figure 4.3: Binding energy versus hexagonal lattice constant of 2D Si and Ge calculated by LDA using PAW potential (dark) and ultrasoft pseudopotentials (dashed green). (PL : planar ; HB : high buckled : LB : low buckled) (taken from Ref. [120]).

The study of the phonon curves of the planar structure (see left part of Fig. 4.4) shows phonon modes which have imaginary frequencies in the Brillouin zone (BZ). At the minimum energy of the planar structure of Si, optical and acoustical branches hybridize. Furthermore, the (ZO) optical branch have imaginary frequencies along the $\Gamma - K$ direction of the BZ and it is merged into acoustical frequencies. After analysis of the high-bucked

(HB) structure, the structure appears unstable. It does not corresponds to a real local minima of the binding energy curve.

For the low-bucked (LB) honeycomb structure, the analysis of the phonon dispersion curves (see right part of Fig. 4.4) shows that the LB structure is the most stable. Indeed, the separation between the acoustical and the optical branches is well defined and all branches have positive frequencies. A linear behavior can be seen for two acoustical branches when $\mathbf{k}$ tends to 0. Near the Γ point, a quadratic dispersion can be seen for two acoustical branches, given the quick decrease of the force constants related to the transverse motion of atoms.

The value of the buckling computed by Cahangirov et al. is $\Delta_{LB} = 0.44$Å and the value of the nearest neighbor distance is 2.25 Å which is about 4% smaller than in the 3D diamond structure. This value of the nearest neighbor distance is confirmed by the optimization of the lattice parameter using LDA and the generalized gradient approximation (GGA) [121]. The LB structure of Si corresponds to local minima on the Born-Oppenheimer surface [122].

They have also computed the electronic band structures and corresponding density of states of LB Si (see Fig. 2 of Ref. [120]). It was shown that similarly to graphene, π and π^* bands of LB Si are semi-metallic as they are crossing at K and $K^{'}$ at the Fermi level. They also evaluated the Fermi velocity and they have found $\simeq 10^6 m.s^{-1}$ which is close to that calculated for graphene using the tight-binding band.

The linear dispersion of the band energy at the K point of the BZ seems to be insensitive to the low buckling. Indeed, in the calculations done by Lebègue et al. [121], the honeycomb lattice is supposed to be flat (graphene-like) and they have found a linear dispersion like it was found in Ref. [120] with a buckled structure. This result was also shown in Ref. [120] (Fig. 2), where energy band structure of Si in honeycomb lattice was compared between the HB, PL (planar) and LB honeycomb structures.

Finally they have considered zigzag and armchair nanoribbons of several sizes. They have observed that a ribbon of width $n = 7$ (where the width is the number of Si atoms in a continuous chain between two edges), preserves their LB honeycomb structure upon structure relaxation (for both zigzag and armchair). On the edge the buckling is weaker than in the inside.

Similarly to graphene nanoribbons, the band gap E_G shows an oscillatory behavior with the ribbon width n [see Fig.3 (c) and (d) of Ref. [120]].

Another study of the armchair nanoribbons of Si and Ge can be found in [123].

A molecular-dynamics study of silicene nanoribbons can be found in [124]. In this study, classical MD simulations using an atomistic many-body poten-

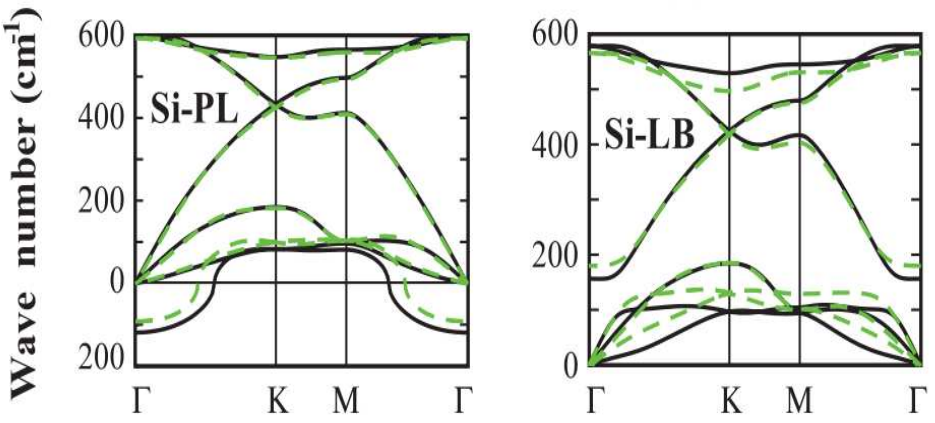

Figure 4.4: Phonon dispersion curves obtained by force-constant (black) and linear response theory (dashed green) (taken from Ref. [120]).

tial function at low and room temperatures has been done, with finite and infinite lengths for the ribbons. The main result of this paper is the tubular structures that can occur at room temperature for the silicene nanoribbons with finite length. The many-body potential used in this work is the combination of a LJ potential for the two-body part and a three-body part given by the Axilrod-Teller function. As we have seen in Section 2.1.1, a multibody potential function cannot describe a wide range of bonding geometries. Hence, the utilization of such a potential in the case of silicene can be questionable.

Experimentally, a first step was taken in 2004 when Leandri *et al.* synthesized Si nanowires on Ag(111) surface, under Ultra High Vacuum (UHV) conditions. STM images of these Si nanowires are shown in Fig. 4.5. The lengths of the wires observed are well beyond 100 nm (after mild annealing) and their width is always the same, around 16$\mathring{A}$. As we can see in Fig. 4.5 (left), there are also dots but after a long annealing they disappear, being incorporated in the nanowires. Before this study, only a few experiments concerned the deposition of Si on metals. One can mention the experiment with copper substrate where short atomic Si chains were grown on top of a surface alloy between Si and Cu atoms [126]. Before this, several experiments several experiments were based on the deposition of a metal on a semiconductor like Au on Si, for example. Si and Cu have tendency to form alloy, as it can be seen in the phase diagram of this system. Ag and Si do not have this tendency. Si/Ag system prefers a phase separation. This may explain why Si nanoribbons can be formed on Ag substrate. The deposition of Si

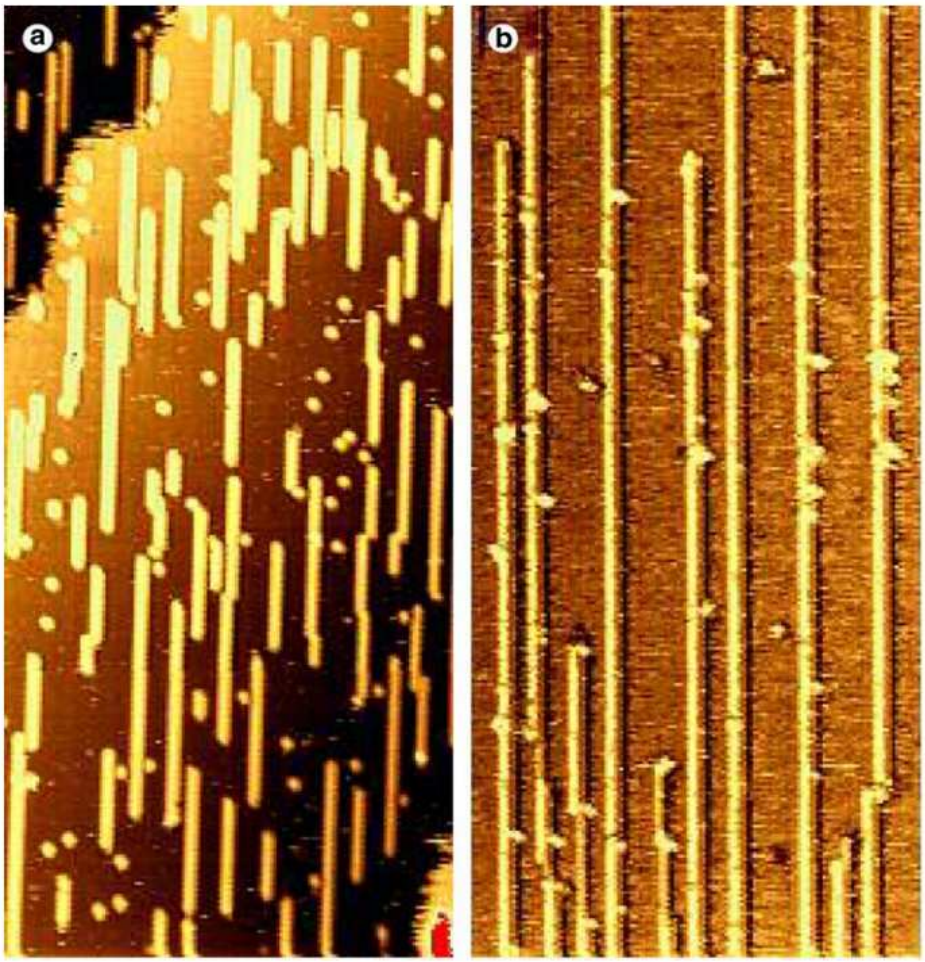

Figure 4.5: Si nanowires before (a) and after (b) annealing at 230°C (taken from Ref. [125]).

on Cu(110) shows alloy clusters. At that time, the atomic structure of the nanowires was not known.

The internal structure of the Si nanoribbons has also been elucidated [127] by Aufray et al. in 2010. By the use of high resolution STM, the silicon hexagons in honeycomb arrangement have been seen (see Fig. 4.6). In that paper, the authors have also used ab-initio DFT calculations. The starting configuration used was taken from STM images and they let it relax on the surface. They found good agreement with STM images. They have also shown that regardless of the starting configuration, Si atoms tend to form a honeycomb structure on top of the silver sample. The computed Si-Si nearest neighbor distance, after full atomic relaxation, is equal to 2.24$\mathring{A}$. The DFT

calculations also show an asymmetric corrugation in the charge density profile, in good agreement with STM profiles. They also found an arched structure of the Si nanoribbons which is probably due to the penetration of the edge atoms of the ribbon in the silver substrate. The calculated width of the ribbons is also in good agreement with the observation ($\simeq 1.51nm$ without counting the van der Waals radii of the Si atoms). Finally they have reported that silver substrate is altered by the presence of the Si nanoribbons.

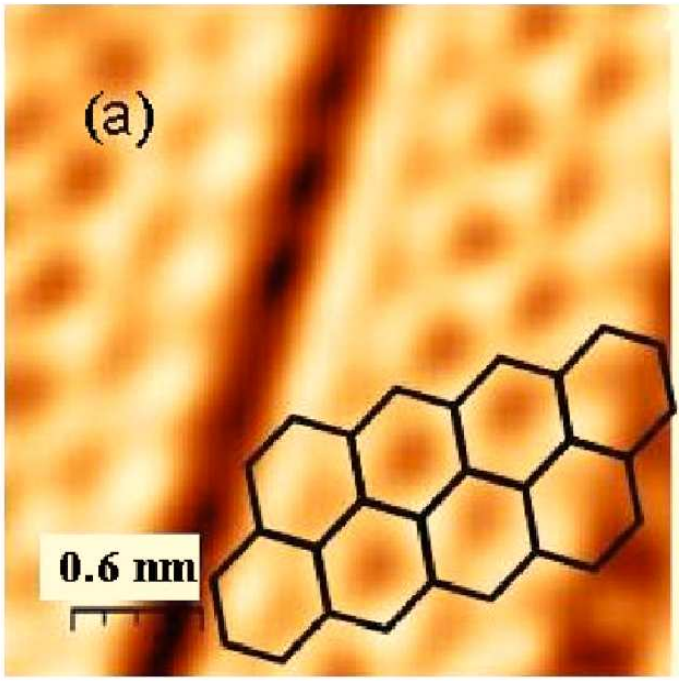

Figure 4.6: High resolution STM image of a Si nanoribbons (taken from Ref. [127]).

After this study, the Si nanoribbons are called "silicene nanoribbons".

In 2010, a study of the electronic signature of the silicene nanoribbons(Si-NRs), deposited on the Ag(110) surface, was done by De Padova et al. using angle resolved photoemission [128].

As we know, the linear dispersion of the energy band near the Fermi level is important because it is the condition to have the charge carriers with a particle with a zero effective mass (due to the curvature of the dispersion curve). This linear dispersion which forms a cone (namely the Dirac cone), is found in graphene. The aim of the study given by De Padova et al. is to see if this behavior, leading to relativistic particles, can be observed in silicene nanoribbons. Figure 4.7 shows what they have found.

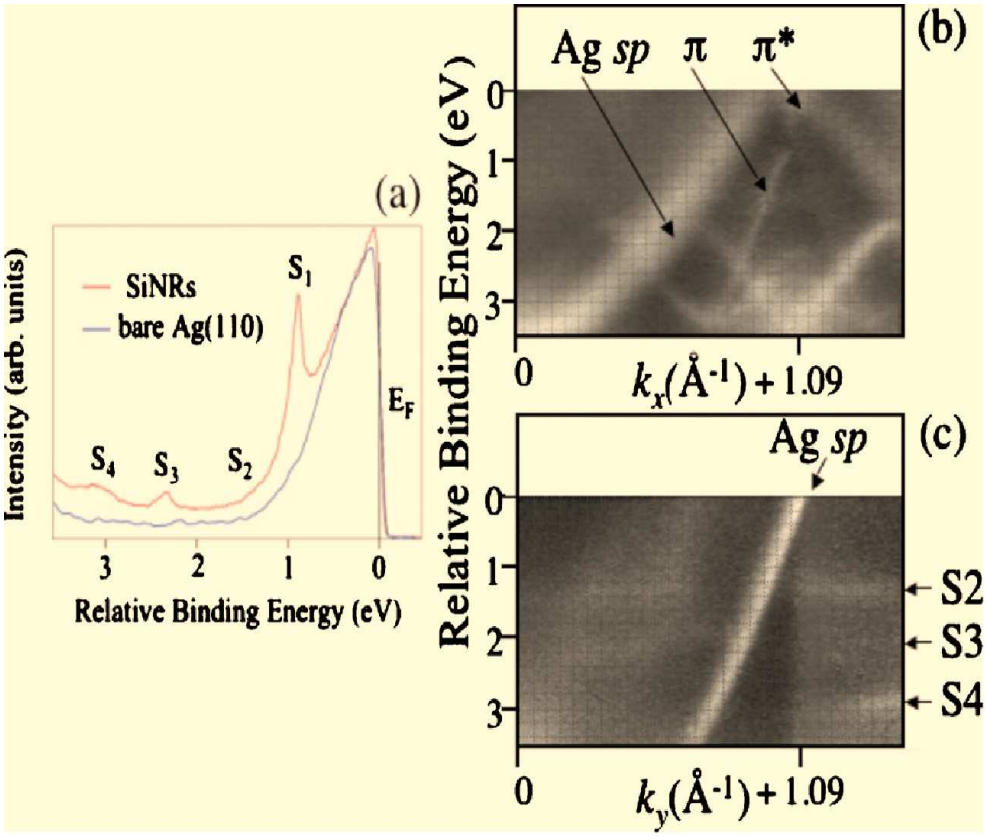

Figure 4.7: **a)** Energy distribution curves for bare Ag(110) and for Si-NRs ; **b)** Band dispersion for the Si-NRs vs. k_x (along the Si-NRs) at $k_y = 0.7\mathring{A}^{-1}$; **c)** vs. k_y (perpendicular to the Si-NRs) at $k_x = 0.35\mathring{A}^{-1}$. The photon energy used was $h\nu = 78eV$ (taken from Ref. [128]).

In Fig. 4.7, the Ag *sp* band can be clearly seen. The narrow width of the Si-NRs implies a lateral confinement which is responsible for the additional S1, S2 , S3 and S4 peaks (see Fig. 4.7). The dispersionless band behavior along k_y confirmed the 1D character of these states (S1, S2, S3 and S4).

The most remarkable result is the quasi linear dispersion of the silicon bands near the $\bar{X}$ point of the Ag surface of Brillouin zone ($k_x = \pm 1.09\mathring{A}^{-1}$). The photoemission data for k_x near $\bar{X}$, with k_y integrated from 0.55 to $0.70\mathring{A}^{-1}$ (see Fig. 4.8), shows a gap below the Fermi level between the π and the π^* branches of the Dirac cones. The authors think that this behavior is due to the interaction with the substrate. Indeed, as they have analyzed, this can be a consequence of the arched structure of the Si-NRs, provoked by the Ag(110) surface. This behavior has already been observed with graphene grown on different surfaces.

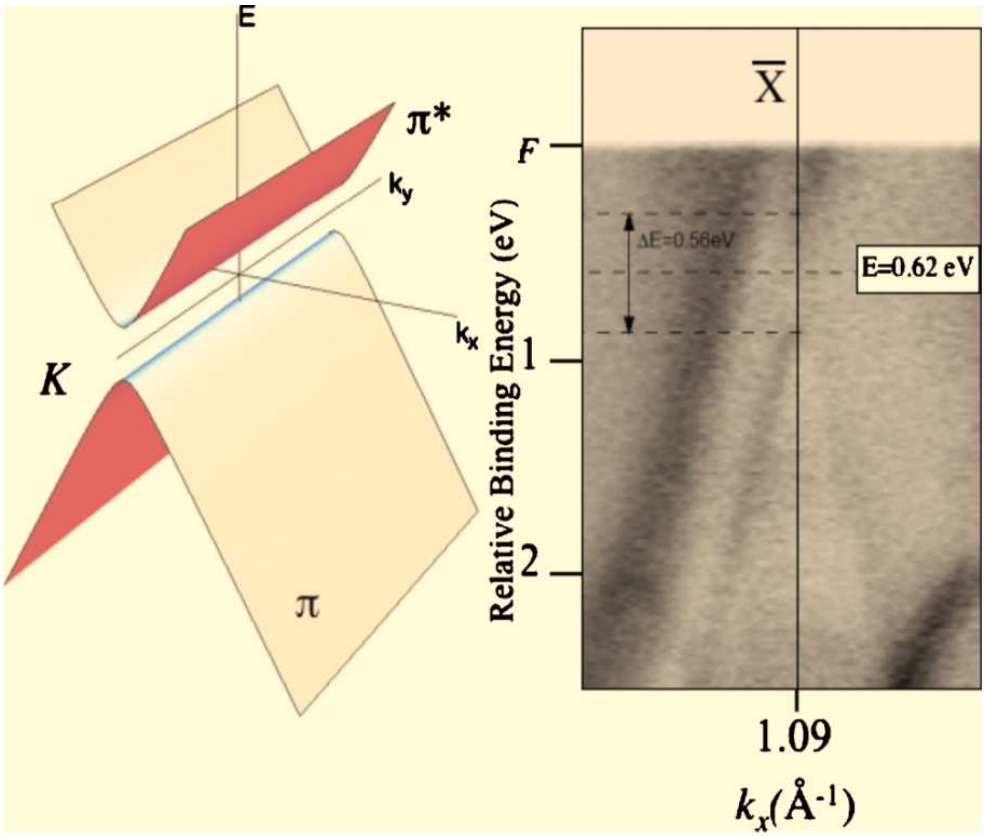

Figure 4.8: **(left)** Projection of the π and π^* cones around the Dirac points ; **(right)** Integrated signal for k_y between 0.55 to $0.7\mathring{A}^{-1}$, along the Si-NRs (taken from Ref. [128]).

The question which is asked is the following: can we grow free-standing silicene nanoribbons? The question is still open.

The next step was to synthesize a silicene sheet. A silicene sheet was grown on the Ag(111) surface (see Fig. 4.9), by Lalmi et al. in 2010 [129]. As we can see in Fig. 4.9b), the silicene sheet is buckled as it is theoretically proved, in order to be stable. The two height of the peaks concern the two triangular lattice in the buckled honeycomb lattice.

In 2012, Jamgotchian *et al.* performed a careful study of LEED patterns and STM images obtained after the deposition of one silicene sheet on the Ag(111) surface, at different temperatures in the range 150-300°C [130]. They have studied the effect of the substrate temperature on the growth of silicene because of the stringent condition on this last one, evoked by Lalmi et al. in [129].

In this range of temperature they have found three superstructures of

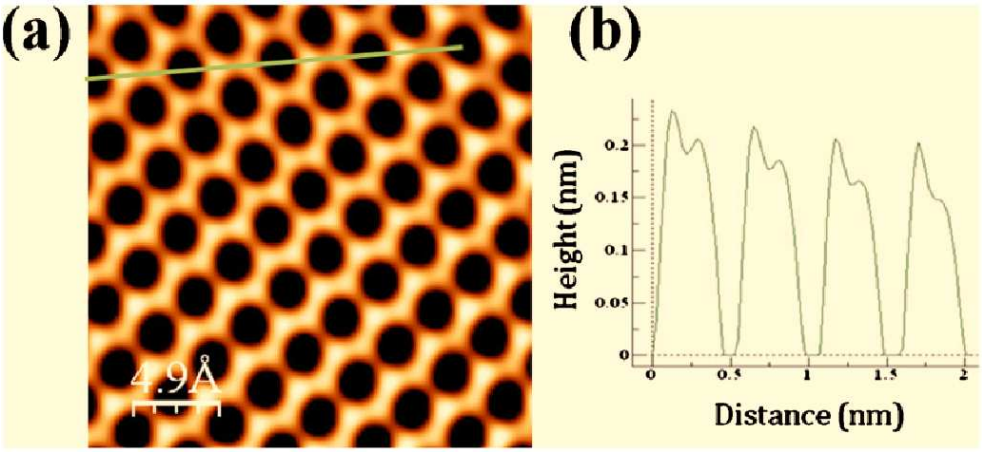

Figure 4.9: **a)** STM image of the filled-state with atomic resolution. One can clearly see the honeycomb structure ; **b)** Line profile of Si atoms along the direction indicated by the green line drawn in a) (taken from Ref. [129]).

silicene, namely the (4×4), $(2\sqrt{3}\times2\sqrt{3})$R30° and $\sqrt{13}\times\sqrt{13})R13.9°$ LEED patterns. These three superstructures are, in fact, a quasi-identical silicene layer with different rotations relative to the Ag(111) surface. With this analysis, the authors have also predicted other structures (namely the $(\sqrt{7}\times\sqrt{7})R19.1°$ and $(\sqrt{21}\times\sqrt{21})R19.1°$), which have not yet been observed.

The role played by temperature on the formation of these structures seems to be difficult to understand. Although the $(2\sqrt{3}\times2\sqrt{3})$R30° is synthesized at a temperature higher than that for the (4×4), if the (4×4) is annealed it is not transformed into the $(2\sqrt{3}\times2\sqrt{3})$R30° structure.

Another study of silicene structure on silver surfaces (Ag(100), Ag(110) and Ag(111)) has been done by Enriquez et al. in Ref. [131]. It was shown that silicene sheet growth was possible only on Ag(111) surface. On other surfaces, the silicene growth resulted in nanoribbons. The authors have shown that the silicene sheet can have different buckling values according to the superstructure formed. The maximum value of the buckling is $1.5\mathring{A}$, for one of the two $(2\sqrt{3}\times2\sqrt{3})$R30° superstructures. In this configuration, the nearest neighbor distance between two Si atoms is equal to $2.51\mathring{A}$ which is quite larger than the Si-Si distance in diamond structure.

The next step is to find a way to synthesize a stand-alone silicene sheet. This problem is still open. Hoping that this structure is possible to be synthesized, and because of the remarkable thermal properties of its carbon counterpart, namely stand-alone graphene which can be experimentally grown,

we have decided to study the thermal behavior of a stand-alone silicene sheet. This is described in the following section.

4.2 Model and Monte Carlo method

As we have seen in section 2.1, the Tersoff potential is a well-known potential for Si-based structures. As we have seen, using this potential, the melting temperature of the bulk diamond crystal of Si is over-estimated but it allows us to describe bonding geometries more accurately than the Stillinger-Weber potential. Hence, for the modeling of silicene, we have decided to use the Tersoff potential.

We report here the results of a study of the thermal behavior of a stand-alone silicene sheet using the MC method. As we have seen, this method is appropriate when one wants to study the thermal behavior of a material.

The algorithm that we have used is a modified version of the algorithm described in section 1.3. In this modified algorithm, the periodic boundary conditions are applied only in the xy-plane. In our simulations, we consider a system of 968 atoms. The algorithm is split into two main parts: the construction of the honeycomb lattice with the minimization of the lattice energy at 0 Kelvin, and in the second part, the MC algorithm using the Metropolis updating criterion [132]. For testing purposes, we have built three different 2D planar lattices of silicon, namely honeycomb, square and triangular structures, and we have computed the energy per atom in this three different configurations. The results are shown in Fig. 4.10.

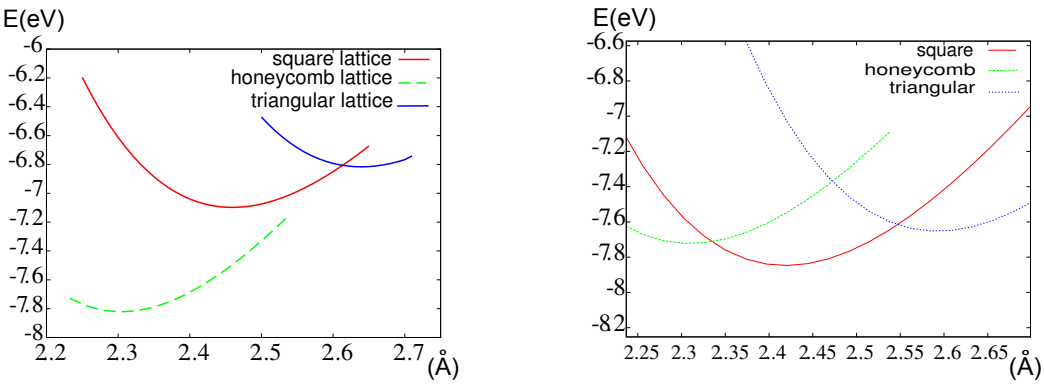

Figure 4.10: Energy vs. NN distance for 3 different lattices. **(left)**: Using the parameters given by Tersoff in Ref. [16]; **(right)**: Using the parameters given by Agrawal in Ref. [2] .

As we can see, the honeycomb lattice is more stable than the two others

at the nearest-neighbor (NN) distance $r = 2.31\mathring{A}$ in agreement with experiments, using both the original set of parameters given by Tersoff [16] and the ARK parameters [2] : the energy has a minimum for the honeycomb lattice at that NN distance. For larger NN distances, the ARK parameters give an energy minimum for the square lattice at $r = 2.42\mathring{A}$, but this distance does not correspond to the NN distance between Si atoms in the silicon crystal. We think that the ARK parameters lowers the energy with a high NN distance because at this distance and with this parameters, the competition between the two-body an the three-body parts allows an increase the number of NN neighbors . As a recall, for the honeycomb the coordination number is 3 NN , for the square lattice it's 4 and for the triangular it's 6. As the rigidity of the structure is lower than with the original parameters, we can understand that the honeycomb lattice can be deformed in a square lattice.So, at $T = 0$, we can say that both potentials give the same energy $E_0 = 7.7eV$ and the same NN distance $2.31\mathring{A}$.

Furthermore, calculations based on DFT [120] found that a buckling in the honeycomb structure of $0.4\mathring{A}$ stabilizes silicene. As we have seen earlier, the buckled configuration is the stacking of two inverted triangular planes at a small z distance. In order to check this suggestion with our potential, we have introduced a parameter d which is the distance between two triangular planes and we have computed the energy per atom as a function of d. The potential used in the present study gives the planar structure ($d = 0$) as the energetically favorable structure (see Fig. 4.11).

In order to reproduce the buckling found by more accurate calculations, one needs to re-fit all the parameters of the potential with the addition of one (such as d) or more parameters; this is out of the scope of the present study and will be tackled in futures work.

For each MC step (MCS) we move all the atoms and we relax the size of the system. The magnitudes of the atomic displacements and the variation of the system size are determined so as to obtain an acceptation rate of about 50%. This collective updating is different from the single-atom updating algorithm which is not at all efficient for melting studies. Our algorithm allows a variation ratio of the volume; so the volume can make fluctuations (dilatation and contraction) around its equilibrium during the simulation time. An important fact is that the volume variation is controlled by the Metropolis algorithm, like atom positions. For each simulation, we made approximately 3.10^7 MC steps per atom. Such long runs allow the observation of the stability of the system and to overcome the very long relaxation time near the melting. At each MC step, after updating atom positions and relaxing the system volume, we compute the following transition probability :

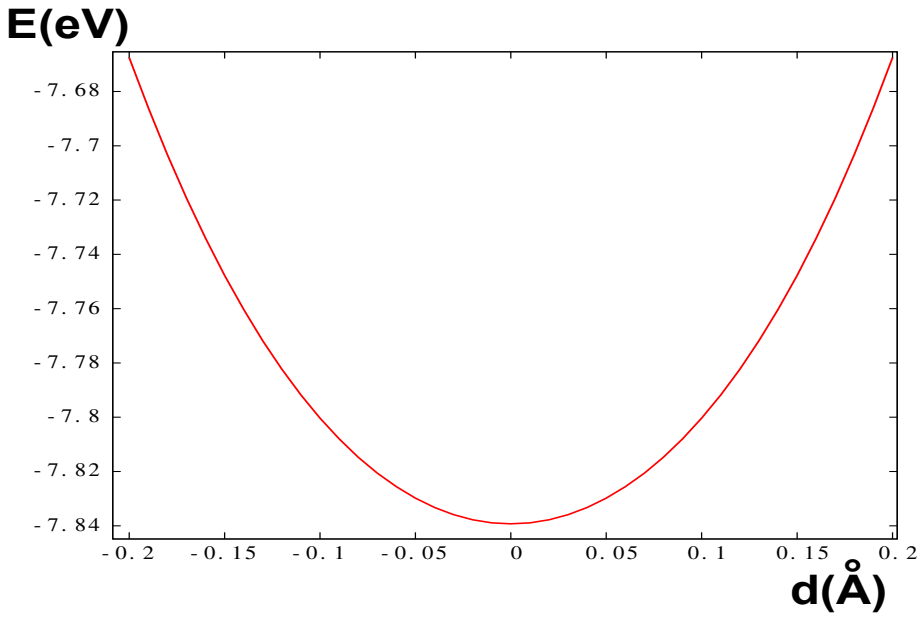

Figure 4.11: Energy curve versus buckling (d), using the Tersoff parameters given in Ref.[16]. The same behavior can be obtained with the parameters given in [2].

$$W = P(S_{new} - S_{old}) + (U_{new} - U_{old}) + N.k_B.T.ln\left(\frac{S_{new}}{S_{old}}\right) \tag{4.1}$$

where P is the pressure (0 in our case), S_{new} and S_{old} are respectively the new system surface and the old one, U_{new} denotes the energy of the system after trial updating, U_{old} the old energy, k_B the Boltzmann constant and T the temperature (in Kelvin unit).

As usual, a trivial move is accepted if a random number ξ between 0 and 1 is lesser than $e^{-\frac{W}{k_B \cdot T}}$. Otherwise, the system returns to its previous state with old atoms positions and old surface size. As said above, we tune the magnitude of displacements and volume variations so as to have an acceptation rate around 50%.

4.3 Results

For 2D systems with short-range isotropic interaction, it is known that long-range order does not survive at finite temperatures [9, 6]. Melting transition

at finite temperatures predicted by the Lindemann's criterion is for 3D crystals [5].

For the present 2D silicene, the potential is not isotropic because it stabilizes the Si diamond structure at very high temperature. As it turns out, this potential stabilizes also the honeycomb structure, as seen below.

The stability of a silicene sheet can be observed by the energy versus temperature curve, the radial distribution function, snapshots of the system, the angular distribution function or the structure factor. We will show these quantities below.

In all our simulations, we started with a perfect lattice at 0 K and we increase the temperature to the interested temperature range.

In order to have more independent data and also to have faster computation, for each temperature we compute physical quantities of the system on an independent node of a CPU cluster. As an example, we show in Fig. 4.12 the mean energy against temperature where each data point was computed by a node.

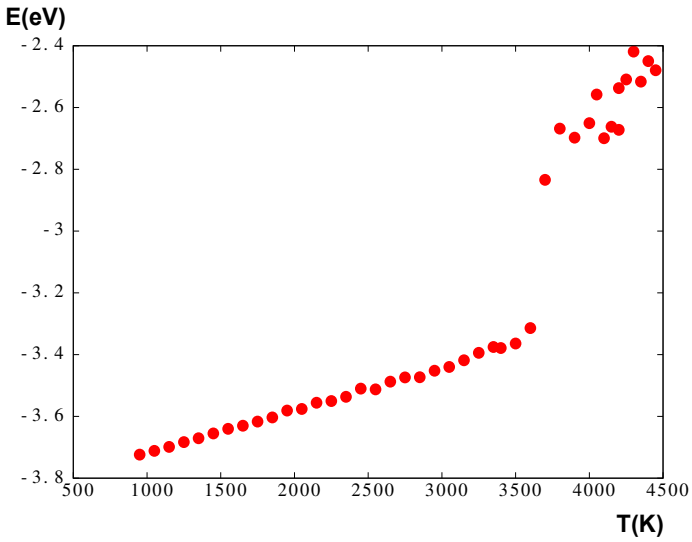

Figure 4.12: Energy versus temperature of a silicene sheet using Tersoff parameters given in Ref. [16].

4.3.1 Results using the original Tersoff parameters

At high T (see Fig. 4.12), we observe a first-order transition with a large latent heat. This transition is the melting of the sheet. Note that the melting temperature is very close to the simulated melting temperature of a 3D silicon

crystal (3600 K) using the same potential. We calculate the structure factor $S_{\overrightarrow{K}}$ (see section 3.3.1 for the definition). This "order parameter" allows us to monitor the long-range order. We show in Fig. 4.13 the structure factor versus T . As seen, the long-range order is lost at $T \simeq 3600$ K, namely at the temperature where the energy has a large discontinuity.

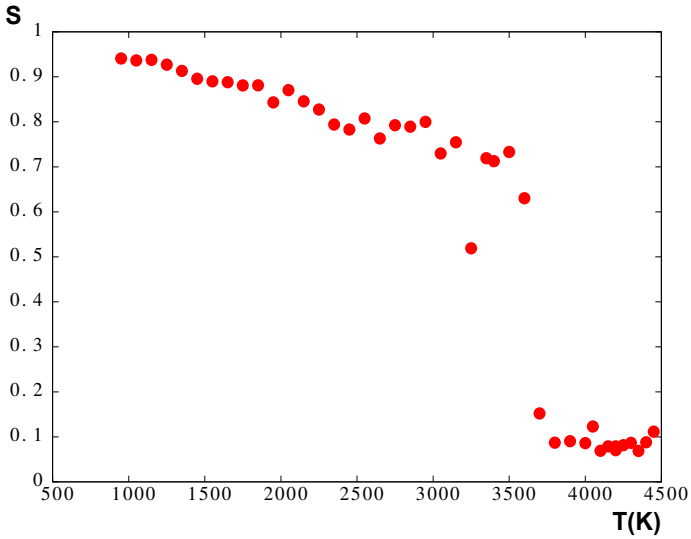

Figure 4.13: Structure factor versus temperature using Tersoff parameters given in Ref. [16].

We show in Fig. 4.14, the angle distribution function at various temperatures. The pronounced peak for $T < 3500K$ undergoes a discontinuous fall at $T \simeq 3600K$. Furthermore, the angle distribution function does not show the appearance of any peak different from that at 120°. This shows the high stability of the honeycomb structure up to melting.

The radial distribution functions confirm the transition. When the temperature increases, the radial distribution function (Fig. 4.15) jumps from a state where we can distinguish the peaks corresponding to ordered positions up to far neighbors to a state where only the peak of nearest-neighbors remains. The long-range order is lost.

In order to see how the number of nearest-neighbors evolves and indirectly how the density is modified, we have computed the integrated radial distribution shown in Fig. 4.16.

As we can see, this number decreases from 3 of the perfect crystal to 2. The latter density corresponds to a wire structure of Si in 3D space (see Fig. 4.17). This behavior has been observed in the study of the melting of graphene [133].

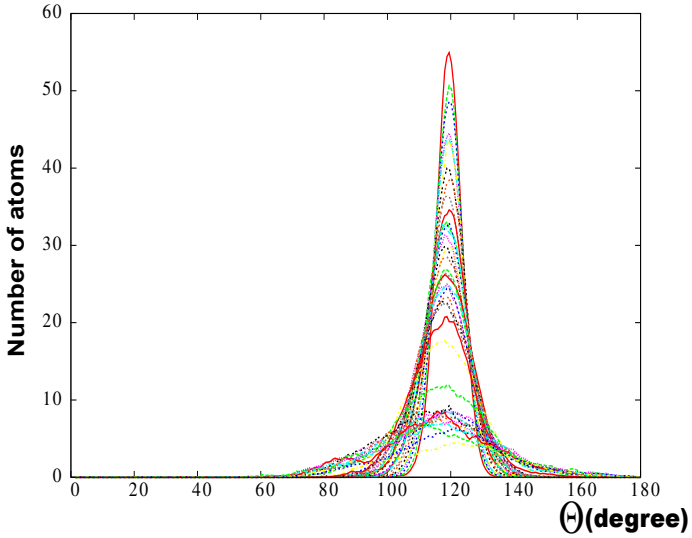

Figure 4.14: Angular distribution function at different temperatures (from 1000K to 4500K), using Tersoff parameters given in Ref. [16].

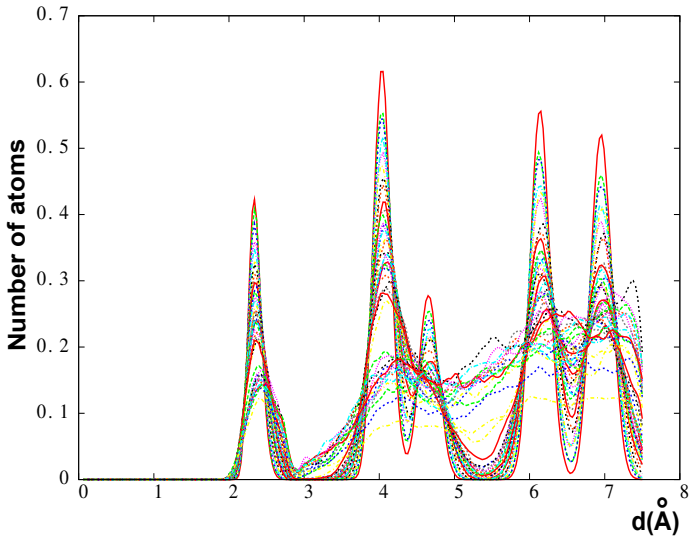

Figure 4.15: Radial distribution function at several temperatures (from 1000K to 4500K), using Tersoff parameters given in Ref. [16].

4.3.2 Results using the ARK parameters

Let us recall that the experimental value of the bulk melting temperature $T_m(exp)$ is about 1700K. The Tersoff parameters yield $T_m(Tersoff) = 3600K$ while the ARK parameters used for the bulk Si crystal gives $T_m(ARK) =$

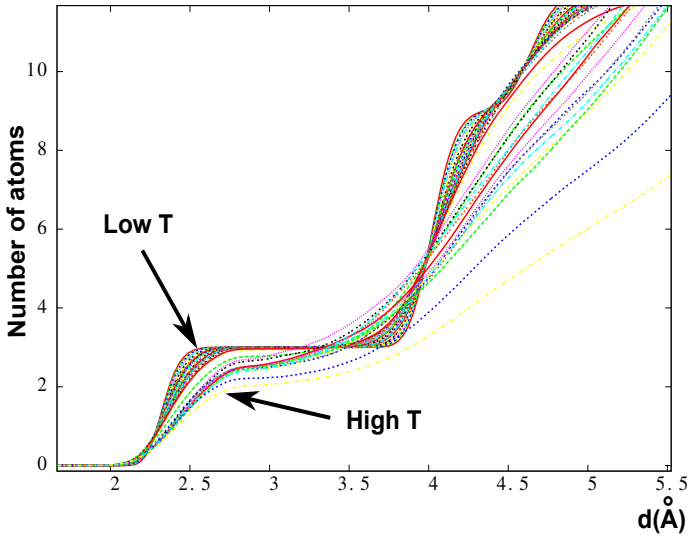

Figure 4.16: Integrated radial distribution function at several temperatures (from 1000K to 4500K), using Tersoff parameters given in Ref. [16].

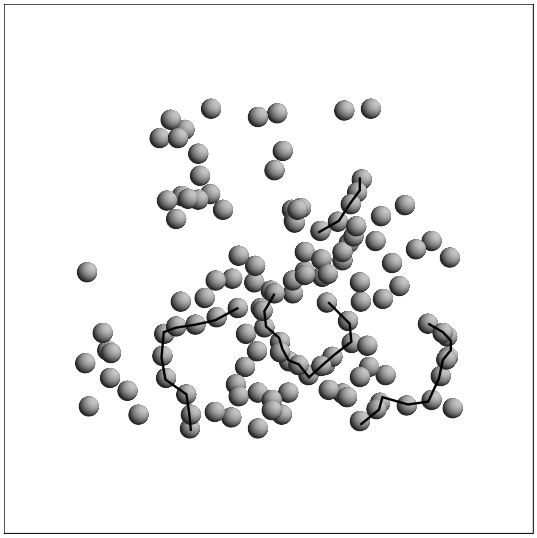

Figure 4.17: Picture of the system at high T ($T = 3800K$), using Tersoff parameters given in Ref. [16], corresponding to the wire structure.

$2200K$. So, the ARK parameters give a melting temperature closer to the experimental value. In the case of a stand-alone sheet, the original Tersoff parameters, as shown above, give a very high melting temperature, almost identical to that of the bulk 3D case, namely $T_m = 3600K$. Let us show now the melting temperature of a stand-alone sheet obtained by using the ARK

parameters. We show the structure factor in Fig. 4.18.

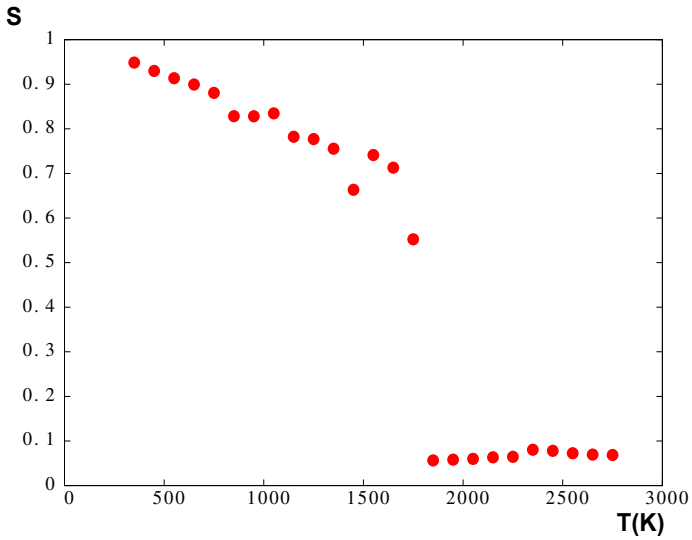

Figure 4.18: Structure factor versus temperature, using ARK parameters given in Ref. [2].

The long-range order is lost at $T_m = 1750K$, lower than that of the ARK bulk value, and less than a half of that obtained by using the original Tersoff parameters. Furthermore, the angular distribution function (see chapter 3) shows the apparition of two peaks at 60° and 90° at the same time a decrease of the peak at 120°. The honeycomb structure is thus strongly deformed to give rise to a 3D structure. For comparison, we show in Fig. 4.19 the angle distribution of the 3D hexagonal lattice.

This result confirms that the transition of the sheet to a 3D film of silicon is a structure where angles of 60° and 90° are proliferated. In Fig. 4.20 we show some snapshots of the system at low and high T where we see the 2D structure before the transition and a 3D one at high T.

The radial distribution and the integrated radial distribution shown in Fig. 4.21 indicate an abrupt transition with a jump of the number of nearest neighbors from 3 at low T to 4.6 at high T. Two groups of curves, describing the two different behaviors (before and after transition) can be clearly seen in the lower part of Fig. 4.21.

This means that the silicon sheet is reorganized in a 3D structure which is more dense than the previous 2D one. The density jump in the integrated radial distribution is in agreement with the visual observation shown in Fig. 4.20. Hence, with the modification of only 3 parameters, the ARK parametrization of the Tersoff potential leads to a completely different be-

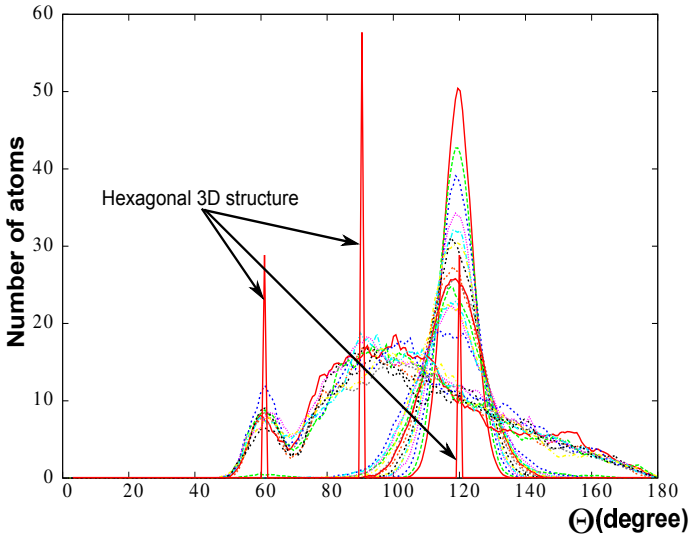

Figure 4.19: Angular distribution function for several temperatures around the melting temperature. The angular distribution function of a perfect hexagonal 3D structure is shown for comparison (using ARK parameters given in Ref. [2]).

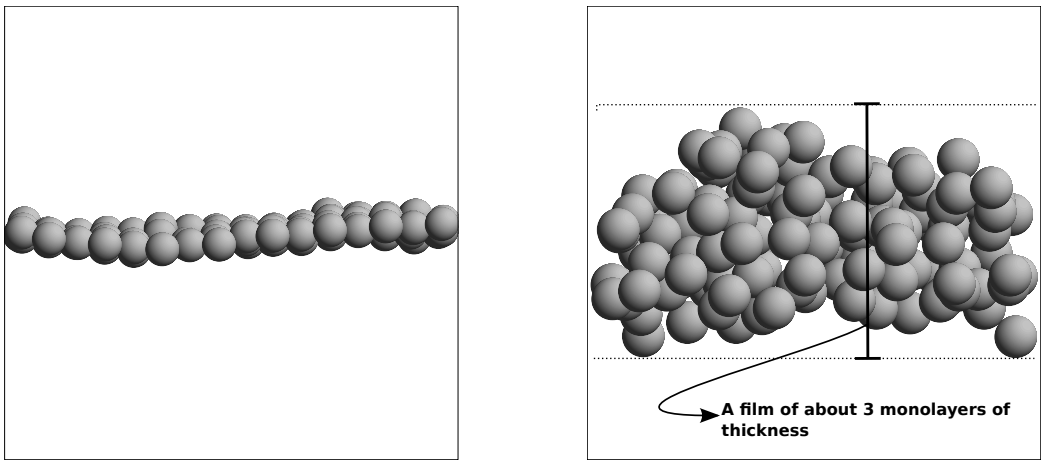

Figure 4.20: Instantaneous snapshots of the system shown by side views: the 2D structure below the transition (left) becomes a 3D one (right) above the transition temperature (using ARK parameters given in Ref. [2]).

havior of the silicene structure.

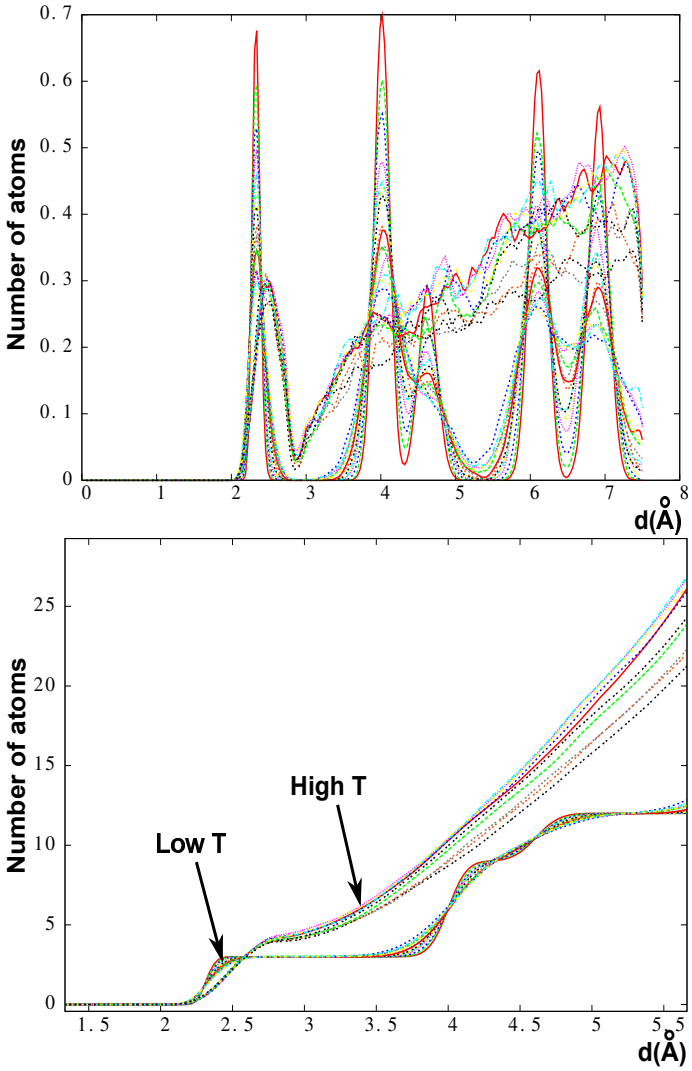

Figure 4.21: Radial distribution function (upper) and integrated radial distribution function (lower) at several temperatures around the transition (using ARK parameters given in Ref. [2]).

4.3.3 Discussion

We have studied the behavior of an infinite stand-alone silicene sheet. We have shown that the 2D honeycomb structure is stable up to high temperatures with the Tersoff potential. However, the temperature range of the silicene stability depends strongly on the parameters of that potential. The original Tersoff parameters give a too-high melting temperature while those proposed by Agrawal, Raff and Komanduri yield a melting temperature which is a half lower and much closer to 3D Si melting temperature.

For both sets of parameters, the Tersoff potential gives rise to a silicene sheet without buckling. The flatness is stable with increasing temperature. Note that a very small buckling has been experimentally observed in the silicon deposition onto Ag(111) substrate maintained during the growth at 250°C [131] as well as in a theoretical DFT study [120]. There may be several reasons to explain the difference between these works and ours. The first reason can be the limitation of the potential. As we know, the Tersoff potential was initially fitted to reproduce bulk properties such as cohesive energy, lattice parameter of the diamond structure, bulk modulus etc. The fact that this potential stabilizes the honeycomb structure is an interesting result. Indeed, the first aim of Tersoff when he decided to built his potential, was to describe the maximum of bonding geometries. We can say in that spirit that the honeycomb geometry is also well described by this potential. The second reason comes from experiments where silicene is for the time being always deposited on a substrate. Scientists agreed with the fact that the substrate plays a major role in the formation and in the buckling of silicene. Of course, theoretical calculations based on DFT show that silicene is necessarily buckled but as we have seen, depending on the temperature and then on the superstructure observed, the silicene sheet never has the same buckling value. Furthermore, some superstructures which have never been observed (but predicted [130] such as $(\sqrt{(}7) \times \sqrt{(}7))R19.1^\circ$ and $(\sqrt{(}21) \times \sqrt{(}21))R19.1^\circ$) can be without buckling. The question remains unsolved.

Finally, we note that the original Tersoff parameters make the system melt into a liquid of wires while the ARK ones make the system melt into a 3D uniform liquid. In view of the fact that the ARK parameters give a melting temperature closer to the experimental one, we believe that they also describe better the melting of the silicene sheet but thorough experimental investigations must be conducted before a clear conclusion can be drawn on this point.

Note that the stability of a stand-alone sheet of silicene at high temperatures, however, is not yet tested in experiments in spite of the fact that it is experimentally proved that silicene on Ag (111) surface is stable at room

temperature.

4.4 Conclusion

In this chapter, we explored silicene, a new 2D Si material of honeycomb lattice, similar to graphene, its carbon counterpart. We have reviewed the state of the knowledge on silicene. As we have seen, silicene seems to be promising for electronic applications because of its properties similar to those of graphene. This new material is believed to be a more easily adaptable material in the current Si-based technology than graphene for new electronic devices.

We have seen that the thermal behavior of this new material has not been studied. This has motivated the study presented in this chapter: the thermal stability of a stand-alone silicene sheet using the Monte Carlo method with the Tersoff and ARK sets of parameters for the Tersoff potential. Theoretically, the existence and the stability of stand-alone silicene sheet and silicene nanoribbons have been demonstrated within DFT [120]. The main difference between silicene and graphene is that the latter is completely flat while silicene needs a small buckling to be theoretically stable. Experimentally, this buckling is confirmed in observations made until now. Regarding to the substrate temperature, we have seen that different superstructures composed of the same silicene sheet can be observed [130, 131]. These superstructures give different buckling values. Hence, the substrate temperature seems to have a major role for this characteristic. The silver (111) surface seems to be the best surface for the growth of a silicene sheet. Now, the question is: Is there any other substrate for the growth of silicene sheet? This question is still open and has attracted the attention of several researchers. If we find a new substrate, we will be able to understand more thoroughly the buckling of the silicene sheet.

For the moment, a stand-alone silicene sheet has never been synthesized, contrary to the case of graphene where such a sheet has been obtained. As we have seen, electronic properties of silicene nanoribbons are affected by the substrate, so if we want to use this promising material in devices, we must find a way to synthesize a stand-alone silicene (nanoribbons or sheets).

Our study of the behavior of a free-standing sheet of silicene presented in this chapter shows that the Tersoff potential [16] is able to stabilize a free-standing silicene sheet up to high temperatures (comparable to bulk 3D Si crystals). This characteristic has never been reported before for silicene. This potential has already been used in the case of the thermal stability of carbon nanotubes [134], using MD simulations but never with MC technique

applied to silicene. In Ref. [134] the authors artificially introduced Stone-Wales defects to reduce the melting temperature. As we have seen earlier, such a practice is needed in MD simulations to eliminate the superheating phenomenon.

The fact that the honeycomb structure of silicene corresponds to the lowest energy configuration, is also remarkable. Indeed, the Tersoff potential is initially fitted to reproduce bulk properties. The ability of this potential for modeling silicium atoms in a 2D honeycomb lattice was not a priori obvious.

The Tersoff potential yields a flat sheet of silicene. This result is not in agreement with experiments performed with silicene on substrate. The comparison of the silicene structure in the two situations may not be appropriate. Furthermore, our result of the flat structure is also not in agreement with previous theoretical DFT approaches. But again here, the potential and approximations used in these calculations and the limitation of the Tersoff potential used in our MC simulations make the comparison doubtful. Nevertheless, we hope that our result will allow a better understanding of the mechanisms responsible of the buckling if it really exists in the standalone silicene. Furthermore, as the buckling can be small (depending on the superstructure obtained [131]), we suppose that the global behavior of a freestanding silicene sheet against temperatures will be not changed. It is already the case for some electronic properties (linear dispersion in buckled nanoribbons) as we have seen above.

Finally, we have also observed that ARK parameters (initially proposed by Agrawal et al. to lower the melting temperature of diamond crystal of silicon) provoke a completely different behavior at high T (see Fig.4.10 for example). In order to determine the parametrization which better describes silicene, we have to wait experiments which study the thermal behavior of silicene (supported or unsupported by substrates). For the moment, such experiments have not been realized.

General Conclusion

In this thesis we have studied the thermal behavior of different materials, using Monte Carlo simulations. Our investigations have been carried out on rare-gas crystals, a semiconductor (Si) and a metal (Ag) in different situations and dimensions.

After the presentation of our algorithm, we have applied it to rare gas using the most popular potential, namely the Lennard Jones potential. Comparing our results with the existing ones, we have proposed a modification of the parameters of this potential to fit better the simulated melting temperature with the experimental one. As we have said, the overestimated melting temperature found with the original Bernardes parameters may come from the fitting procedure used by Bernardes which was based on the gaseous state at low temperatures. As we can easily understand, good parameters must yield results valid for the whole range of temperature. Hence, we have proposed parameters which are valid for a range of temperatures comprising the melting transition. Another important point is the following. The voids-nucleated method which is used in Molecular Dynamics is not necessary in Monte Carlo simulations. Indeed, with Molecular Dynamic simulations, the defects have to be created artificially while with Monte Carlo simulations, defects are naturally created with random displacements of atoms during a huge number of Monte Carlo steps.

We have also applied our algorithm to the 3D Si diamond lattice using the Stillinger Weber and the Tersoff potentials. The melting temperatures given by these two potentials are also overestimated. This behavior is well known for the Tersoff potential. This study of 3D bulk Si was a first step toward the modeling of 2D silicene, a Si counterpart of graphene.

We have next studied the 3D silver FCC lattice. Here, EAM and Gupta potentials were introduced and the same simulated melting temperature found with the two potentials are in good agreement with the experimental one. This last result allows us to study the Ag(111) surface which is an important surface for the growth of silicene structures. The modification of the algorithm in order to study a semi-infinite material (with a surface)

was presented. We found low-temperature contractions of the inter-layer distances between the topmost layers of the sample in agreement with theoretical and experimental results. Concerning the controversy about the variation of the contraction with increasing temperature, we have found two different results depending on the potential used. For the Gupta potential, the inter-layer distances stay contracted until the bulk melting temperature (absence of surface melting). For the EAM, an anomalous thermal expansion is observed at a temperature well below the bulk melting but above the surface melting observed only in the case of EAM potential.

Finally, we have studied the thermal behavior of a new promising material, namely silicene. We have used the Tersoff potential with a new configuration for Si atoms: the honeycomb structure. As we have seen, the Tersoff potential is able to describe and to stabilize this structure until very high temperatures. No such a study has previously been reported in the literature.

The results obtained in this doctorate work can be extended in several ways. Some of them are already in progress.

The first work which is in progress is the modeling of silicene sheet on the silver (111) surface. As we have seen, our algorithm which has treated the Ag(111) surface is ready and the algorithm which describes the silicene sheet is ready too. Now we are searching for a potential function which is able to correctly describe the interaction between the sheet and the substrate.

We want also to study free-standing silicene armchair and zigzag nanoribbons. This work has also begun with infinite silicene nanoribbons (as we have seen the ratio between the width and the length of this configuration allow this modelization) using the periodic boundary condition in one direction.

Another direction of our coming research is to include our results in the framework of the spin transport. The study of spins transport by Monte Carlo simulation, has been done in a previous algorithm of our team. However, in this first transport algorithm, the spins of the lattice are attached to their corresponding node. The spin states are updated according to the chosen spin model, but they are unable to have displacements. Hence, traveling spins of the current see fixed lattice spins, so that only magnetic scattering is taken into account in the spin resistivity, but not scattering of phonons. When the temperature increases, it will be interesting to test the influence of atoms displacements on the results already obtained. Adding such a phonon scattering will allow us to get results of spin resistivity even closer to the experimental reality. This study has already begun where we are studying Ising spin transport in a graphene sheet.

Finally, in collaboration with the Dr. Han Yilong of the Hong Kong University of Science and Technology, we have submitted a Hubert Curien

project for the study of thermal behavior of colloidal crystals for 2014-2015.

List of publications

[1] Virgile Bocchetti and H. T. Diep. Melting of Rare-Gas Crystal : Monte Carlo Simulations versus Experiments. *Journal of Chemical Physics*, **138**(11):516, 2013.

[2] Virgile Bocchetti and H.T. Diep. Monte Carlo Simulation of Melting and Lattice Relaxation of the (111) Surface of Silver. *Surface Science*, **614**(0):46 – 52, 2013.

[3] Virgile Bocchetti, H.T. Diep, Hanna Enriquez, Hamid Oughaddou, and Abdelkader Kara. Thermal Stability of Stand-alone Silicene Sheet. *ScienceJet*, *Submitted, Sept. 2013*.

[4] H. T. Diep, V. Bocchetti, D.-T. Hoang and V. T. Ngo, Theory and Simulation of Magnetic Materials: Physics at Phase Frontiers, *submitted for publication*, http://hal.archives-ouvertes.fr/hal-00863101 ; arXiv : 1309.4754

Appendix A

Computation of $\overrightarrow{K}$ for the Structure Factor

A.1 Ag(111) surface

It is clear that the triangular lattice of the (111) surface of a face-centered-cubic lattice of silver atoms is a Bravais lattice. To compute the geometrical structure factor, it is useful to consider the triangular lattice like a lattice with motifs.

Indeed, the geometrical structure factor is based on the interferences of the diffusing centers on a lattice with motifs. In Fig. A.1 we represent classical cartesian base vectors and another set of base vectors, namely $\mathscr{B}'\left(\overrightarrow{U}_{x'};\overrightarrow{U}_{y'};\overrightarrow{U}_{z'}\right)$. This last set of vectors clearly show the considered triangular lattice.

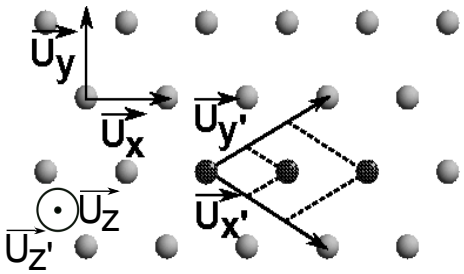

Figure A.1: Triangular lattice with two bases. The motif atoms are darker than the other atoms.

Following the notations introduced in Fig. A.1 for the different kinds of bases, the motif atoms, that we denote $\overrightarrow{d}_0$, $\overrightarrow{d}_1$ and $\overrightarrow{d}_3$, has the following

coordinates :

$$\overrightarrow{d}_0 = \begin{pmatrix} 0 \\ 0 \\ 0 \end{pmatrix}_{\mathscr{B}'} \quad \overrightarrow{d}_1 = \begin{pmatrix} \frac{1}{3} \\ \frac{1}{3} \\ 0 \end{pmatrix}_{\mathscr{B}'} \quad \overrightarrow{d}_2 = \begin{pmatrix} \frac{2}{3} \\ \frac{2}{3} \\ 0 \end{pmatrix}_{\mathscr{B}'}$$

Because it is easy to compute the coordinates of the vector of the reciprocal space in a base which is orthonormal, we convert and show all the coordinates in the classical cartesian base $\mathscr{B}\left(\overrightarrow{U}_x; \overrightarrow{U}_y; \overrightarrow{U}_z\right)$.

In the cartesian system we have :

$$\overrightarrow{U}_{x'} = \begin{pmatrix} \frac{3}{2} \\ -\frac{\sqrt{3}}{2} \\ 0 \end{pmatrix}_{\mathscr{B}} \quad \overrightarrow{U}_{y'} = \begin{pmatrix} \frac{3}{2} \\ \frac{\sqrt{3}}{2} \\ 0 \end{pmatrix}_{\mathscr{B}} \quad \overrightarrow{U}_{z'} = \begin{pmatrix} 0 \\ 0 \\ 1 \end{pmatrix}_{\mathscr{B}}$$

Using the definition of the reciprocal lattice vectors [11] :

$$\overrightarrow{b}_1 = \quad 2\pi \begin{pmatrix} \frac{1}{3} \\ -\frac{\sqrt{3}}{3} \\ 0 \end{pmatrix}_{\mathscr{B}} \quad \overrightarrow{b}_2 = \quad 2\pi \begin{pmatrix} \frac{1}{3} \\ \frac{\sqrt{3}}{3} \\ 0 \end{pmatrix}_{\mathscr{B}} \quad \overrightarrow{b}_3 = \quad 2\pi \begin{pmatrix} 0 \\ 0 \\ 1 \end{pmatrix}_{\mathscr{B}}$$

The vector $\overrightarrow{K}$ must be a vector of the reciprocal space. Hence, there exist $(n_1, n_2, n_3) \in \mathbb{Z}^3$ such as :

$$\overrightarrow{K} = \begin{pmatrix} \frac{1}{3}(n_1 + n_2) \\ \frac{\sqrt{3}}{3}(n_2 - n_1) \\ n_3 \end{pmatrix}_{\mathscr{B}}$$

In our case, the structure factor is given by :

$$S_{\overrightarrow{K}} = 1 + e^{\overrightarrow{K}.\overrightarrow{d}_1} + e^{\overrightarrow{K}.\overrightarrow{d}_2}$$

with,

$$\overrightarrow{K}.\overrightarrow{d}_1 = 2\pi\left(\frac{n_1 + n_2}{3}\right) \qquad \overrightarrow{K}.\overrightarrow{d}_2 = 4\pi\left(\frac{n_1 + n_2}{3}\right)$$

The structure factor is hence maximum if : $n_1 + n_2 = 3\,l, \quad l \in \mathbb{Z}$
A possible choice is : $(n_1; n_2) = (1; 2)$
Finally,

$$\overrightarrow{K} = \quad 2\pi \begin{pmatrix} 1 \\ -\sqrt{3} \\ 0 \end{pmatrix}_{\mathscr{B}}$$

A.2 Silicene

As we know, it is possible to talk about a reciprocal lattice if we have a Bravais lattice in the direct space. In the case of silicene, the honeycomb structure is not a Bravais lattice. Indeed, like we can see in Fig. A.2, the environment of the two atoms is not exactly the same; The environment of the atoms A is the rotation of 180° of the environment of the atoms B. Despite this remark, it is possible to see the honeycomb lattice like a triangular Bravais lattice with motifs (see Fig. A.2).

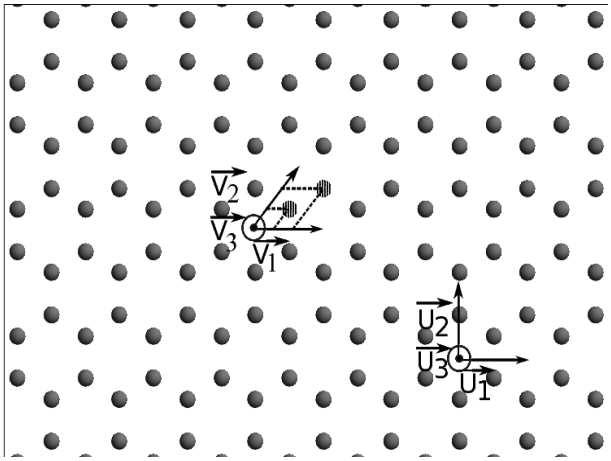

Figure A.2: Honeycomb lattice with two different bases. The motif atoms are darker than the other atoms.

Let $\mathscr{B}\left(\overrightarrow{U}_1; \overrightarrow{U}_2; \overrightarrow{U}_3\right)$ be the cartesian base. Let $\mathscr{B}'\left(\overrightarrow{U}_{x'}; \overrightarrow{U}_{y'}; \overrightarrow{U}_{z'}\right)$ be the other base.

In $\mathscr{B}$, the coordinates of the vectors of $\mathscr{B}'$ are the following :

$$\overrightarrow{V}_1 = \begin{pmatrix} \frac{1}{3} \\ -\frac{1}{3} \\ 0 \end{pmatrix}_{\mathscr{B}} \quad \overrightarrow{V}_2 = \begin{pmatrix} \frac{2}{3} \\ \frac{2}{3} \\ 0 \end{pmatrix}_{\mathscr{B}} \quad \overrightarrow{V}_3 = \begin{pmatrix} 0 \\ 0 \\ 1 \end{pmatrix}_{\mathscr{B}}$$

The coordinates of the motifs in $\mathscr{B}$ are :

$$\overrightarrow{d}_0 = \begin{pmatrix} \frac{1}{2} \\ \frac{\sqrt{3}}{6} \\ 0 \end{pmatrix}_{\mathscr{B}} \quad \overrightarrow{d}_1 = \begin{pmatrix} 1 \\ \frac{1}{\sqrt{3}} \\ 0 \end{pmatrix}_{\mathscr{B}}$$

Furthermore, the reciprocal lattice vectors are :

$$\overrightarrow{b}_1 = \quad 2\pi \begin{pmatrix} 1 \\ -\frac{\sqrt{3}}{3} \\ 0 \end{pmatrix}_{\mathscr{B}} \quad \overrightarrow{b}_2 = \quad 2\pi \begin{pmatrix} 0 \\ 2\frac{\sqrt{3}}{3} \\ 0 \end{pmatrix}_{\mathscr{B}} \quad \overrightarrow{b}_3 = \quad 2\pi \begin{pmatrix} 0 \\ 0 \\ 1 \end{pmatrix}_{\mathscr{B}}$$

As $\overrightarrow{K}$ is a reciprocal vector lattice, we can decompose it into $\mathscr{B}^* \left(\overrightarrow{b}_1; \overrightarrow{b}_2; \overrightarrow{b}_3 \right)$. There exist $(n_1; n_2; n_3) \in \mathbb{Z}$ such as : $\overrightarrow{K} = n_1 \overrightarrow{b}_1 + n_2 \overrightarrow{b}_2 + n_3 \overrightarrow{b}_3$.

The computation of the scalar product between $\overrightarrow{K}$ and the different motif vectors are the following :

$$\overrightarrow{K}.\overrightarrow{d}_0 = 2\pi \left(\frac{n_1 + n_2}{3} \right) \qquad \overrightarrow{K}.\overrightarrow{d}_1 = 2\pi \left(2\frac{n_1 + n_2}{3} \right)$$

Finally, in order to have an intensity which is maximum, we have to take $n_1 + n_2$ as a multiple of 3.

The expression of the coordinates of $\overrightarrow{K}$ in the case of silicene is :

$$\overrightarrow{K} = \quad 2\pi \begin{pmatrix} 1 \\ \sqrt{3} \\ 0 \end{pmatrix}_{\mathscr{B}}$$

Bibliography

[1] Nicholas Metropolis, Arianna W. Rosenbluth, Marshall N. Rosenbluth, Augusta H. Teller, and Edward Teller. Equation of State Calculations by Fast Computing Machines. *The Journal of Chemical Physics*, 21(6):1087–1092, 1953.

[2] Paras Mal Agrawal, Lionel M. Raff, and Ranga Komanduri. Monte Carlo Simulations of Void-Nucleated Melting of Silicon via Modification in the Tersoff Potential Parameters. *Phys. Rev. B*, 72:125206, 2005.

[3] R. E. ALLEN and F. W. DE WETTE. Calculation of Dynamical Surface Properties of Noble-Gas Crystals. I. The Quasiharmonic Approximation. *Phys. Rev.*, 179:873–886, 1969.

[4] Virgile Bocchetti and H.T. Diep. Monte Carlo Simulation of Melting and Lattice Relaxation of the (111) Surface of Silver. *Surface Science*, 614(0):46 – 52, 2013.

[5] F. A. Lindemann. The Calculation of Molecular Vibration Frequencies. *Phys. Z*, 11:609–612, 1910.

[6] David R. Nelson and B. I. Halperin. Dislocation-Mediated Melting in Two Dimensions. *Phys. Rev. B*, 19:2457–2484, Mar 1979.

[7] L. Gómez, A. Dobry, and H. T. Diep. Monte Carlo Simulation of the Role of Defects as a Melting Mechanism. *Phys. Rev. B*, 63:224103, May 2001.

[8] L. Gómez, A. Dobry, Ch. Geuting, H. T. Diep, and L. Burakovsky. Dislocation Lines as the Precursor of the Melting of Crystalline Solids Observed in Monte Carlo Simulations. *Phys. Rev. Lett.*, 90:095701, Mar 2003.

[9] N. D. Mermin. Crystalline Order in Two Dimensions. *Phys. Rev.*, 176:250–254, Dec 1968.

[10] D. Pettifor. *Bonding and Structure of Molecules and Solids*. Oxford University Press, London, 1995.

[11] Ch. Kittel. *Physique du Solide*. Dunod, 8 edition, 2008.

[12] Ashcroft, Neil W. and Mermin, David N. *Solid State Physics*. Thomson Learning, Toronto, 1^{st} edition, 1976.

[13] Raju P. Gupta. Lattice relaxation at a metal surface. *Phys. Rev. B*, 23:6265–6270, Jun 1981.

[14] Frank H. Stillinger and Thomas A. Weber. Computer simulation of local order in condensed phases of silicon. *Phys. Rev. B*, 31:5262–5271, Apr 1985.

[15] J. Tersoff. New Empirical Model for the Structural Properties of Silicon. *Phys. Rev. Lett.*, 56:632–635, Feb 1986.

[16] J. Tersoff. Modeling Solid-State Chemistry: Interatomic Potentials for Multicomponent Systems. *Phys. Rev. B*, 39:5566–5568, 1989.

[17] M. Foiles, S., I. Baskes, M., and S. Daw, M. Embedded-Atom-Method Functions for the FCC Metals Cu,Ag,Au,Ni,Pd,Pt, and their Alloys. *Physical Review B*, 33(12):7983–7991, 1986.

[18] P. Tchofo Dinda, G. Vlastou-Tsinganos, N. Flytzanis, and A. D. Mistriotis. Simulation of the Melting Behavior of Small Silicon Clusters. *Phys. Rev. B*, 51:13697–13704, May 1995.

[19] R. L. C. Vink, G. T. Barkema, W. F. Van-der Weg, and N. Mousseau. Fitting the Stillinger–Weber Potential to Amorphous Silicon. *J. of Non-Crystalline Solids*, 282:248, 2001.

[20] N. Bernardes. Theory of Solid Ne, Ar, Kr and Xe at 0 K. *Physical review*, 112(1534), 1958.

[21] James R. Morris and Xueyu Song. The Melting Lines of Model Systems Calculated from Coexistence Simulations. *The Journal of Chemical Physics*, 116(21):9352, 2002.

[22] Jeffrey R Errington. Solid-Liquid Phase Coexistence of the Lennard-Jones System Through Phase-Switch Monte Carlo Simulation. *The Journal of Chemical Physics*, 120(7):3130–41, February 2004.

[23] Ethan A Mastny and Juan J de Pablo. Direct Calculation of Solid-Liquid Equilibria from Density-of-States Monte Carlo Simulations. *The Journal of Chemical Physics*, 122(12):124109, March 2005.

[24] G. C. McNeil-Watson and N. Wilding. *The Journal of Chemical Physics*, 124:064504, 2006.

[25] W. Sutherland. *Philosophical Magazine*, pages 32–42, 1891.

[26] J. J. Gilvarry. The Lindemann and Grüneisen Laws. *Phys. Rev.*, 102:308–316, 1956.

[27] S A Cho. Role of Lattice Structure on the Lindemann Fusion Theory of Metals. *Journal of Physics F: Metal Physics*, 12(6):1069, 1982.

[28] Léon Brillouin. On Thermal Dependence of Elasticity in Solids. *Phys. Rev.*, 54:916–917, 1938.

[29] Max Born. Thermodynamics of Crystals and Melting. *The Journal of Chemical Physics*, 7(8):591–603, 1939.

[30] T. Gorecki. *Z Metall*, 65:426, 1974.

[31] Leonid Burakovsky, Dean L. Preston, and Richard R. Silbar. Melting as a Dislocation-Mediated Phase Transition. *Phys. Rev. B*, 61:15011–15018, 2000.

[32] H. Kleinert. *Gauge Theory in Condensed Matter*. World Scientific, Singapore, 1989.

[33] E. Pahl, F. Calvo, L. Koči, and P. Schwerdtfeger. Accurate Melting Temperature for Neon and Argon from Ab initio Monte Carlo Simulations. *Angewandte Chemie*, 47:8207–8210, 2008.

[34] E. Pahl, F. Calvo, and P. Schwerdtfeger. The Importance of Accurate Interaction Potentials in the Melting of Argon Nanoclusters. *International Journal of Quantum Chemistry*, 109(9):1812–1819, 2009.

[35] E. G. Noya and J. P. K. Doye. Structural Transitions in the 309-Atom Magic Number Lennard-Jones Cluster. *Journal of Chemical Physics*, 124:104503, 2006.

[36] S. R. Phillpot, J. F. Lutsko, D. Wolf, and S. Yip. Molecular-Dynamics Study of Lattice-Defect-Nucleated Melting in Silicon. *Phys. Rev. B*, 40:2831–2840, 1989.

[37] J. F. Lutsko, D. Wolf, S. R. Phillpot, and S. Yip. Molecular-Dynamics Study of Lattice-Defect-Nucleated Melting in Metals Using an Embedded-Atom-Method Potential. *Phys. Rev. B*, 40:2841–2855, 1989.

[38] Jan Solca, Anthony J. Dyson, Gerold Steinebrunner, Barbara Kirchner, and Hanspeter Huber. Melting Curve for Argon Calculated from Pure Theory . *Chemical Physics*, 224(2–3):253 – 261, 1997.

[39] Loup Verlet. Computer "Experiments" on Classical Fluids. I. Thermodynamical Properties of Lennard-Jones Molecules. *Phys. Rev.*, 159:98–103, Jul 1967.

[40] D. Frenkel and B. Smit. *Understanding Molecular Simulation: From Algorithms to Applications*. Academic, London, 2002.

[41] Virgile Bocchetti and H. T. Diep. Melting of Rare-Gas Crystal : Monte Carlo Simulations Versus Experiments. *Journal of Chemical Physics*, 138(11):516, 2013.

[42] J. E. Jones and A. E. Ingham. On the Calculation of Certain Crystal Potential Constants, and on the Cubic Crystal of Least Potential Energy. *Proceedings of the Royal Society A*, 107(636), 1925.

[43] M. L. Klein, G. K. Horton, and J. L. Feldman. Thermodynamic Properties of Solid Ar, Kr, and Xe Based Upon a Short-Range Central Force and the Conventional Perturbation Expansion of the Partition Function. *Phys. Rev.*, 184:968–978, Aug 1969.

[44] D. N. Batchelder, D. L. Losee, and R. O. Simmons. Measurements of Lattice Constant, Thermal Expansion, and Isothermal Compressibility of Neon Single Crystals. *Phys. Rev.*, 162:767–775, Oct 1967.

[45] E R Dobbs and G O Jones. Theory and Properties of Solid Argon. *Reports on Progress in Physics*, 20(1):516, 1957.

[46] Neil W. Ashcroft and David N. Mermin. *Solid State Physics*, chapter 6. Thomson Learning, Toronto, first edition, 1976.

[47] Alan M. Ferrenberg and Robert H. Swendsen. New Monte Carlo Technique for Studying Phase Transitions. *Phys. Rev. Lett.*, 61:2635–2638, 1988.

[48] Alan M. Ferrenberg and D. P. Landau. Critical Behavior of the Three-Dimensional Ising Model: A High-Resolution Monte Carlo Study. *Phys. Rev. B*, 44:5081–5091, 1991.

[49] D.P. Landau and K. Binder. *Monte Carlo Simulation in Statistical Physics*. Springer-Verlag, 1988.

[50] P. C. Hohenberg and B. I. Halperin. Theory of Dynamic Critical Phenomena. *Rev. Mod. Phys.*, 49:435–479, 1977.

[51] M. N. Barber. Phase Transitions and Critical Phenomena. *Phys. Rev. Lett.*, 8:145, 1983.

[52] K. Binder. *Rep. Prog. Phys.*, 50:783–859, 1987.

[53] K. Binder. *Rep. Prog. Phys.*, 60:487, 1997.

[54] A. Billoire, T. Neuhaus, and B. Berg. *Nucl. Phys. B.*, 396:779, 1993.

[55] Jooyoung Lee and J. M. Kosterlitz. Finite-Size Scaling and Monte Carlo Simulations of First-Order Phase Transitions. *Phys. Rev. B*, 43:3265–3277, Feb 1991.

[56] V. Thanh Ngo and H. T. Diep. Phase Transition in Heisenberg Stacked Triangular Antiferromagnets: End of a Controversy. *Phys. Rev. E*, 78:031119, 2008.

[57] Newton Bernardes. Theory of Solid Ne, A, Kr, and Xe at 0°K. *Phys. Rev.*, 112:1534–1539, 1958.

[58] E R Dobbs and G O Jones. Theory and Properties of Solid Argon. *Reports on Progress in Physics*, 20(1):516, 1957.

[59] D. N. Batchelder, D. L. Losee, and R. O. Simmons. Measurements of Lattice Constant, Thermal Expansion, and Isothermal Compressibility of Neon Single Crystals. *Phys. Rev.*, 162:767–775, 1967.

[60] M. L. Klein, G. K. Horton, and J. L. Feldman. Thermodynamic Properties of Solid Ar, Kr, and Xe Based Upon a Short-Range Central Force and the Conventional Perturbation Expansion of the Partition Function. *Phys. Rev.*, 184:968–978, 1969.

[61] H. Balamane, T. Halicioglu, and W. A. Tiller. Comparative Study of Silicon Empirical Interatomic Potentials. *Phys. Rev. B*, 46:2250–2279, Jul 1992.

[62] J. Tersoff. New Empirical Approach for the Structure and Energy of Covalent Systems. *Phys. Rev. B*, 37:6991–7000, 1988.

[63] J. Tersoff. Empirical Interatomic Potential for Silicon with Improved Elastic Properties. *Phys. Rev. B*, 38:9902–9905, 1988.

[64] Eric Pearson, Tadayoshi Takai, Timur Halicioglu, and William A. Tiller. Computer Modeling of Si and SiC Surfaces and Surface Processes Relevant to Crystal Growth from the Vapor. *Journal of Crystal Growth*, 70(1–2):33 – 40, 1984.

[65] P. N. Keating. Effect of Invariance Requirements on the Elastic Strain Energy of Crystals with Application to the Diamond Structure. *Phys. Rev.*, 145:637–645, 1966.

[66] Stillinger and Weber. Computer Simulation of Local Order in Condensed Phases of Silicon. *Physical review B*, 31:5262–5271, 1985.

[67] P.C.L Stephenson, M.W Radny, and P.V Smith. A modified Stillinger-Weber Potential for Modelling Silicon Surfaces. *Surface Science*, 366(1):177 – 184, 1996.

[68] John Ferrante, John R. Smith, and James H. Rose. Diatomic Molecules and Metallic Adhesion, Cohesion, and Chemisorption: A Single Binding-Energy Relation. *Phys. Rev. Lett.*, 50:1385–1386, 1983.

[69] James H. Rose, John R. Smith, and John Ferrante. Universal Features of Bonding in Metals. *Physical review B*, 28(4), 1983.

[70] R. Biswas and D. R. Hamann. New Classical Models for Silicon Structural Energies. *Phys. Rev. B*, 36:6434–6445, 1987.

[71] Brian W. Dodson. Development of a Many-Body Tersoff-Type Potential for Silicon. *Phys. Rev. B*, 35:2795–2798, 1987.

[72] S. Yoo, X. C. Zeng, and James R. Morris. The Meting Lines of Model Silicon Calculated from Coexisting Solid–Liquid Phases. *The Journal of Chemical Physics*, 120(3):1654–1656, 2004.

[73] C. Massobrio, V. Pontikis, and G. Martin. Amorphization Induced by Chemical Disorder in Crystalline $NiZr_2$: A Molecular-Dynamics Study Based on An n -Body Potential. *Phys. Rev. Lett.*, 62:1142–1145, 1989.

[74] Fran çois Willaime and Carlo Massobrio. Temperature-Induced HCP-BCC Phase Transformation in Zirconium: A Lattice and Molecular-Dynamics Study Based on An N -Body Potential. *Phys. Rev. Lett.*, 63:2244–2247, 1989.

[75] M. Nastar and F. Willaime. Tight-Binding Calculation of the Elastic Constants of FCC and HCP Transition Metals. *Phys. Rev. B*, 51:6896–6907, 1995.

[76] Fabrizio Cleri and Vittorio Rosato. Tight-Binding Potentials for Transition Metals and Alloys. *Phys. Rev. B*, 48:22–33, 1993.

[77] C. Mottet, G. Tréglia, and B. Legrand. Structures of a Ag Monolayer Deposited on Cu(111), Cu(100), and Cu(110) Substrates: An Extended Tight-Binding Quenched-Molecular-Dynamics Study. *Phys. Rev. B*, 46:16018–16030, 1992.

[78] H. T. Diep, S. Sawada, and S. Sugano. Melting and Magnetic Ordering in Transition-Metal Microclusters. *Phys. Rev. B*, 39:9252–9259, 1989.

[79] D. Tománek, S. Mukherjee, and K. H. Bennemann. Simple Theory for the Electronic and Atomic Structure of Small Clusters. *Phys. Rev. B*, 28:665–673, 1983.

[80] M.B. Gordon, F. Cyrot-Lackmann, and M.C. Desjonquères. Relaxation and Stability of Small Transition Metal Particles . *Surface Science*, 80:159–164, 1979.

[81] Murray S. Daw and M. I. Baskes. Semiempirical, Quantum Mechanical Calculation of Hydrogen Embrittlement in Metals. *Phys. Rev. Lett.*, 50:1285–1288, 1983.

[82] S. M. Foiles and J. B. Adams. Thermodynamic Properties of FCC Transition Metals as Calculated with the Embedded-Atom Method. *Phys. Rev. B*, 40:5909–5915, 1989.

[83] Ting Ning, Qingliang Yu, and Yiying Ye. Multilayer Relaxation at the Surface of FCC Metals: Cu, Ag, Au, Ni, Pd, Pt, Al . *Surface Science*, 206(1–2):L857 – L863, 1988.

[84] Murray S. Daw and S. M. Foiles. Order-Disorder Transition of Au and Pt (110) Surfaces: The Significance of Relaxations and Vibrations. *Phys. Rev. Lett.*, 59:2756–2759, 1987.

[85] J. S. Nelson, Erik C. Sowa, and Murray S. Daw. Calculation of Phonons on the Cu(100) Surface by the Embedded-Atom Method. *Phys. Rev. Lett.*, 61:1977–1980, 1988.

[86] P. Stoltze, K. W. Jacobsen, and J. K. Norskov. Monte Carlo Calculation of the Thermal Expansion Coefficient of Al. *Phys. Rev. B*, 36:5035–5036, 1987.

[87] S. M. Foiles. Application of the Embedded-Atom Method to Liquid Transition Metals. *Phys. Rev. B*, 32:3409–3415, 1985.

[88] X.W. Zhou, H.N.G. Wadley, R.A. Johnson, D.J. Larson, N. Tabat, A. Cerezo, A.K. Petford-Long, G.D.W. Smith, P.H. Clifton, R.L. Martens, and T.F. Kelly. Atomic Scale Structure of Sputtered Metal Multilayers. *Acta Materialia*, 49(19):4005–4015, November 2001.

[89] F. Jona. LEED Crystallography. *Journal of physics C : Solid State Physics*, 11(21):4271–4306, 1978.

[90] J. Friedel. *Ann. Phys.*, 1(257), 1976.

[91] R. N. Barnett, Uzi Landman, and C. L. Cleveland. Multilayer Lattice Relaxation at Metal Surfaces: A Total-Energy Minimization. *Phys. Rev. B*, 28:1685–1695, 1983.

[92] Uzi Landman, Ross N. Hill, and Mark Mostoller. Lattice Relaxation at Metal Surfaces: An Electrostatic Model. *Phys. Rev. B*, 21:448–457, 1980.

[93] J. P. Perdew. Physics of Lattice Relaxation at Surfaces of Simple Metals. *Phys. Rev. B*, 25:6291–6299, 1982.

[94] Laurent J. Lewis. Thermal Relaxation of Ag(111). *Phys. Rev. B*, 50:17693–17696, 1994.

[95] P. Statiris, H. C. Lu, and T. Gustafsson. Temperature Dependent Sign Reversal of the Surface Contraction of Ag(111). *Phys. Rev. Lett.*, 72:3574–3577, 1994.

[96] E.A Soares, G.S Leatherman, R.D Diehl, and M.A Van Hove. Low-Energy Electron Diffraction Study of the Thermal Expansion of Ag(111) . *Surface Science*, 468(1–3):129 – 136, 2000.

[97] Joost W. M. Frenken, Frank Huussen, and J. F. van der Veen. Evidence for Anomalous Thermal Expansion at a Crystal Surface. *Phys. Rev. Lett.*, 58:401–404, 1987.

[98] C. E. Botez, W. C. Elliott, P. F. Miceli, and P. W. Stephens. Thermal Expansion of the Ag(111) Surface Measured by x-ray Scattering. *Phys. Rev. B*, 63:113404, 2001.

[99] Ahlam N. Al-Rawi, Abdelkader Kara, and Talat S. Rahman. Anharmonic Effects on Ag(111): a Molecular Dynamics Study. *Surface Science*, 446(1–2):17 – 30, 2000.

[100] S. Narasimhan. Phonon Softening and the Anomalous Thermal Expansion of Ag(111). *Surface Science*, 417(2–3):L166 – L172, 1998.

[101] Abdelkader Kara, Pavlin Staikov, Ahlam N. Al-Rawi, and Talat S. Rahman. Thermal Expansion of Ag(111). *Phys. Rev. B*, 55:R13440–R13443, 1997.

[102] Xueguang Shao, Xiaomeng Liu, and Wensheng Cai. Structural Optimization of Silver Clusters up to 80 Atoms with Gupta and Sutton-Chen Potentials. *Journal of Chemical Theory and Computation*, 1(4):762–768, July 2005.

[103] I L Garzo, K Michaelian, and N Rendo. Structure and Energetics of Ni, Ag, and Au Nanoclusters. *Physical Review B*, 60(3):2000–2010, 2000.

[104] José Rogan, Griselda García, Max Ramírez, Víctor Muñoz, Juan Alejandro Valdivia, Xavier Andrade, Ricardo Ramírez, and Miguel Kiwi. The Structure and Properties of Small Pd Clusters. *Nanotechnology*, 19(20):205701, 2008.

[105] Fuyi Chen, Z. Y. Li, and Roy L. Johnston. Surface reconstruction precursor to melting in Au309 clusters. *AIP Advances*, 1(3):032105, 2011.

[106] M. Methfessel, D. Hennig, and M. Scheffler. Trends of the Surface Relaxations, Surface Energies, and Work Functions of the $4d$ Transition Metals. *Phys. Rev. B*, 46:4816–4829, 1992.

[107] S. Narasimhan and M. Scheffler. A Model for the Thermal Expansion of Ag(111) and Other Metal Surfaces. *Z. Phys. Chem.*, 202:253–262, 1997.

[108] Jianjun Xie, Stefano de Gironcoli, Stefano Baroni, and Matthias Scheffler. Temperature-Dependent Surface Relaxations of Ag(111). *Phys. Rev. B*, 59:970–974, 1999.

[109] Y. S. Touloukian, R. K. Kirby, R. E. Taylor, and P. D. Desai. *Thermophysical Properties of Matter*. New York, plenum edition, 1975.

[110] Paras M. Agrawal, Betsy M. Rice, and Donald L. Thompson. Molecular Dynamics Study of the Effects of Voids and Pressure in Defect-Nucleated Melting Simulations. *The Journal of Chemical Physics*, 118(21):9680–9688, 2003.

[111] Z. H. Jin, P. Gumbsch, K. Lu, and E. Ma. Melting Mechanisms at the Limit of Superheating. *Phys. Rev. Lett.*, 87:055703, 2001.

[112] K. Lu and Y. Li. Homogeneous Nucleation Catastrophe as a Kinetic Stability Limit for Superheated Crystal. *Phys. Rev. Lett.*, 80:4474–4477, 1998.

[113] Virgile Bocchetti, H.T. Diep, Hanna Enriquez, Hamid Oughaddou, and Abdelkader Kara. Thermal Stability of Stand-alone Silicene Sheet. *ScienceJet*, Submitted, Sept. 2013.

[114] P. R. Wallace. The Band Theory of Graphite. *Phys. Rev.*, 71:622–634, 1947.

[115] K. S. Novoselov, A. K. Geim, S. V. Morozov, D. Jiang, Y. Zhang, S. V. Dubonos, I. V. Grigorieva, and A. A. Firsov. Electric Field Effect in Atomically Thin Carbon Films. *Science*, 306(5696):666–669, 2004.

[116] M. S. Dresselhaus and G. Dresselhaus. Intercalation Compounds of Graphite. *Advances in Physics*, 30:139–326, 1981.

[117] K. S. Novoselov, D. Jiang, F. Schedin, T. J. Booth, V. V. Khotkevich, S. V. Morozov, and A. K. Geim. Two-Dimensional Atomic Crystals. *Proceedings of the National Academy of Sciences of the United States of America*, 102(30):10451–10453, 2005.

[118] K. S. Novoselov, A. K. Geim, S. V. Morozov, D. Jiang, M. I. Katsnelson, I. V. Grigorieva, S. V. Dubonos, and A. A. Firsov.

[119] Kyozaburo Takeda and Kenji Shiraishi. Theoretical Possibility of Stage Corrugation in Si and Ge Analogs of Graphite. *Phys. Rev. B*, 50:14916–14922, 1994.

[120] S. Cahangirov, M. Topsakal, E. Aktürk, H. Şahin, and S. Ciraci. Two- and One-Dimensional Honeycomb Structures of Silicon and Germanium. *Phys. Rev. Lett.*, 102:236804, 2009.

[121] S. Lebègue and O. Eriksson. Electronic Structure of Two-Dimensional Crystals from *ab initio* Theory. *Phys. Rev. B*, 79:115409, 2009.

[122] H. Şahin, S. Cahangirov, M. Topsakal, E. Bekaroglu, E. Akturk, R. T. Senger, and S. Ciraci. Monolayer Honeycomb Structures of Group-IV Elements and III-V Binary Compounds: First-Principles Calculations. *Phys. Rev. B*, 80:155453, 2009.

[123] S. Cahangirov, M. Topsakal, and S. Ciraci. Armchair Nanoribbons of Si and Ge Honeycomb Structures. *Phys. Rev. B*, 81:195120, 2010.

[124] Alper Ince and Sakir Erkoc. Silicene Nanoribbons: Molecular-Dynamics Simulations . *Computational Materials Science*, 50(3):865 – 870, 2011.

[125] C. Leandri, G. Le Lay, B. Aufray, C. Girardeaux, J. Avila, M.E. Dávila, M.C. Asensio, C. Ottaviani, and A. Cricenti. Self-Aligned Silicon Quantum Wires on Ag(1xa0;1xa0;0) . *Surface Science*, 574(1):L9 – L15, 2005.

[126] C. Polop, C. Rojas, J. A. Martín-Gago, R. Fasel, J. Hayoz, D. Naumović, and P. Aebi. Structure of Si Atomic Chains Grown on the Si/Cu(110) $c(2 \times 2)$ Surface Alloy. *Phys. Rev. B*, 63:115414, 2001.

[127] Bernard Aufray, Abdelkader Kara, Sebastien Vizzini, Hamid Oughaddou, Christel Leandri, Benedicte Ealet, and Guy Le Lay. Graphene-Like Silicon Nanoribbons on Ag(110): A Possible Formation of Silicene. *Applied Physics Letters*, 96(18):183102, 2010.

[128] Paola De Padova, Claudio Quaresima, Carlo Ottaviani, Polina M. Sheverdyaeva, Paolo Moras, Carlo Carbone, Dinesh Topwal, Bruno Olivieri, Abdelkader Kara, Hamid Oughaddou, Bernard Aufray, and Guy Le Lay. Evidence of Graphene-Like Electronic Signature in Silicene Nanoribbons. *Applied Physics Letters*, 96(26):261905, 2010.

[129] Boubekeur Lalmi, Hamid Oughaddou, Hanna Enriquez, Abdelkader Kara, Sebastien Vizzini, Benidicte Ealet, and Bernard Aufray. Epitaxial Growth of a Silicene Sheet. *Applied Physics Letters*, 97(22):223109, 2010.

[130] H Jamgotchian, Y Colignon, N Hamzaoui, B Ealet, J Y Hoarau, B Aufray, and J P Bibérian. Growth of Silicene Layers on Ag(111): Unexpected Effect of the Substrate Temperature. *Journal of Physics: Condensed Matter*, 24(17):172001, 2012.

[131] Hanna Enriquez, Sébastien Vizzini, Abdelkader Kara, Boubekeur Lalmi, and Hamid Oughaddou. Silicene Structures on Silver Surfaces. *Journal of Physics: Condensed Matter*, 24(31):314211, 2012.

[132] M. P. Allen and D. J. Tildesley. *Computer Simulation of Liquids*. Oxford science publications. Oxford University Press, USA, 1989.

[133] K V Zakharchenko, Annalisa Fasolino, J H Los, and M I Katsnelson. Melting of Graphene: From Two to One Dimension. *Journal of Physics: Condensed Matter*, 23(20):202202, 2011.

[134] Kaiwang Zhang, G Malcolm Stocks, and Jianxin Zhong. Melting and Premelting of Carbon Nanotubes. *Nanotechnology*, 18(28):285703, 2007.